Review Vol. 14, No. 3 / September 2022 / Advances in Optics and Photonics 571

Advances in Optics and Photonics

Semiconductor optical amplifiers: recent advances and applications

ANEESH SOBHANAN,[1,2] ARAVIND ANTHUR,[3] SEAN O'DUILL,[4] MARK PELUSI,[5] SHU NAMIKI,[5] LIAM BARRY,[4] DEEPA VENKITESH,[1,7] AND GOVIND P AGRAWAL[6,8]

[1]Department of Electrical Engineering, Indian Institute of Technology Madras, Chennai, India
[2]Now at Aston Institute of Photonic Technologies, Aston University, Birmingham, UK
[3]Institute of Materials Research and Engineering, A*STAR, 2 Fusionopolis Way, Singapore
[4]Radio and Optical Communications Laboratory, Dublin City University, Dublin, Ireland
[5]The National Institute of Advanced Science and Technology, Tsukuba, Japan
[6]The Institute of Optics, University of Rochester, Rochester, USA
[7]e-mail: deepa@ee.iitm.ac.in
[8]e-mail: govind.agrawal@rochester.edu

Received December 20, 2021; revised May 19, 2022; accepted May 20, 2022; published 20 September 2022

Owing to advances in fabrication technology and device design, semiconductor optical amplifiers (SOAs) are evolving as a promising candidate for future optical coherent communication links. This review article focuses on the fundamentals and broad applications of SOAs, specifically for optical channels with advanced modulation formats, as an integrable broadband amplifier in commercial transponders and as a nonlinear medium for optical signal processing. We discuss the basic functioning of an SOA and distortions of coherent signals when SOAs are used as amplifiers. We first focus on the techniques used for low-distortion amplification of phase-modulated signals using SOAs. Then we discuss optical signal processing techniques enabled by SOAs with an emphasis on all-optical wavelength conversion, optical phase conjugation, and phase quantization of coherent optical signals.

https://doi.org/10.1364/AOP.451872

Semiconductor optical amplifiers: recent advances and applications

Aneesh Sobhanan, Aravind Anthur, Sean O'Duill, Mark Pelusi, Shu Namiki, Liam Barry, Deepa Venkitesh, and Govind P Agrawal

1. INTRODUCTION

Semiconductor optical amplifiers (SOAs) were first developed during the 1980s, mainly motivated by their potential for the compensation of fiber's losses in optical communication systems. By 1989, several review articles had covered the gain and noise properties of SOAs, and the pros and cons of using such amplifiers [1–4]. With the adoption of the erbium-doped fiber amplifier (EDFA) for the purpose of in-line loss compensation, SOAs were used after 1990, mainly as integrable on-chip amplifiers within optical transmitters and receivers. It was also realized that SOAs have considerable potential for optical signal processing. Indeed, their use for wavelength conversion of intensity modulated channels was exploited extensively during the 1990s using nonlinear phenomena such as four-wave mixing (FWM) and cross-gain modulation (XGM) [5–7].

SOAs have remained an active area of research over the past 25 years [8–11]. This is due to their two important features. First, their tiny size and the use of semiconductor materials allow them to be integrated with other devices on the same chip. Second, SOAs can be used for optical signal processing, without introducing insertion losses, because they can also amplify the signal being processed through electrical pumping. The use of quantum-dot technology after 2001 has led to further improvements in the performance of modern SOAs [12]. For this reason, the applications of SOAs in coherent communication systems have been pursued extensively in recent years. Figure 1(a) shows the different linear and nonlinear effects of SOA and their potential application for amplification and other functional applications. The different impairments posed by the SOA when it is used as linear amplifier for single carrier and multi-carrier/WDM signals are shown in Fig. 1(b) along with their potential solutions.

In this review, our objective is to provide an up-to-date account of the recent progress in the field of SOAs, with an emphasis on their applications in coherent communication systems. To help the reader, Section 2 is devoted to the basic aspects of SOAs. It first covers the underlying physics and the structures used for making SOAs, and then describes the mathematical techniques used to understand their operation. Both the traveling-wave and the lumped models (based on the rate equations) of SOAs are discussed in the context of quantum-well (QW) as well as quantum-dot devices. Section 3 considers the use of SOAs as integrable optical amplifiers in both long-haul and short-haul optical networks, with an emphasis on their ultra-wide bandwidth. Nonlinear distortions introduced by the SOAs are also discussed, together with the techniques used to compensate them.

The focus of Section 4 is on all-optical wavelength conversion. Here, we first review the different nonlinear processes used for wavelength conversion such as XGM, cross-phase modulation (XPM), and FWM. We then focus on the fidelity of the conversion process in terms of the amplitude, phase and polarization of the converted channel. Techniques used to minimize the signal degradation are discussed in this section.

Figure 1

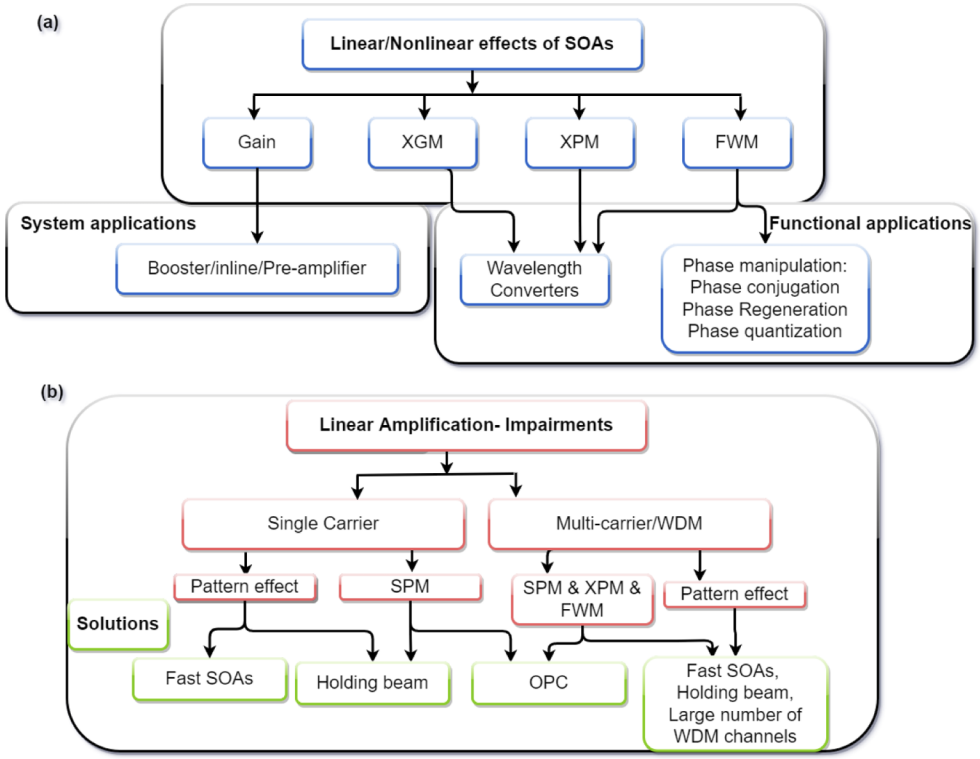

(a) Linear and nonlinear effects in SOA and their applications. (b) Impairments posed by SOA in linear amplification and their potential solutions.

The use of SOAs for phase manipulation is discussed in Section 5. We begin this section by reviewing how SOAs can be used for optical phase conjugation (OPC) and then consider the issues of optical signal-to-noise ratio (OSNR) degradation and the polarization sensitivity of the phase conjugation process. Phase quantization and phase regeneration are also considered in this section. Section 6 is devoted to the use of SOAs for optical switching. The concluding section points out other applications of SOAs and comments on the potential of SOAs in the near future.

2. BASIC CONCEPTS, THEORY AND MODELING OF SOAS

For the benefit of new researchers into photonic technologies, we devote this section to the basic concepts, device design, and modeling of SOAs. As SOAs find wide applications in all-optical signal processing, we focus on the modeling techniques that are best suited for such applications. With this aim in mind, we discuss the SOA models that are relatively simple to implement on any computer platform with a moderately fast run time. We also point to comprehensive SOA models whenever the simple models are likely to be insufficient. Even though the later sections focus mainly on operating wavelengths in the 1550-nm range, the analysis within this section is general in nature and can be applied to any SOA operating at a wavelength in the range from 700 to 2000 nm.

2.1. Short List of Important Papers

There are five topics that are fundamental to understanding the operation of SOAs, and these are listed below. All prior art that is essential for understanding the working of an SOA and its applications is comprehensively discussed in the papers listed here.

(1) Connelly [2001], "Wideband semiconductor optical amplifier steady-state numerical model" [13]. This paper describes the SOA's gain in terms of band filling in semiconductors and allows us to introduce a traveling-wave model with the amplified spontaneous emission (ASE) included. The source codes used to generate the results in this paper are available online [14].
(2) Agrawal and Olsson [1989] "Self-phase modulation and spectral broadening of pulses in semiconductor laser amplifiers" [15]. This paper makes the crucial transformation from a traveling-wave description to a lumped model that is suitable for the purpose of faster numerical simulations.
(3) Mork and Mecozzi [1997] "Saturation effects in nondegenerate four-wave mixing between short pulses in semiconductor optical amplifiers" [16]. This paper generalizes the lumped-model approach to include the intra-band nonlinear gain effects.
(4) Cassioli, Scotti, and Mecozzi [2000] "A time-domain computer simulator of the nonlinear response of semiconductor optical amplifiers" [17]. This paper shows how to use the lumped model in a communication-system simulator for FWM-based all-optical signal processing applications.
(5) Agrawal [1988] "Population pulsations and nondegenerate four-wave mixing in semiconductor lasers and amplifiers" [18]; Mecozzi et al. [1995] "Four-wave mixing in travelling-wave semiconductor optical amplifiers" [19]. These two papers clearly and concisely explain the origin of FWM in SOAs. Moreover, they contain analytical expressions for the conjugate field and provide an estimate for the conversion efficiency.

2.2. SOA Structures

SOAs are made with direct bandgap semiconductor materials. Recombination of electrons and holes is possible in such semiconductors without requiring a change in the momentum, i.e., without interaction with the underlying lattice. When electrons and holes are injected into such a device, they occupy various energy states, with electrons occupying the conduction band and holes occupying the valence band. A population inversion is possible in semiconductors with a direct bandgap. Under such conditions, electrons near the bottom of the conduction band recombine with the holes in the valence band, when undergoing stimulated emission in the presence of an electromagnetic wave.

Population inversion occurs when the summation of the probability of finding an electron in the conduction band and the probability of finding a hole in the valence band exceeds one [20]. In this situation, amplification of an optical signal through stimulated emission exceeds its direct absorption. The energy of each photon created during stimulated emission equals the energy lost by the recombining electron. SOAs require confinement of carriers, as well as of the electromagnetic field, within its active region for an efficient operation. The schematic of a typical SOA structure is shown in Fig. 2(a). The active region where amplification takes place is typically an undoped (intrinsic) semiconductor layer made of gallium arsenide (GaAs), indium phosphide (InP), or an alloy combining both compounds.

The wavelength range of interest determines the composition of various layers used to make SOAs. One has to choose the appropriate alloy mixtures for the device to operate in a wavelength range of interest. The active layer is sandwiched between two cladding layers, which are suitably doped. Electrons are injected into the active layer from the n-doped side, and holes are injected from the p-doped side. Carrier confinement within the active region (red hatched region in Fig. 2) is ensured by using heterostructures that create an insurmountable energy barrier for electrons and holes to migrate back

Figure 2

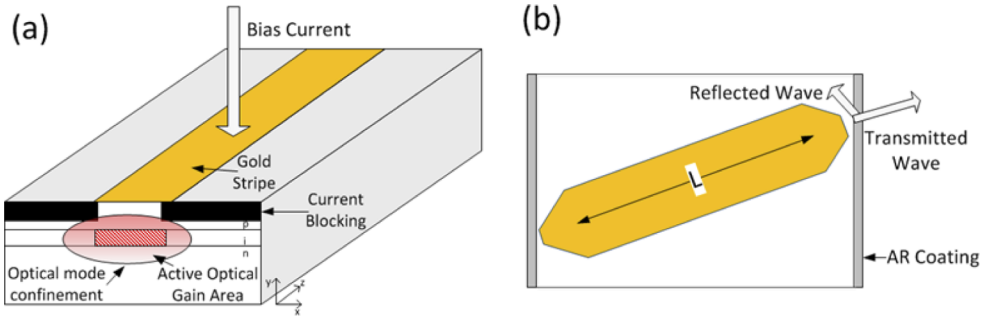

(a) Simplified SOA structure showing optical mode confinement. Electrons and holes are injected into the active region. Their presence creates a population inversion, allowing for amplification of injected light. (b) An SOA structure with a tilted waveguide. The tilt, in conjunction with the anti-reflection (AR) coatings, reduce feedback at the facets and avoids the structure from becoming a laser.

to their original layer. Recombination of carriers, whether spontaneous or stimulated, occurs only within the active region.

The doped cladding regions have a lower refractive index than the active region and therefore help with electromagnetic field confinement. The dimensions of the active region are critical to confine the radiation to the fundamental mode of the waveguide; the minimum size is related to the wavelength λ_0 of light being amplified. Making these dimensions too small would result in no wave being able to propagate along the waveguide. Making the dimensions too large would allow multiple modes to propagate with different spatial profiles, resulting in performance below that expected for single-mode SOAs. The design details of SOAs to meet single-mode criterion are beyond the scope of this review but are available in Ref. [21]. As shown in Fig. 2(b), the active region of an SOA is typically angled with respect to its cleaved facets to divert reflections away from the amplifying region; anti-reflection coatings at each facet further reduce the amount of backreflection. To avoid an SOA becoming a laser, the effective reflectivity of each facet should be much smaller than the single-pass gain of the SOA.

The gain of an SOA depends on the energy distribution of charged carriers. This distribution can be manipulated by inserting carrier-confining nanostructures within the active region. There are three possible types of structures that manipulate the allocation of charged carriers within the active region namely, (i) bulk, (ii) quantum-well (QW), and (iii) quantum dash/dot. The last two contain regions within the active layer comprising a material that has a lower bandgap compared with the rest of the active layer. The dimensions of these regions are smaller than the de Broglie wavelength of the carriers. As a result, the carriers can only exist at quantized energy states within the energy band of a semiconductor. The energy spread of the carriers due to their thermal energy is much reduced in this case, and the carriers remain tightly bound to energy levels defined by the dimensions of the quantum-confining regions. In bulk SOAs, there are no quantum-confining elements. As per elementary semiconductor band-filling theory, the density of states (D_S) of a bulk device, where the carriers are free to move in all three dimensions, scales with its energy, E as $D_S \propto \sqrt{E - E_V}$, where E_V is the lowest energy in the valence band. For a QW, a thin layer of lower band-gap material is embedded within the active region, as shown in Fig. 3(a). Its thickness is typically <15 nm, thus confining carriers to within this thin layer. The confinement of the electron's wave function is shown in Fig. 3(b) at a certain

Figure 3

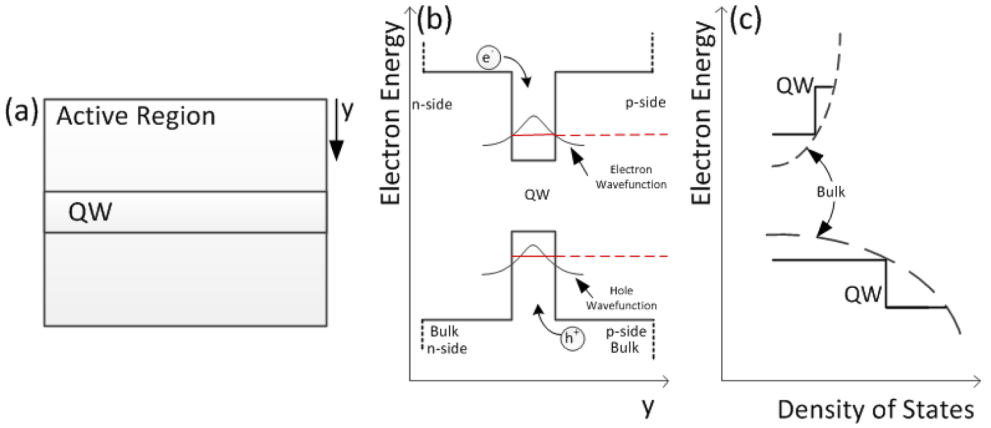

(a) Schematic of a QW within the active region of an SOA. (b) Allowed energy levels within the QW (shown by red dashed line) and (c) corresponding density of states.

energy level. Confining carriers in this way alters the density of states such that D_S develops a staircase structure, as shown in Fig. 3(c). The density of states of the lowest energy levels for electrons in QWs is much greater than the lowest energy density of states for bulk material, hence much larger optical gain is achieved at lower bias currents for QW material.

Confining the carriers to a specific energy states in QW and quantum dash/dot structures has two important advantages over bulk material. First, it reduces the threshold currents for lasers. Second, it increases the differential gain (dg_m/dN, where g_m is the gain coefficient (per meter) and N is the carrier density) compared with bulk devices. It is this second feature that is useful for SOAs. For QW lasers, a larger differential gain results in an increased modulation bandwidth. In the case of a QW SOAs, carriers are replenished quickly compared with a bulk SOA, allowing for exploitation of the nonlinear behavior for faster modulated signals. The crux of all-optical signal processing is to take advantage of the SOA gain responding instantaneously to the optical power. Having devices that respond quicker to the optical power reduces distortions due to SOAs, especially when the signal symbol rates approach 100 Gbaud.

2.3. Modeling of Bulk SOAs

2.3a. Population Inversion and Spontaneous Emission

No single SOA model can include all relevant effects, and a choice must be made based on the application. For example, models that include wavelength dependence of the amplification process may not necessarily be suitable for simulating the wave-mixing effects. One has to decide the most important features that needs to be included (amplification, FWM, XGM, XPM, wavelength dependence of gain, gain recovery times) before adopting an SOA model. We shall give guidelines as to which models are suited to each task.

As an example, consider modeling of an optical communication system. One may need to simulate thousands of data symbols, if the objective is to simulate the system's performance in terms of its bit error rate (BER). SOA models that are numerically efficient and capture the most relevant effects (such as FWM, XGM, noise) are suited for this purpose. There is always a temptation to implement a traveling-wave model because the SOA is a traveling-wave amplifier. However, the use of such a model is not necessary for such systems. If wavelength dependence can also be ignored, a simple SOA model converts the traveling-wave model to a set of rate equations [15,16]. Such

an approach speeds up system-level modeling because one does not need to solve for the forward and backward propagating signals. To see how the SOA can be condensed into a lumped model based on a set of differential equations, we briefly review a traveling-wave model.

We begin with the SOA model developed by Connelly [13]. This model considers band filling from a strict semiconductor-physics perspective and uses realistic energy distribution of electrons and holes within the SOA's active region. The energy difference between electrons and holes determines the wavelengths that can be amplified. The material gain g_m (gain per meter) of the SOA at any frequency υ is calculated using

$$g_m(\upsilon, N) = \frac{c^2}{4\sqrt{2}\pi^{3/2} n_1^2 \tau_S \upsilon^2} \left(\frac{2 m_e m_{hh}}{\hbar (m_e + m_{hh})} \right)^{3/2} \times \int_0^\infty \sqrt{\upsilon' - \frac{E_g(N)}{h}} [f_C(\upsilon', N) - f_V(\upsilon', N)] \left(\frac{2T_0}{1 + (2\pi T_0)^2 (\upsilon - \upsilon')^2} \right) d\upsilon', \tag{1}$$

where c is the speed of light in vacuum, n_1 is the refractive index of the active region, τ_S is the carrier radiative recombination lifetime, m_e is the electron's mass, m_{hh} is the heavy-hole mass, f_C and f_V are the Fermi distributions of electrons and holes, and E_g is the bandgap. The convolution integral results from the sum over all energy states of electron–hole pairs interacting with the optical field. This interaction is modeled as a damped harmonic oscillator with a dephasing lifetime T_0 ($\sim$ 1 ps), resulting in a Lorentzian-type spectral broadening associated with each electron–hole pair.

When the gain spectrum of an SOA is much wider than the bandwidth of the Lorentzian profile, the Lorentzian term can be replaced with a delta function $\delta(\upsilon - \upsilon')$. The integration in Eq. (1) is then easily performed to obtain

$$g_m(\upsilon, N) = \frac{c^2}{4\sqrt{2}\pi^{3/2} n_1^2 \tau_S \upsilon^2} \left(\frac{2 m_e m_{hh}}{\hbar (m_e + m_{hh})} \right)^{3/2} [\upsilon - E_g(N)/h]^{1/2} [f_C(\upsilon, N) - f_V(\upsilon, N)]. \tag{2}$$

The material gain is essentially a function of the density of states (term with the square root) and the Fermi distributions of the electrons in the conduction band and holes in the valence band. Its dependence on carrier density, N, is implicit within f_C and f_V, and it is known how to calculate these distributions [13].

As an example, Fig. 4 shows the calculated gain curves over a range of values of N ranging from 1.2×10^{24} m^{-3} to 2×10^{24} m^{-3}, using the codes supplied in Ref. [14]. The parameter values correspond to an SOA designed to provide maximum gain near 1550 nm. The gain curve can be well approximated by a quadratic function of wavelength and carrier density, and such quadratic gain models have been developed; see, for example, Ref. [22].

Most of the nonlinear effects are adequately explained by the simple relation $g_m = a(N - N_0)$ m^{-1}, where a, commonly known as the differential gain, is related to the slope of the gain curve at the chosen wavelength, and N_0 is the carrier density at transparency (i.e., the carrier density at which the material flips from being absorptive to amplifying). It is obvious from Fig. 4 that a is a function of the wavelength, and it is smaller for wavelengths larger than the gain peak compared with those smaller than that of the gain peak. When amplifying an input signal, the carrier density will also depend on the optical power as well as the injected current. For signal amplification, one would ideally like the SOA gain to be independent of the value of the carrier

Figure 4

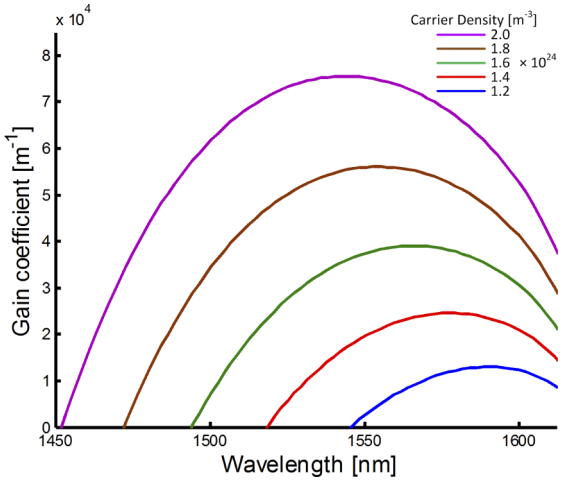

Calculated SOA gain curves with increasing values of carrier density. Adapted from J. Quant. Electron., **37**, 439 (2001) [13].

density. If that is not practicable, one would engineer the material such that the gain peak of the SOA is at a shorter wavelength than those of the signals being amplified, see, for example, Ref. [23]. For optimal nonlinear behavior of the SOA, one would engineer the gain peak of the SOA to coincide with the wavelength of the signals being manipulated through the nonlinear gain, see, for example, Ref. [24].

Spontaneous emission, an unwanted signal impairment, also occurs within any SOA, in addition to stimulated emission because there is a finite probability that an electron–hole pair recombines spontaneously and releases a photon. Such photons are emitted at random times with random phases and act as a noise. This noise is also amplified by the SOA, resulting in the ASE noise. This amplification process of the spontaneously emitted power, with power spectral density S_{ASE}, is governed by

$$\frac{dS_{ASE}}{dz} = g_m S_{ASE} + g_m n_{sp} h\upsilon, \tag{3}$$

where $h\upsilon$ in the second term is the photon energy and n_{sp} is known as the spontaneous emission factor. It denotes the relative level of population inversion. Integrating Eq. (3) over the length L of the SOA and setting $S_{ASE} = 0$ at $z = 0$, we obtain an important relation for the power spectral density of the ASE at the SOA output as

$$S_{ASE}(L) = n_{sp} h\upsilon[\exp(g_m L) - 1] = n_{sp} h\upsilon(G - 1), \tag{4}$$

where $G = \exp(g_m L)$ is called the unsaturated SOA gain. The minimum ASE noise occurs for complete population inversion, for which $n_{sp} = 1$. However, complete population inversion never occurs in SOAs, and typically n_{sp} is close to 3. The noise figure (F_n) of an SOA is defined as $F_n = 2n_{sp}$ and is relatively large for SOAs (close to 8 dB) compared with EDFAs. We use the material gain and total ASE power P_{ASE} for developing a traveling-wave model, which comes close to describing the physical propagation of light in SOAs.

2.3b. Basic Traveling-Wave Model

When modeling SOAs, one should always consider what the model does and, more importantly, does not do. For SOAs, one should consider the following questions. Can the model just consider power variations or do the phase variations need to be

Table 1. Typical Values of the Parameters for an SOA Operating Near 1550 nm

Symbol	Meaning	Value and/or Unit
N	Carrier density	m^{-3}
E	Optical field	$W^{-1/2}$
I	SOA drive current	350 mA
e	Quantum of electronic charge	1.66×10^{-19} C
A_c	Cross-sectional area of SOA active region	1.7×10^{-13} m^2
L	Length of SOA	800 μm
V	Volume of SOA active section, $L \times A_c$	1.36×10^{-16} m^3
A	Shockley–Read–Hall recombination rate	1×10^9 s^{-1}
B	Bimolecular recombination coefficient	1×10^{-16} $s^{-1}m^3$
C	Auger recombination coefficient	$1 \times 10^{-41} s^{-1}$ m^6
Γ	Confinement factor	0.2
a	Differential gain (dg_m/dN)	4×10^{-20} m^{-2}
N_0	Carrier density at transparency	1×10^{24} m^3
v_g	Group velocity c/(3.45)	0.87×10^8 m/s
α_H	Gain-phase coupling parameter	3
α_L	Waveguide scattering losses	5,000 m^{-1}
$\hbar\omega_0$	Photon energy	1.32×10^{-19} J
λ_0	Wavelength	1.55 μm
r_0	Reflectivity at input facet	0
r_1	Reflectivity at output facet	0

considered? Is it necessary to include the wavelength dependence of gain? Can the model assume that the gain response is instantaneous? Do temporal dynamics of the carrier-distribution process need to be considered? Do backreflections need to be considered, do multiple reflections from each facet need to be accounted for? Does ASE noise need to be included? Can the ASE noise be lumped as a single quantity denoting ASE power? Does wideband ASE noise need to be included? Do polarization effects need to be considered? The answers to these questions determine which SOA model is most appropriate for a given problem.

We focus on a traveling-wave model that includes the standard rate equation for the carrier density and two equations for the forward and backward propagating optical fields. We refer readers to look at other implementations of traveling-wave models [13,22]. The three basic equations are given by

$$\frac{dN(z,t)}{dt} = \frac{I}{eV} - R(N[z,t]) - \frac{\Gamma a(N[z,t]-N_0)}{A_c\hbar\omega_0}\left(\left|E^+\right|^2 + \left|E^-\right|^2\right), \tag{5}$$

$$\frac{\partial E^\pm}{\partial z} \mp \frac{1}{v_g}\frac{\partial E^\pm}{\partial t} = \frac{1}{2}\left(\Gamma a(N[z,t](1-j\alpha_H)-N_0) - \alpha_L\right)E^\pm + \varepsilon_{SE}, \tag{6}$$

where $N(z,t)$ is the carrier density at the location z at time t, I is the current injected into the SOA, e is an electron's charge, V is the active volume, A_c is the cross-sectional area of the SOA active region, a is differential gain, and Γ is the confinement factor. The total recombination rate of the carriers depends on N as $R = AN + BN^2 + CN^3$, where A, B, C are known parameters. Typical values of these parameters are given in Table 1.

In Eq. (6), we are invoking the slowly varying envelope approximation (SVEA) by only considering the relatively slower amplitude and phase variations arising from modulation and noise addition [15]. In the SVEA, only the first derivative of the envelope ($\partial/\partial z$) is retained. In addition, E is a scaled version of the electric field corresponding to the optical signal such that $|E|^2$ is the power of the signal being amplified. In Eq. (6), E^+ is the forward traveling field, E^- is the backward traveling field, v_g is the group velocity, α_L is the loss coefficient, α_H is the linewidth enhancement

factor is related to contribution of the carrier density to the refractive index [25], and ε_{SE} is the contribution of random carrier recombination to spontaneous emission. An assumption is also made in (5) by neglecting the standing-wave pattern of two counter-propagating waves. The carrier diffusion is assumed to wash out any variations in the carrier density at the sub-wavelength scale. To solve Eqs. (5) and (6), we also need to specify the boundary conditions at the facets, represented as

$$E^{+}(0,t) = E_{in}(t) + r_1 E^{-}(0,t), \qquad E^{-}(L,t) = r_2 E^{+}(L,t), \tag{7}$$

where r_1 and r_2 are reflection coefficients at the two facets and $E_{in}(t)$ is the envelope of the input signal. Input to the SOA can include any amplitude and phase-modulated signal. It can also include multiple channels at distinct wavelengths and/or additional pump waves launched to produce FWM interactions.

To solve Eq. (6) numerically, one needs to divide the SOA's length into multiple short segments and calculate the fields within each segment. For a segment of length Δz, the time taken by the field to propagate that segment is $\Delta t = \Delta z / v_g$. Using $t = m(\Delta t)$ and $z = n(\Delta z)$, where m and n are integers, the fields at each time iteration evolve as

$$\begin{aligned} E^{+}(n+1, m+1) &= \exp(G_{nm})\, E^{+}(n,m) + \hat{\varepsilon}_{SE} \\ E^{-}(n-1, m+1) &= \exp(G_{nm})\, E^{-}(n,m) + \hat{\varepsilon}_{SE}, \end{aligned} \tag{8}$$

where

$$G_{nm} = \frac{1}{2}\left(\Gamma a[N(n,m)(1 - j\alpha_H) - N_0]\right)\Delta z. \tag{9}$$

We show later that the ASE contribution $\hat{\epsilon}_{SE}$ can be added to the field at the input facet.

An alternative method for ASE estimation is to calculate the total ASE power separately from the signal, thereby separating the ASE noise into two counter-propagating average power contributions:

$$\begin{aligned} P_{ASE}(n+1, m+1) &= n_{sp} h\nu[\exp(\hat{G}_{nm}) - 1]B_o + \exp(\hat{G}_{nm}) P_{ASE}(n), \\ P_{ASE}(n-1, m+1) &= n_{sp} h\nu[\exp(\hat{G}_{nm}) - 1]B_o + \exp(\hat{G}_{nm}) P_{ASE}(n), \end{aligned} \tag{10}$$

where B_o is the SOA's gain bandwidth, $\hat{G}_{nm} = 2 \times \Re(G_{nm})$, and $\Re$ denotes the real part. Despite including the traveling-wave nature of the SOA, the preceding model has few drawbacks:

- requires extensive calculations at each spatial point;
- sampling time depends on the choice of Δz, and this may require the signal to be appropriately sampled;
- does not include wavelength dependence, unless one considers separate fields for each wavelength and sums over them to get the total $E^{\pm}$; this increases the total number of equations to $2M_\lambda + 1$, where M_λ is the number of wavelengths included in the model.

It is clear from Eqs. (5) and (6) that a large number of parameters need to be specified, even when one limits to a single wavelength. In the simplest case, we assume that the gain varies with carrier density as $g_m(N, \omega) = a(N - N_0)$ and the ASE is lumped into one single variable. Table 1 provides the typical values of the parameters for an SOA operating near 1550 nm.

Figure 5(a) shows variations of the steady-state carrier density and Fig. 5(b) shows variations in the ASE power along the length of the SOA when no signal is being

Figure 5

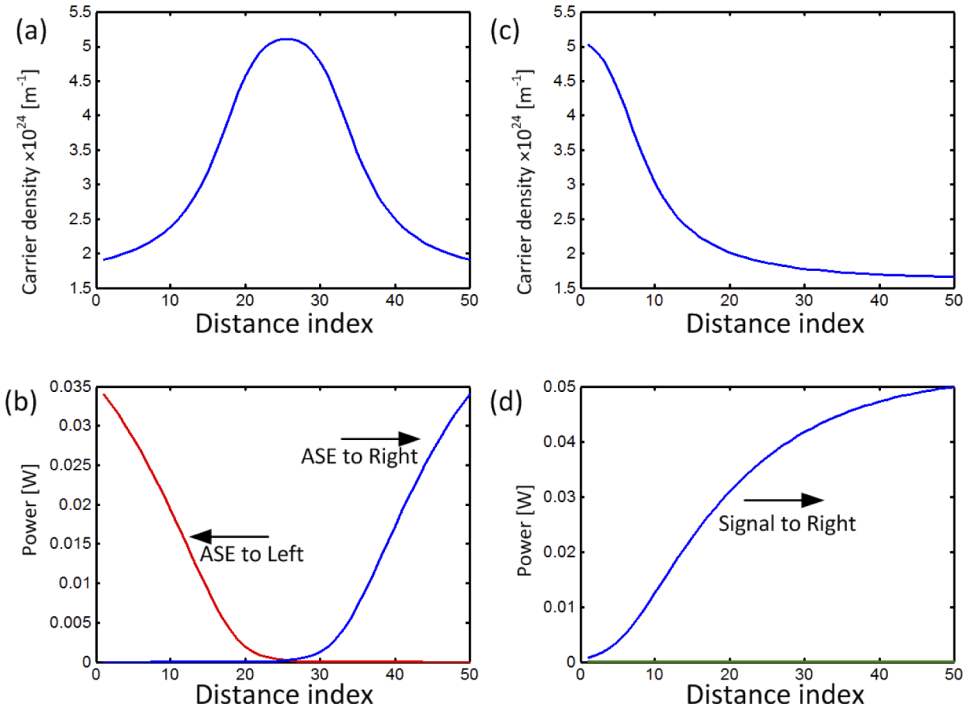

Results of the traveling-wave model. (a) Carrier density and (b) ASE power along the SOA's length without any injected optical wave. (c) Carrier density and (d) optical power along the SOA's length when a 1 mW optical signal is injected at the front facet. The green horizontal line represents the power of the backwards traveling wave, which is zero because the reflectivity of the facets is zero.

amplified. As the ASE propagates toward either facet, its power increases, which depletes the carriers close to both end facets, as seen in Fig. 5(a). When an optical signal is injected into the SOA from the left facet, its power first increases exponentially as seen in Fig. 5(d), which reduces the carrier density as seen in Fig. 5(c). The resulting saturation of the SOA gain makes the power increase only gradually in the second half of the SOA. As seen in Figs. 5(c) and 5(d), most of the amplification takes place in the first half of the SOA because of gain saturation.

One may think that a traveling-wave model cannot be used for modulated input signals because it does not include multiple wavelengths and ignores all FWM effects. This is true to some extent. However, some FWM effects can be captured writing the input field as

$$E_{in}(t) = \sum_n E_n(t) \exp(2\pi j n \Delta f_n t + j\phi_n), \tag{11}$$

where Δf_n is the detuning of the nth channel relative to the reference frequency and ϕ_n is its phase. The complex valued time-varying modulation can be included within $E_n(t)$.

2.4. Derivation of the Lumped Model

In this section we show how the traveling-wave models can be transformed into a lumped SOA model described by a set of ordinary differential equations with suitable approximations. If an SOA is designed with anti-reflection coatings at both facets, we can ignore all facet reflections. If we also neglect ASE, we only need to and consider a single forward-propagating wave corresponding to the signal being amplified.

Introducing the local gain coefficient at any distance z as $g_m(z,t) = \Gamma a(N - N_0)$, Eqs. (5) and (6) of the traveling-wave model are reduced to

$$\begin{aligned} \frac{dg_m(z,t)}{dt} &= \frac{g_m(z,t) - g_{m0}}{\tau_S} - \frac{g_m(z,t)|E(z,t)|^2}{P_{sat}\tau_S}, \\ \frac{dE(z,t)}{dz} &= \frac{1}{2}\left[g_m(z,t)(1 - j\alpha_H) - \alpha_L\right] E(z,t), \end{aligned} \tag{12}$$

where g_{m0} is the unsaturated gain coefficient due to the bias current and equals $aN_0(I/I_0 - 1)$ and I_0 is the current needed for transparency and equals eVN_0/τ_S; τ_S is an effective carrier lifetime related to the recombination rate R in Eq. (5). The saturation power is defined as $P_{sat} = (\Gamma a \tau_S)^{-1}$. The electric-field equation can be converted into an intensity equation for $|E|^2 = E^*E$, resulting in

$$\frac{d|E(z,t)|^2}{dz} = \left[g_m(z,t) - \alpha_L\right]|E(z,t)|^2. \tag{14}$$

It turns out that Eqs. (12) and (14) can be solved analytically [15]. We first write the formal solution of Eq. (14) in the form

$$|E(z,t)|^2 = |E(0,t)|^2 \exp\left[\int_0^z \left[g_m(z,t) - \alpha_L\right] dz\right] = |E(0,t)|^2 \exp(h_N - \alpha_L L), \tag{15}$$

where we defined a new variable h_N with the physical meaning of total integrated gain as

$$h_N(t) = \int_0^L g(z,t)dz. \tag{16}$$

We substitute this solution into (12) and integrate it over the entire length of the SOA. It is easy to show that $h(t)$ is approximated by the following equation [26]:

$$\frac{dh_N}{dt} = \frac{h_N - h_0}{\tau_S} - \left(\frac{h_N}{h_N - \alpha_L L}\right)\frac{[\exp(h_N - \alpha_L L) - 1]\,|E_{in}|^2}{P_{sat}\tau_S}. \tag{17}$$

The above equation is exact when losses vanish ($\alpha_L = 0$) [15]. As seen in Fig. 5(c), the carrier density is not constant, though we have shown in Ref. [26] that Eq. 17 is a very good approximation. Equation (17) describes the SOA's gain dynamics when an optical pulse is injected into the SOA with the input field $E(0,t)$. In this formulation, the SOA can be treated as a lumped element without any consideration to the traveling-wave nature of the optical fields. The electric field at the SOA's output end is related to the input field E_{in} as

$$E_{out}(t) = E_{in}(t)\exp\left[\tfrac{1}{2}h_N(t)(1 - j\alpha_H) - \tfrac{1}{2}\alpha_L L\right]. \tag{18}$$

The lumped model can be extended to include several important effects such as carrier heating (CH) and spectral hole burning (SHB). Although both of them do not include the carrier density number, their inclusion is necessary to account for changes in the optical gain due to the energy distribution of the carriers and thus affect the integrated gain $h_N(t)$. Their effect can be included by considering h as the sum of three parts: $h = h_N + h_{CH} + h_{SHB}$. Polarization effects can be included by writing the input electric field in a vectorial form:

$$\mathbf{E}_{in}(t) = E_{in}^{TE}(t)\hat{\mathbf{e}}_{TE} + E_{in}^{TM}(t)\hat{\mathbf{e}}_{TM}, \tag{19}$$

where $\hat{\mathbf{e}}_{TE}$ and $\hat{\mathbf{e}}_{TM}$ are units vectors along which the transverse electric (TE) and transverse magnetic (TM) modes of the SOA are polarized. The input intensity is then

the sum over these two modes such that

$$|E_{in}(t)|^2 = |E_{in}^{TE}(t)|^2 + |E_{in}^{TM}(t)|^2. \tag{20}$$

With these modifications, the three parts of h satisfy the following three equations [16]:

$$\frac{dh_N}{dt} = \frac{h_0 - h_N}{\tau_S} - \frac{h_N[\exp(h_N - \alpha_L L) - 1]}{(h_N - \alpha_L L)P_{sat}\tau_S}\left[|E_{in}^{TE}(t)|^2 + |E_{in}^{TM}(t)|^2\right], \tag{21}$$

$$\frac{dh_{SHB}}{dt} = -\frac{h_{SHB}}{\tau_1} - \frac{\varepsilon_{SHB}h_N[\exp(h_N - \alpha_L L) - 1]}{(h_N - \alpha_L L)\tau_1}\left[|E_{in}^{TE}(t)|^2 + |E_{in}^{TM}(t)|^2\right], \tag{22}$$

$$\frac{dh_{CH}}{dt} = -\frac{h_{CH}}{\tau_h} - \frac{\varepsilon_{CH}h_N[\exp(h_N - \alpha_L L) - 1]}{(h_N - \alpha_L L)\tau_h}\left[|E_{in}^{TE}(t)|^2 + |E_{in}^{TM}(t)|^2\right]. \tag{23}$$

In these equations, we have assumed identical gain for both TE and TM modes, this is a reasonable assumption considering that difference in gain between TE and TM modes is typically <0.3 dB [24]. Treating the two gains as being equal is a compromise made for simplifying the lumped model. The characteristic time of carrier–phonon scattering, i.e., the time constant associated with a carrier distribution relaxing to the temperature of the vibrating crystal lattice structure is given by τ_h, and the carrier–carrier scattering time is given by τ_1. The SOA parameters such as carrier lifetime and the gain recovery times associated with the intraband processes may also be polarization dependent [27]: this can lead to nonlinear polarization rotation, whereby the power of the input waves can alter the polarization state of the output waves [28,29]. Another consideration is related to the choice of the time step when these equations are solved numerically. It should be smaller than the shortest time scales of the processes considered, to avoid numerical instability and to obtain a reasonably accurate solution. The smallest lifetime is the scattering time τ_1 between two charged carriers, and the time step should be less than the value of this parameter (~10 fs). This results in oversampling of the signal being amplified and requires relatively long computing times.

A reasonable approximation can reduce the computing times considerably. It makes use of the observation that fast dynamics of both CH and SHB allows a steady state to be reached at the time scale at which the signal's intensity $|E_{in}(t)|^2$ changes. In this situation, we can set the time derivatives, dh_{SHB}/dt and dh_{CH}/dt to zero. This is known as the adiabatic approximation, and its use allows us to solve Eqs. (22) and (23) and obtain

$$h_{SHB} = -\frac{\varepsilon_{SHB}h_N\tau_1}{h_N - \alpha_l L}\left[\exp\left(h_N - \alpha_L L\right) - 1\right]\left(|E_{in}^{TE}(t)|^2 + |E_{in}^{TM}(t)|^2\right), \tag{24}$$

$$h_{CH} = -\frac{\varepsilon_{CH}h_N\tau_h}{h_N - \alpha_l L}\left[\exp\left(h_N - \alpha_l L\right) - 1\right]\left(|E_{in}^{TE}(t)|^2 + |E_{in}^{TM}(t)|^2\right). \tag{25}$$

The TE and TM components of the amplified signal at the SOA output field are given by

$$E_{out}^{\mu}(t) = E_{in}^{\mu}(t)\exp\left[\tfrac{1}{2}h_N(t)\left(1 - j\alpha_H\right) + h_{CH}(t)\left(1 - j\alpha_{CH}\right) + h_{SHB}(t) - \tfrac{1}{2}\alpha_L L\right], \tag{26}$$

where μ stands for TE or TM.

This extended lumped model is quite versatile as it includes gain saturation, as well as the effects of intraband changes to the SOA gain induced by CH and SHB. The model also automatically includes all FWM effects, if the input electric field is given in the form of Eq. 11. In this case, nonlinear phase rotations resulting from self-phase modulation (SPM) and XPM are also automatically included. For completeness, if necessary, coupling losses at each facet can be easily included.

2.5. Inclusion of ASE and Simulation Results

ASE noise is still missing from the lumped model. Even though the buildup of ASE noise along the amplifier's length cannot be included in the lumped model, some features can be incorporated by considering the power spectral density of the ASE noise given as (4). As $G \gg 1$ typically in most applications of SOAs, we can account for the amplification of noise inside the SOA by adding noise to the input signal with the power spectral density $S(\upsilon) = n_{sp}h\upsilon$ [17]. The sampled ASE noise is split between two quadratures, with the following expression for the ASE noise at the nth sampling instance

$$\varepsilon_{ASE}(nt_s) = \sqrt{\frac{n_{sp}h\upsilon}{2t_s}}\left[\varepsilon_I(nt_s) + j\varepsilon_Q(nt_s)\right], \tag{27}$$

where ε_I and ε_Q represent the in-phase and quadrature components of the ASE-noise field, each modelled as a random Gaussian random variable. Here t_s is the step size or sampling time such that $1/t_s$ represents the simulation bandwidth. Note that the approach of including the ASE in this way is also valid for the traveling-wave approach.

We have used the lumped SOA model for applications ranging from signal amplification to FWM-based wavelength conversion [26,30–34], and a few specific results are shown in Fig. 6. Table 2 lists the values of SOA parameters used for these simulations. To demonstrate the possibilities of the type of system simulations that are possible we show some of the main results. The simulation framework for dual-pump FWM is shown in Fig. 6(a); the signal to undergo wavelength conversion is a 16-QAM signal at 10 GBaud. The pumps and the 16-QAM signal are numerically generated, added together, then the entire field passed through the SOA block, the wavelength converted idler is filtered out and the BER is calculated for differing values of OSNR at the receiver. We used the simulator to find the acceptable linewidth limits for the pump(s). The formal treatment of pump phase noise transfer to the wavelength converted signal is given in Section 4.2.2. The BER results from the simulator are shown in Fig. 6(b), we obtain the expected result that the pump linewidth tolerance for the dual-pump scenario is double that for single-pump scheme. Phase noise is present in light from all semiconductor lasers and arises from random spontaneous emission and a complete treatment of is given in Ref. [25]. Details about how to implement appropriate laser phase noise for numerical simulations are available in Ref. [30].

Figure 6(c) shows the eye diagrams of an amplified PAM-4 signal at 28 GBaud. The PAM-4 signal was amplified by the SOA, filtered using a 50-GHz super-Gaussian bandpass filter, and detected using an ideal photodetector. Four eye diagrams in Fig. 6(c) show the amplification for input powers ranging from −23 dBm to 0 dBm. At a low input power, ASE is the dominant signal impairment, and the BER is 0.016. There exists an optimum input power for which the BER becomes minimum, i.e., the signal becomes strong enough to overcome the ASE but remains weak enough to not produce nonlinear distortions. This occurs for an input power of −10 dBm. Increasing the input power to 0 dBm nonlinear distortions become the dominant impairment. Figure 6(d) shows BER curves when one, three, and five PAM-4 signals are amplified simultaneously with 100-GHz channel spacing. The eye diagrams corresponding to subplots (i), (ii), and (iv) are indicated in Fig. 6(d). The corresponding BER for subplot (iii) is off the scale and omitted. At low input powers (< − 10 dBm), the BER is independent of the number of channels, as the only impairment is due to ASE. Many similarities are found between experimentally measured BER and calculated BER from the simulator. For example, the BER goes below 10^{-4} when the input power is greater than −18 dBm, and this is shown experimentally for such systems in Ref. [35]. At larger input powers, the BER rises owing to signal distortions from gain saturation; when amplifying using

Figure 6

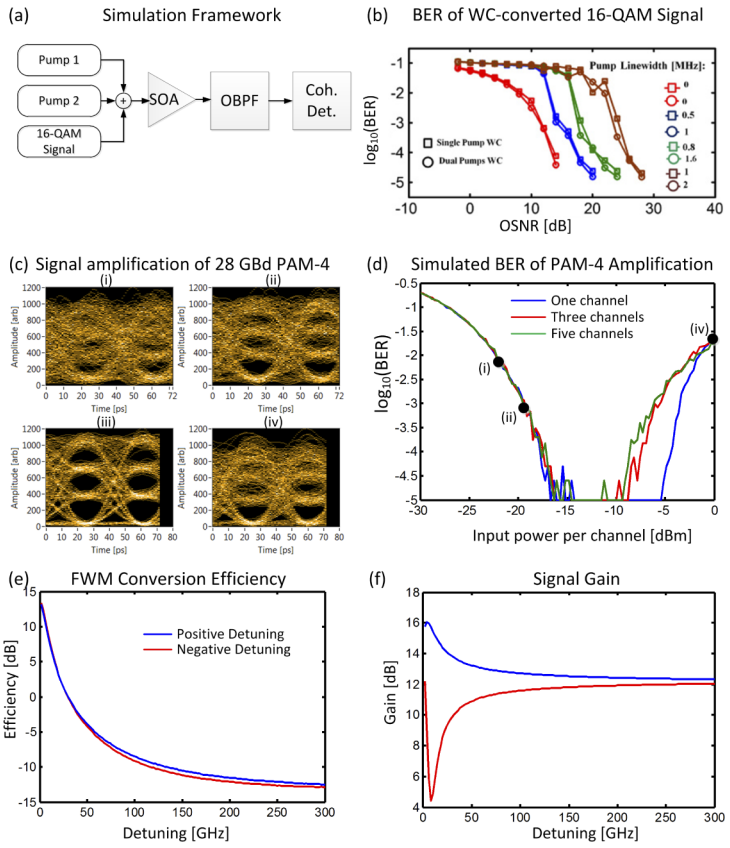

Results obtained with the lumped SOA model. (a) Simulation framework for dual-pump FWM scheme. (b) BER dependence on OSNR at the receiver with pump linewidth as parameter. (c) Eye patterns for a 28-GBaud PAM-4 signal for input powers from (i) −23 dBm to (iv) 0 dBm. They show the influence of ASE noise in (i), "error-free" amplification in (iii), and strong nonlinear distortions in (iv). (d) BER of a multichannel PAM-4 signal. (e) FWM conversion efficiency and (f) calculated signal gain for the continuous wave (CW) pump and signal fed to the input of the SOA in the pump–probe scheme.

Table 2. Simulation Parameters Used for the Nonlinear SOA for FWM and Linear SOA for Amplification for Obtaining the Results in Fig. 6

Scenario	SOA for FWM	SOA for Amplification
h_0	8	6
$\alpha_L L$	2	3
α_H	-3	-3
P_{sat}	10 mW	10 mW
τ_S	100 ps	100 ps
ε_{SHB}	1 W^{-1}	1 W^{-1}
ε_{CH}	2 W^{-1}	2 W^{-1}
α_{CH}	-1	-1

SOA, the BER reaches a minimum for input powers around −12 dBm using the simulator and −10 dBm in the experiment. BER levels below 10^{-4} can be calculated by simulating millions of symbols and there is also scope to change the SOA parameters, i.e., the noise figure to match experimental BER at low input powers (< − 15 dBm) and to set the saturation power and carrier lifetime values to match the BER at high input powers (> − 5 dBm). For input signal powers of −5 dBm, BER becomes worse

in the multichannel case, compared with the single-channel case, owing to the effect of XGM and FWM from neighbouring channels. At 0 dBm, there appears to be a crossover in BER performance in the sense that the multichannel case outperforms the single-channel case. An explanation is that power variations are smoothed out with increasing channel count. More details on the results contained within Figs. 6(c) and 6(d) are available in Ref. [31].

Figures 6(e) and (f) show the FWM conversion efficiency (ratio of the output conjugate power to the input signal power) performance of an SOA for the continuous wave (CW) pump and signal waves. The pump power is 1 mW whereas the signal power is 0.1 mW, the detuning between the signal and pump waves are varied. In this section we define the detuning to be $\nu_{signal} - \nu_{pump}$. Figure 6(e) shows conversion efficiency as the pump–signal detuning is increased from −300 GHz to +300 GHz using the lumped model. Values of conversion efficiency lager than 0 dB are possible for SOAs whose small-signal gain approaches 30 dB. Figure 6(f) shows the signal's saturated gain calculated using the lumped model and its dependence on the pump–signal detuning. As seen there, the gain of a redshifted signal (positive detuning) is higher for an SOA. This asymmetry is a consequence of the phase-amplitude coupling in SOAs governed by the parameter α_H.

2.6. FFT-Based SOA Modeling

If wavelength-dependent gain needs to be included, while accounting for all FWM effects, a hybrid approach involving both time and spectral domains is employed. It makes use of the fast Fourier transform (FFT) because the wavelength decomposition does not automatically capture the FWM effects. One such procedure is outlined in Ref. [36]. In this approach, the wavelength dependence of the SOA gain is incorporated in the spectral domain, whereas the FWM effects are incorporated in the time domain. Here we just highlight the main points and refer to Ref. [36] for details.

For specifying the frequency dependence of the gain coefficient $g(N, \omega)$, the gain spectrum is approximated with a parabola centered at the gain peak, while also including the wavelength dependence of the gain peak. Let $E_n = E(n\Delta t_s)$ be the envelope of the total optical field sampled at intervals Δt_s and $\tilde{E}_k$ represent the FFT of E_n. The first item that needs to be calculated is the (temporal) average carrier density, $\bar{N}$ at any point z along the SOA. This is done by solving Eq. (5) in steady state, i.e., $dN/dt = 0$, and also noting that $P_0(z) = \langle |E(z,t)|^2 \rangle$

$$0 = \left(\frac{I}{eV}\right) - R\left(\bar{N}\right) - \left(\frac{\Gamma a}{\hbar\omega_0} P_0(z)\right)\bar{N} + \frac{\Gamma a N_0}{\hbar\omega_0}, \tag{28}$$

where P_0 is the average optical power, and a is the differential gain. Knowing the value of $\bar{N}$ allows us to calculate $g_m\left(\bar{N}, k\right)$ at the corresponding index in the FFT array. Care needs to be taken while mapping the FFT index to the frequency of the envelope f_k [37]. A simple relation for the FFT index k for an K-point FFT is as follows: k is in the range from $0 \le k \le (K-1)$:

$$f_k = \begin{cases} \dfrac{k}{Kt_s} & k \le K/2, \\ \dfrac{k-K}{Kt_s} & k > K/2. \end{cases} \tag{29}$$

The beating terms arising from the modulation of the gain that create the FWM products as well as the terms governing self-gain modulation and XGM. Recall $\mathbf{F}\left[|E|^2\right] = \tilde{E} \otimes \tilde{E}^*$, where $\mathbf{F}$ denotes the Fourier transform, $\otimes$ denotes convolution, and a tilde denotes the Fourier transform of that variable. Using this relation, the

beating contributions from the carrier density modulation (CDM), CH, and SHB are included as

$$\tilde{F}_k = \sum_{m=CDM,CH,SHB} \frac{(1-j\alpha_m)}{(1+j\Omega_k\tau_m)\,P_{sat,m}} \tilde{E}_k \otimes \tilde{E}_k^*, \tag{30}$$

where α_m, $P_{sat,m}$, and τ_m are the gain-phase coupling parameter, saturation power, and response time associated with three different contributions. The $k = 0$ index in the case of CDM corresponds to the DC term, which has already been used for calculating $\bar{N}$. This term is not included while calculating F_k. The propagation equation thus takes the form

$$\frac{d\tilde{E}_k}{dz} = \frac{1}{2} g\left(\bar{N}, k\right)\left[(1-j\alpha_H)\,\tilde{E}_k - \kappa_k\right] - \frac{\alpha_{loss}}{2}\tilde{E}_k, \tag{31}$$

where $\tilde{\kappa}_k = \tilde{F}_k \otimes \tilde{E}_k$. The convolutions are quickly implemented in the time domain by taking the inverse FFT of $\tilde{E}_k$ and $\tilde{F}_k$. This approach accounts for all of the contributions to the optical field while including all FWM terms as well as accounting for the imposed amplitude and phase variations in the signal being amplified by the SOA. ASE can be included, as discussed earlier. Two main advantages of the FFT approach are: (i) the wavelength dependence of the gain is taken into account, while including for all FWM contributions and (ii) spectral-domain calculation of the CH and SHB nonlinear effects allows for longer sampling times for the signal.

2.7. Origin of FWM in SOAs

In most applications of the SOAs, FWM is the key mechanism by which optical signal processing is performed. For this reason, we focus on the origins of FWM in SOAs. This will help the reader in understanding important articles related to FWM in SOAs [16,18,20,38].

Consider the common pump–probe scenario in which the pump field and signal acting as a probe field, E_0 and E_1, are combined and launched simultaneously into an SOA. In practice, the power of the pump beam is much larger than that of the signal, and the two waves have different frequencies (or wavelengths). When two waves with distinct frequencies, ω_0 and ω_1, are present inside an SOA, their beating creates local intensity that varies with time at the difference frequency such

$$|E|^2 = |E_0|^2 + |E_1|^2 + E_0 E_1^* \exp\left[j\left(\omega_0 - \omega_1\right)t\right] + c.c. \tag{32}$$

As the SOA's gain depends on this intensity, the carrier density N is also modulated at the beat frequency $\Omega = \omega_0 - \omega_1$. It is this feature that creates new waves at frequencies that were not present in the original input signal. The first two terms in Eq. 32 are associated with the average intensity of both waves and leads to only gain saturation. However, the two oscillating terms modulate the carrier density at the beat frequency Ω. This modulation, in turn, creates new waves at frequencies $\omega_0 \pm m\Omega$, where m is an integer. The strength of the new waves depends on the ability of the gain medium to respond quickly enough to changes in the carrier density. All of the mediating gain mechanisms, carrier density pulsations, CH, and SHB have temporally limited responses, and therefore cannot respond instantaneously to the wave beating.

An analytical description of FWM inside an SOA is available in Refs. [17,18]. Here we outline the key steps of the derivation. We begin with the rate equation for the carrier density:

$$\frac{dN\left(z,t\right)}{dt} = \frac{I}{eV} - \frac{N\left(z,t\right)}{\tau_S} - \frac{\Gamma a}{A_{eff}\hbar\omega_0}\left[N(z,t) - N_0\right]\left|E(z,t)\right|^2, \tag{33}$$

where the carrier lifetime τ_S is defined as

$$\tau_S = \left(\frac{dR(N)}{dN}\right)^{-1}. \tag{34}$$

We focus on three fields, E_0, E_1, and E_2, corresponding to the pump, signal, and the conjugate created at the new frequency $\omega_2 = 2\omega_0 - \omega_1$, respectively. Taking the pump frequency as the reference frequency , the total field at any point along the SOA is given by

$$E(z) = \left[E_0 + E_1 e^{j\Omega t} + E_2 e^{-j\Omega t}\right] \exp(-j\omega_0 t). \tag{35}$$

As the only generated beating terms in the carrier density occur at the frequency Ω, the carrier density can be written as

$$N(z,t) = \bar{N}(z) + \Delta n(z) e^{-j\Omega t} + \Delta n^*(z) e^{j\Omega t}, \tag{36}$$

where $|\Delta n| \ll \bar{N}$. The optical intensity can also be written as

$$|E|^2 = S_0 + S_1 e^{-j\Omega t} + S_1^* e^{j\Omega t}, \tag{37}$$

where

$$S_0 = |E_0|^2 + |E_1|^2 + |E_2|^2, \quad S_1 = E_1 E_0^* + E_0 E_2^*. \tag{38}$$

We consider pump and signal waves operating within the pump–probe scenario, $|S_1| \ll |S_0|$.

Inserting (36) and (37) into the rate equation (33), and keeping only the dominant first-order terms in Δn and S_1, we obtain:

$$0 = \frac{I}{eV} - \frac{\bar{N}(z)}{\tau_S} - \frac{\Gamma a}{A_{eff}\hbar\omega_0}(\bar{N} - N_0)S_0, \tag{39}$$

$$\frac{d\Delta n}{dt} = -\frac{\Delta n}{\tau_S} - \Gamma a(\bar{N} - N_0)S_1 - \frac{\Gamma a}{A_{eff}\hbar\omega_0} S_0 \Delta n. \tag{40}$$

Equation (39) provides the average carrier density $\bar{N}$ and can be written as

$$\frac{\Gamma a}{A_{eff}\hbar\omega_0}(\bar{N} - N_0) = \frac{\Gamma \bar{g}}{1 + S_0/P_{sat}}, \tag{41}$$

where the unsaturated gain and the saturation power are defined as

$$\bar{g} = Ia\tau_S/eV - aN_0, \qquad P_{sat} = \left(\frac{\Gamma a \tau_S}{A_{eff}\hbar\omega_0}\right)^{-1}. \tag{42}$$

Equation (40) is linear and can be solved using the Fourier transform to obtain

$$\Gamma a \Delta n = -\frac{\Gamma a(\bar{N} - N_0)}{1 + S_0/P_{sat} - j\Omega\tau_S} \frac{E_0^* E_1 + E_0 E_2^*}{P_{sat}}. \tag{43}$$

The evolution of the total electric field is governed by

$$\frac{dE(z,t)}{dz} = \frac{1}{2}\left(-\alpha_L + (1 - j\alpha_H)\Gamma a (N - N_0)\right) E(z,t). \tag{44}$$

Substituting E from (35) and using the preceding results, the signal and conjugate fields are found to evolve as

$$\begin{aligned}\frac{dE_{1,2}}{dz} = {} & \frac{1}{2}\left[-\alpha_L + \frac{(1 - j\alpha_H)\Gamma\bar{g}}{1 + S_0/P_{sat}}\left(1 - \frac{|E_0|^2}{P_{sat}}\frac{1 + S/P_{sat} \pm j\Omega\tau_S}{}\right)\right] E_{1,2} \\ & - \frac{1}{2}\frac{(1 - j\alpha_H)\Gamma\bar{g}}{1 + S_0/P_{sat}} \frac{E_0^2 E_{2,1}^*/P_{sat}}{1 + S/P_{sat} \pm j\Omega\tau_S},\end{aligned} \tag{45}$$

where the minus sign is chosen for E_2. The FWM terms generated by CH and SHB can also be added to this equation [16].

Equation (45) describes the evolution of the signal and conjugate waves along the SOA, while including most important physical effects resulting from gain saturation. Recalling that $E_2 = 0$ initially, the last term is the FWM term that creates the idler wave through modulation of the SOA gain, resulting from the beating between the pump and signal waves. As the pump–signal detuning Ω increases, the strength of the FWM term weakens. A point worth noting is that the presence of the pump not only influences amplification of the signal but also affects its phase through XGM, both of which depend on the detuning Ω. This feature is known as the Bogatov effect and arises from the delay between the pump–signal beating and the resulting modulation of the gain and the refractive index seen by the signal wave; it becomes significant for detunings $|\Omega| \approx \tau_S^{-1}$. The results in Fig. 6(f) show this effect in the strongly differing signal gain for both positive and negative detunings within a few tens of gigahertz from the pump. Typically, when the signal is at a longer wavelength than that of the pump, it experiences larger gain compared with when its wavelength is shorter [18].

As the idler amplitude grows during its amplification inside the SOA, it can acts as a pump and create its own idler. Cascading of this process can lead to multiple waves on both sides of the original pump at frequencies $\omega_m = \omega_0 \pm m\Omega$, where m is an integer. General expression for the FWM term resulting from beating of any three waves is

$$E_{ijk}(\omega_i - \omega_j + \omega_k) = \eta(\omega_i - \omega_j)E_i E_j^* E_k, \tag{46}$$

where η denotes the FWM efficiency. In the case of nondegenerate FWM, all three frequencies are different, and two contributions to E_{ijk} are possible, which correspond to swapping of i and k subscripts. The relative strengths of the two contributions are set by the efficiencies $\eta(\omega_i - \omega_k)$ and $\eta(\omega_k - \omega_i)$.

2.8. Quantum-Well SOAs

As discussed earlier, QW SOAs often perform better because of the quantum confinement of electrons and holes inside a thin layer (thickness $\sim$ 10 nm). The active region of such SOAs contains multiple thin layers of active material (providing gain) embedded within a thicker passive layer. The properties of a QW SOA become different from a bulk SOA, because of changes in the density of states. In practice, the differential gain parameter a becomes larger because there are more electron–hole pairs for the optical field to interact with. As we have seen, this parameters affects the SOA dynamics because the optical gain is proportional to a.

One approach to model QW SOAs is to employ the lumped model developed in this section with a larger value of a and a lower values of τ_S (about 25 ps) that corresponds to the carrier's escape time from the well. It is also useful to modify the dependence of the gain on the carrier density N. In place of the linear dependence as $g = a(N - N_0)$, it is common to use $g = g_0 \ln(N/N_0)$, where N_0 is the carrier density at transparency and g_0 depends on the SOA design.

A more accurate model for the gain in QW SOAs is given in Refs. [39,40] and the gain dynamics considers two rate equations, one for the carriers in the bulk region that are captured by the thin QWs, and the other governing the dynamics of the captured carriers [41]. For the bulk region, the rate equation includes the capture rate R_{cap} as well as the escape rate R_{esc} of the carriers:

$$\frac{dN_b}{dt} = \frac{I}{eV} - R(N_b) - R_{cap} + R_{esc}, \tag{47}$$

where I is the injected current and $R(N_b)$ is the recombination rate in the bulk region. The rate equation in the QW contains the stimulated-emission term that depends on

the total intensity $|E|^2$:

$$\frac{dN}{dt} = R_{cap} - R_{esc} - R_{sp} - g_w(N,\omega)|E|^2, \tag{48}$$

$$\frac{dE}{dz} = \frac{1}{2}\left[(1 - j\alpha_w)\, g\,(N,\omega) - \alpha_L\right] E, \tag{49}$$

where R_{sp} is the rate of spontaneous radiative recombination. As before, the field equation includes the linear loss as well as the amplitude-phase coupling through the parameter α_w.

While a QW SOA responds faster, an useful feature, its saturation power is nearly the same as a bulk device. This can be understood from Eq. 42, where P_{sat} depends on the combination $a\tau_S$. Even though the differential gain a is larger for a QW, τ_S is smaller by nearly the same factor.

2.9. Quantum-Dot SOAs

In recent years, the performance of SOAs has been improved further by confining charge carriers in three dimensions using the so-called quantum dots in which carriers are confined to a spherical region whose radius is about 5 nm. The term quantum dash is used when the shape is like a cylinder. Growing quantum dots on the InP material has proven to be difficult, but considerable advances have been made in recent years in producing quantum-dash devices, and recent advances in quantum-dot technology, especially the shape control and dot uniformity are surmised in Ref. [42]. Models for quantum-dot SOAs can also be used for quantum-dash SOAs with minor changes. For this reason we focus on quantum-dot SOAs only.

We discuss a few concepts needed to understand the gain dynamics in quantum-dot SOAs. Each quantum dot interacts with a narrow band of wavelengths, for which photon energy is close to the energy separation of carriers within that quantum dot, resulting in the so-called homogeneous broadening. However, as the active region in such SOAs contains quantum dots of different sizes, different wavelengths interact with different dots, resulting in a inhomogeneous broadening of the overall gain. Thus, one can use the same model used for a QW device also for a quantum-dot device, after we account for this inhomogeneous broadening. Such a model has the following features.

- One equation, similar to Eq. 47, describes dynamics of the carriers injected into the bulk region that are captured by the individual dots.
- An ensemble of equations, similar to Eq. 48, for each group of quantum dots with nearly the same size.
- An equation for the optical field interacting with each group and adding contributions of all dot groups.

Adapting the quantum-dash model in Ref. [43], we assume that a steady state has been established for carriers within each group of quantum dots and that the electrons only occupy the ground energy state within each dot. The gain of the lth dot group is then found using

$$\frac{dg_l\,(z,t)}{dt} = \frac{g_{l0} - g_l\,(z,t)}{\tau_l^{eff}} - \frac{\Gamma\gamma}{\hbar\omega_0} g_l^{peak} \mathrm{Re}\left[E\,(z,t)\left\{E^*\,(z,t) \otimes L_I\,(t)\right\}\right], \tag{50}$$

where g_{l0} is the peak gain of the lth dot group and τ_l^{eff} is the effective lifetime of a carrier in this group. This time is related to the rates of spontaneous recombination,

capture into the dot, and escape from the dot. These processes occur simultaneously and the effective lifetime is dominated by the fastest process. In Eq. 50 L_l is the impulse response of the homogeneous broadening:

$$L_l(t) = \gamma \exp[-\gamma t + j(\omega_0 - \omega_l)t]\, u(t), \tag{51}$$

where $u(t)$ is the step function, ω_m is the resonant frequency of the lth dot group, and γ is the dephasing rate that determines the spectral width. The field equation takes the form

$$\frac{dE(z,t)}{dz} = \frac{\Gamma}{2}\sum_l g_l(z,t)(1 - j\alpha_H) \otimes L_l(t) - \frac{\alpha_L}{2}E(z,t). \tag{52}$$

ASE noise can also be added as described earlier.

As Eq. 50 has a form similar to that of a bulk SOA, the same nonlinear dynamics occur, albeit faster owing to the faster replenishment of the gain from carriers captured by the dots. As the differential gain is larger for quantum dots compared with bulk and QW devices, the saturation power remains nearly the same.

Summarizing, in this section we have discussed the gain dynamics for bulk, QW, and quantum-dot SOAs. We have paid special attention to FWM because of its critical role in the use of SOAs in optical signal processing. We focused on a dual-polarization, lumped SOA model that is capable of capturing most nonlinear effects that are significant for all-optical signal processing. For situations in which the lumped model may be inadequate, we have provided a traveling-wave model, capable of including the wavelength dependence of the gain as well as the polarization effects. A comparative description of the various bulk SOA models introduced in this paper is given in Table 3. The models are ranked in the order of complexity of implementation and a summary of the applicability of the models is given.

3. SOAS AS INTEGRABLE OPTICAL AMPLIFIERS

The potential of optical amplifiers for compensating losses in optical communication systems was understood soon after such systems were commercialized. SOAs could avoid the need for periodic optical-to-electrical conversion and increase repeater separation. Indeed, as we mentioned in Section 1, SOAs were developed and investigated during the 1980s for this purpose. The situation changed with the advent of the EDFA in 1986 [44]. The huge transmission capacity of today's optical telecommunication systems results directly from the adaption of EDFAs in wavelength division multiplexed (WDM) systems [45–47]. It is also important to note that the EDFAs are agnostic to both the bit rate and the modulation format, which makes them suitable for coherent communication systems. It was shown in 2017 that 179 channels with a net data rate of 65 Tb/s can be transmitted over 6600 km using EDFAs in the C and L bands with a spectral efficiency of 7.3 b/s/Hz, resulting in the per-channel bit rate of 363 Gb/s [46]. Even this experiment covered only about 20% of the full potential (low-loss) capacity of the fiber. Fiber-based Raman amplifiers have been used in recent years because they reduce the noise level in a long-haul communication link, and also allow the use of the S-band [48–50]. Optical parametric amplifiers are being pursued to increase the gain bandwidth of amplifier with minimal noise figure [51].

The question is: what do SOAs offer to remain attractive for optical communication systems? The answer is: *energy efficiency* and *chip-level integrability*. The compactness of the SOA, a small semiconductor chip with electrical connections, is remarkable when compared with the form factors of the other available amplifiers. As discussed in Section 2, SOAs operating in different wavelength bands can be made by changing the constituent material combinations, while providing a gain bandwidth of up to 100 nm.

Table 3. Summary of the Different SOA Models and a Comparison

Model	**Ranking with Respect to the Ease of Implementation**		Gain Dynamics (Implements SPM and XPM)	Wavelength-Dependent Gain	Treatment of FWM	Polarization	Notes
Lumped							
Agrawal and Olsson [15]	1	Fast runtime makes the lumped model highly suitable for system simulation. Can model bidirectional signals.	✓	×	Automatically generated if working with optical field	Can be added	Recommended to be the first SOA model to conduct system simulations.
Mecozzi *et al.* [16,17]	2		✓	×		✓	Similar to [15]; additionally includes intraband contributions to the nonlinear gain
This work, Section 2.4	3		✓	×		✓	Explicitly shows how polarization is included in the system model. Longer time steps permitted because intraband contributions are calculated analytically.
FFT-based							
Summerfield and Tucker [36]	4	Includes wavelength-dependent gain with full wave mixing. Moderately fast runtimes.	✓	✓	✓	Can be added	SOA transient is not calculated, helpful for simulating periodic signals.
Bidirectional							
This work, Section 2.3.2	5	The most accurate of all the SOA models. Slowest runtimes. Spatial discretization defines the temporal sampling care needed with system simulation.	✓	×	Automatically generated if working with optical field	Can be added	Fundamental bidirectional SOA model
Toptchiyski *et al.* [22]	6		✓	✓: Only central frequency of optical field	Implements wavelength decomposition, FWM products need to be included		Includes intraband contributions to the nonlinear SOA gain.
Connelly [13]	7		✓	✓			Fundamental origin of SOA gain based on semiconductor band filling.

However, there is one major difference compared to other amplifiers such as EDFAs. The response time of SOAs, governed by the lifetime of injected carriers is much smaller (nanoseconds to picoseconds) compared with EDFAs. As a result, the SOA's gain reacts to changes in a signal's power at such short time scales. This change in the gain leads to phase fluctuation through the linewidth enhancement factor introduced in Eq. 6. SOA-based amplification also results in bit-pattern effects and the origin of this distortion lies in the slower gain-recovery time of the SOA compared with a symbol's duration. Moreover, SOAs exhibit a higher noise figure and their response is often nonlinear. In this section, we focus on these challenges and their solutions while using SOAs as amplifiers.

Recent work has shown that SOAs can be designed to provide amplification over a wide bandwidth [52]. This, coupled with advances in digital signal processing (DSP) can be useful for amplification of modulated signals in coherent transceivers. However, the nonlinear distortions introduced by the SOAs can be adverse for pluggable transceivers operating with a limited number of channels. Different mitigation techniques have been employed for reducing bit-pattern effects in intensity modulated data, which include the use of symbol rates lower than the inverse of the gain recovery time [53], or the use of quantum-dot SOAs [54]. A digital back-propagation for mitigating SOA-induced nonlinear impairments was proposed and its efficacy was numerically verified in Ref. [55]. Though DSP can also be used for this purpose, an all-optical method is attractive because it reduces the additional processing overhead and the latency in coherent communication systems. In the following sections, we discuss techniques used for reducing amplitude and phase distortions introduced by SOAs.

3.1. SOAs for Long-Haul and Short-Haul Networks

Gain saturation, elevated noise figures, and bit-patterning effects are the primary deterrents for the use of SOA in direct detection WDM systems. In addition to the above, coherent systems suffer from nonlinear phase distortions due to the gain-phase coupling in SOAs.

The use of SOAs as in-line amplifiers was demonstrated in the 1990s using four WDM channels, modulated directly at 10 Gb/s and transmitted over 80 km, both in the 1300-nm band [56] and in the 1550 nm band [57]. In the year 2000, eight WDM channels were modulated at 20 Gb/s and transmitted successfully over 160 km using four SOAs acting as in-line amplifiers [58]. Distance could be increased to 240 km when 8 channels were transmitted at a bit rate of 10 Gb/s [59]. In these demonstrations, SOAs were also used as both power boosters and preamplifiers at the receiver. In another experiment, 32 WDM channels were transmitted over 125 km using SOAs as in-line amplifiers, but the bit rate of each channel was only 2.5 Gb/s [60,61]. Later, the distance could be increased to 325 km for such a 32-channel system [62]. An SOA was used even to add and drop a WDM channel in Ref. [63]. In an access-network experiment, two 1.25-Gb/s channels were successfully transmitted over 26-km of standard single-mode fiber in a duplex mode (to and from an user) using reflective SOAs [64]. Frequency response of a reflective SOA in Ref. [65] revealed a high-pass filter response that suppressed modulations on the reflected seeding light, thus stabilizing the self-seeded output. The authors showed the potential of such a reflective SOA as a cost-efficient solution for WDM passive optical networks (PONs).

A direct-detection system was demonstrated using a bidirectional SOA for the next-generation PONs, where a single SOA is used for upstream pre-amplification and downstream boosting [66]. Figure 7 shows the schematic of the transmitter and receiver designs for such PONs with SOAs playing different roles. The authors of this work also explained the wavelength-dependent performance of the SOAs in the presence of only few WDM channels (four channels). Another recent PON system,

Figure 7

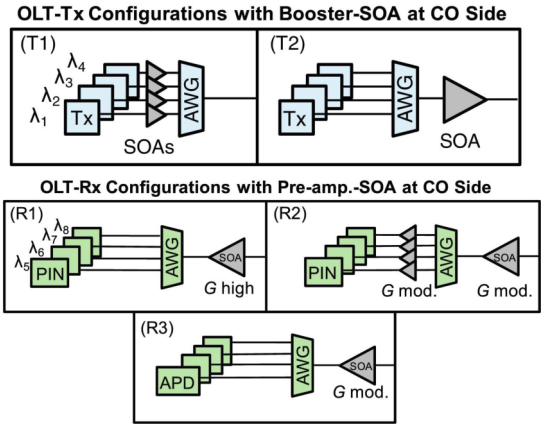

Two transmitter concepts (top) deploying SOAs as power boosters: (T1) one SOA per WDM channel or (T2) a single SOA for all WDM channels. Three receiver configurations with SOAs: (R1) one SOA for all WDM channels followed by an arrayed waveguide grating (AWG) and detectors, (R2) multiple SOAs after AWG as power boosters, or (R3) avalanche photodiodes (APDs) with a single SOA. Reprinted with permission from [66]. © 2015 The Optical Society.

Figure 8

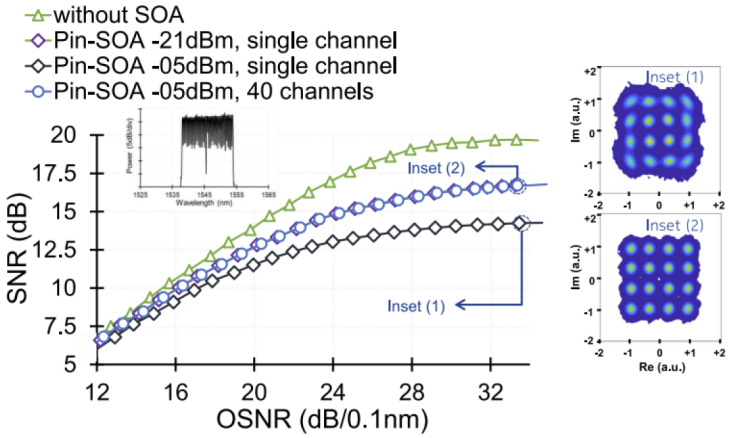

Measured electrical SNR at the receiver as a function of OSNR under three conditions. Constellations of the received data are shown on the right. © 2019 IEEE. Reprinted, with permission, from Renaudier and Ghazisaeidi, J. Lightwave Technol., **37**, 1831 (2019) [52].

operating as bit rates of 50–90 Gb/s, employed SOAs both as preamplifiers and power boosters [67].

Multi-span coherent WDM systems using in-line SOAs for loss compensation were analyzed recently [68]. The use of SOAs as broadband amplifiers in coherent WDM systems has also been studied in detail [52,69–72]. In one study [52], it was found that the nonlinear dynamics of SOAs was not a limiting factor. Figure 8 shows one such result where the electrical signal-to-noise ratio (SNR) measured at the receiver is plotted as a function of OSNR corresponding to the amplification of 16-QAM signals for different SOA input signal power levels and different number of channels. As seen in Fig. 8, increase in input power in a single-channel scenario has resulted in a degradation in the electrical SNR due to gain saturation effect. However, when the number of channels is increased to 40, the electrical SNR is similar to that of a single-channel case at low power levels. It is found that the measured electrical SNR at higher per-channel power improves with an increase in the number of WDM channels from 1 to 40; and the nonlinear distortions seen in the constellations is worse for single channel as compared with 40 channels. This suggests that nonlinear phase distortions do not scale up with the number of WDM channels and makes it possible to employ SOAs as in-line amplifiers in WDM systems making use of all three transmission bands (S, L, and C bands). However, it is still important to understand the origin of nonlinear phase distortions in coherent systems and their compensation techniques.

3.2. Nonlinear Distortion in SOAs and its Compensation

The time evolution of optical gain in an SOA is given as [15]

$$\frac{\partial g}{\partial t} = \frac{g - g_0}{\tau_S} - \frac{g|E|^2}{E_{sat}}, \tag{53}$$

where $E_{sat} = \hbar\omega_0\sigma/a$ is the saturation energy, σ is the mode cross-sectional area, and g_0 is the unsaturated gain, as explained in Section 2.4.

Using $E(z,t) = \sqrt{P(t)}\exp(-j\phi(t))$ in (13), the power P and phase ϕ are found to satisfy,

$$\frac{\partial P}{\partial z} = gP, \qquad \frac{\partial \phi}{\partial z} = -\frac{\alpha_H}{2}g. \tag{54}$$

Figure 9

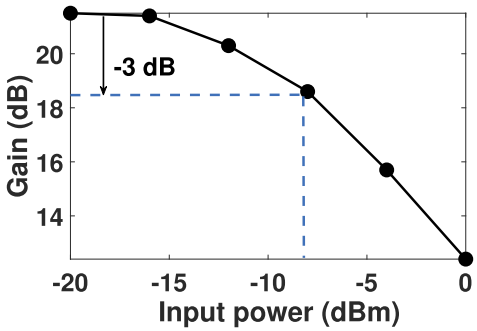

SOA's gain as a function of average power ($\tilde{P}$) of the input signal showing gain's saturation at high power levels.

The steady-state solution of (53) gives

$$g = \frac{g_0}{1 + \tilde{P}/P_{sat}}, \tag{55}$$

where $\tilde{P}$ the average input power and saturation power is defined as $P_{sat} = E_{sat}/\tau_S$.

The gain saturation in one SOA at the applied current of 250 mA is shown in Fig. 9, where the amplification factor $G = P_{out}/P_{in}$ is plotted as a function of P_{in}. When the input signal power is low, amplification is maximum with $G = \exp(g_0 L)$, corresponding to the unsaturated gain coefficient g_0. As G is independent of the input power, amplification occurs without any distortion. In contrast, the gain is saturated at higher input powers. In this case, G becomes a function of input power. Clearly, the operation of an SOA in the saturated regime will produce nonlinear distortion of the amplified signal. Input power level after which nonlinearities become enhanced is about −8 dBm, as indicated by the vertical dashed line in Fig. 9. Two types of signal distortions in the SOA are commonly known as the (a) bit-pattern effect and (b) the nonlinear phase noise.

3.2a. Nonlinear Distortions

The use of SOAs as amplifiers for pulse-amplitude-modulated (PAM) signals is limited by the gain's recovery time and the bit pattern effects resulting from it. Depending on the duration of symbols and the input power, the gain is saturated and its recovery time is governed by the applied current, injected optical power, and several SOA's parameters such as its carrier lifetime and time constants associated with CH and SHB [73].

Figure 10 shows the signal input and output of the SOA when the bit-period is smaller than the gain recovery time. When the gain recovery time is comparable or less than one symbol duration, the carrier density is not able to reach its steady state value between bit transitions. The resulting distortion of the signal is referred to as the bit-pattern effect. The red curve clearly shows such signal distortion due to the bit-pattern effects. In the case of phase-modulated data, distortions are primarily due to the nonlinear phase noise [74]. Even though phase-shift keying (PSK) modulation does not require amplitude changes, in practice, quadrature PSK (QPSK) modulation typically results in amplitude transitions at the symbol boundaries. In addition, amplitude noise generated within the SOA leads to fluctuations in the gain. In the case of 16-QAM and 64-QAM modulations, the amplitude changes occur naturally at the symbol boundaries. A time-varying gain results in an output phase ($\phi_{out}(t)$) different from that of the input phase

Figure 10

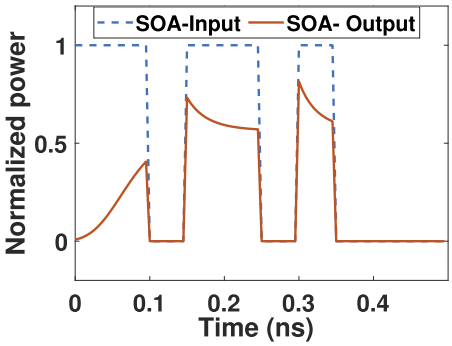

Illustration of the pattern effect in an OOK signal at the output of SOA.

($\phi_{in}(t)$), leading to nonlinear phase noise [15]. The input–output relations for an SOA have the form

$$P_{out}(t) = P_{in}(t)\exp[h(t)], \quad \phi_{out}(t) = \phi_{in}(t) - \frac{1}{2}\alpha_H h(t), \tag{56}$$

where $h(t)$ is the gain integrated over the SOA's length L,

$$h(t) = \int_0^L g(z,t)dz. \tag{57}$$

Equations (56) show that both the power and phase change simultaneously when g fluctuates, resulting in phase distortions.

Gain fluctuations in SOAs are caused by temporal changes in the signal power. Assuming quasi-steady-state condition, where the gain recovery time is faster than each symbol duration, gain fluctuation $\Delta g(t)$ is obtained by differentiating Eq. (55) with respect to $P_{in}(t)$ and is given by

$$\Delta g(t) = -\frac{1}{P_{sat}}\frac{g_0}{(1+\tilde{P}/P_{sat})^2}\Delta P_{in}(t), \tag{58}$$

where $\Delta P_{in}(t) = \tilde{P} - P_{in}(t)$.

For a single channel, this phase distortion is due to SPM and is a nonlinear function of the input power, because the gain experienced by the signal has a nonlinear dependence on its power. For WDM signals with multiple channels, the input power, $P_{in}(t) = \sum_j |E_j(t)|^2$, is a sum of individual channel powers. It is easy to see that power fluctuations in this situation lead to nonlinear phase noise in each channel from a combination of SPM and XPM.

3.2b. Distortion Reduction for Amplitude Modulated Signals

The use of a holding beam was originally proposed through numerical simulations to reduce the bit-pattern effects [75]. Physically speaking, XGM within the SOA owing to the holding beam resulted in minimization of distortions with an amplification penalty of only 4.1 dB. This approach was not pursued further because it was convenient to use EDFAs for amplification. With the recent increase in the use of bands other than the C-band, it has become relevant to explore the compensation of nonlinear distortion in SOAs. Nonlinear filtering based on neural networks was recently demonstrated to mitigate the pattern effects in a 50G PON [76]. The use of a neural-network-based pre-equaliser improved the dynamic range of the receiver and allowed one to realize

29-dB power budget with the FEC limit set at a BER limit of 10^{-2}. This approach becomes computationally expensive, especially at high data rates. The utility of a holding beam for PAM4 modulation is also being explored.

3.2c. Distortion Reduction for Advanced Modulation Formats

Two techniques are discussed here to reduce nonlinear phase distortions induced by SOAs on optical channels carrying data in advanced modulation formats.

3.2d. SOAs with a Holding Beam

The performance of an SOA can be improved by using a holding beam, whose wavelength is significantly different from that of the signal being amplified. In practice, the holding-beam wavelength is chosen to be in the gain-transparency region of the SOA, so that it does not affect its small-signal gain and improves the gain-recovery time [77,78]. A holding beam at the input of the SOA was used in Refs. [79,80] to amplify a three-channel WDM signal at a bit rate of 144 Gb/s or more using 16-QAM and 64-QAM formats. It was found that minimum distortion occurred even at a relatively high gain. The mechanism of nonlinear distortion reduction with a holding beam is similar to that of a gain-saturated SOA with high channel count [52]. The reason is that, for a given channel of interest, other channels can be thought of acting as a broadband holding beam.

In the presence of holding beam, the gain is compressed, and so are the fluctuations in gain. This can be seen by considering the saturated gain $g'(t)$ and its fluctuation $\Delta g'(t)$, in the presence of a saturating holding beam with constant power P_{HB}, it can be written as

$$g'(t) = \frac{g_0}{1 + (\tilde{P} + P_{HB})/P_{sat}} + \Delta g'(t) \approx \frac{g_0}{1 + P_{HB}/P_{sat}} + \Delta g'(t), \tag{59}$$

where the fluctuation $\Delta g'(t)$ in the presence of holding beam is given by

$$\Delta g'(t) \approx -\frac{1}{P_{sat}} \frac{g_0}{\left(1 + P_{HB}/P_{sat}\right)^2} \Delta P_{in}(t). \tag{60}$$

As $P_{HB} \gg \tilde{P}$ in practice, it follows that $g'(t) < g(t)$, leading to an overall reduction in gain. Comparing Eqs. (58) and (60), it is evident that $\Delta g'(t)$ is significantly reduced compared with $\Delta g(t)$. In general, α_H, which is proportional to the variation of phase with respect to gain, is expected to change with gain fluctuations. However, under saturated operation, fluctuations in α_H are also minimal [81]. In the case of a holding beam within the gain spectrum of the SOA, the modulated signal experiences even smaller distortions.

As an example, Fig. 11 shows the measured spectra at the output of the SOA in the presence and absence of the holding beam for a three-channel WDM system [80]. The spectrum at the input of the SOA is also shown for reference. The gain compression owing to the holding beam is 8 dB in this case, resulting in the gain of about 10 dB/channel. In the absence of holding beam, significant nonlinear interaction occurs among the three channels owing to the dynamic gratings formed at the difference frequency of the WDM wavelengths [18], causing FWM, leading to the formation of the side bands in Fig. 11. These are clearly suppressed by the saturating holding beam. The sidebands do appear near the holding beam, but they do not affect the system's performance.

Figure 12 shows the constellations of the center channel at the output of SOA for 16-QAM and 64-QAM formats in three situations: back-to-back (left) without the

Figure 11

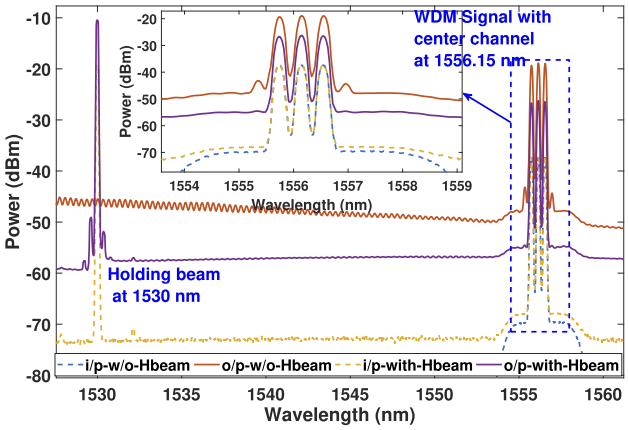

Spectra measured for a three-channel WDM system at the output of the SOA with and without a holding beam. Spectrum at the input of the SOA is also shown for reference. Reprinted from Sobhanan *et al.*, Opt. Commun., **502**, 127331 (2022) [80]. © 2022, with permission from Elsevier.

Figure 12

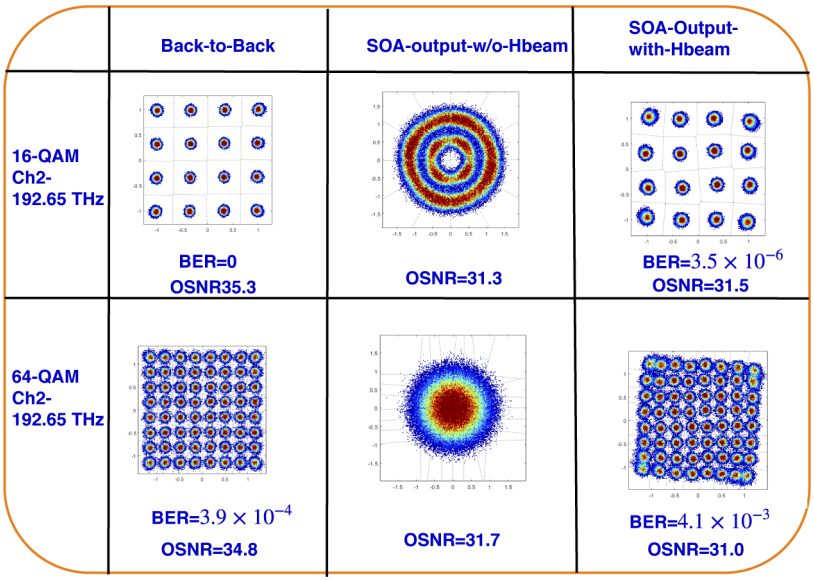

Constellations for the center channel at the output of SOA for 16-QAM (top) and 64-QAM (bottom) formats in three situations when the drive current was 250 mA (Output power ≈ −2 dBm). Reprinted from Sobhanan *et al.*, Opt. Commun. **502**, 127331 (2022) [80]. © 2022, with permission from Elsevier.

holding beam (middle), and with the holding beam (right). Without the holding beam, the phase values are severely distorted, both due to SPM and XPM. In the presence of the holding beam, phase values are nearly restored, and both BER and Q factor are improved significantly. Demodulation is successful with the holding beam, and Q-factor degradation is only about 2 dB.

It is confirmed through independent experiments that even in the linear regime of operation, the holding beam scheme outperforms when (a) the drive current is reduced to achieve the same gain at the same input power as in case with holding beam and (b) the input power is reduced to achieve the same output power at the same drive current

Figure 13

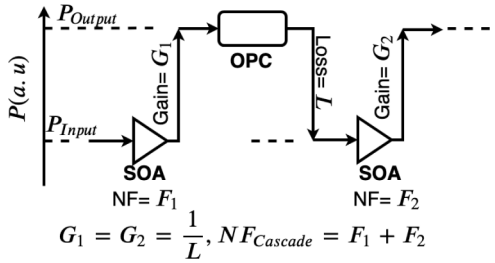

Power distribution map (in the ideal case) indicating the power levels and noise figure at the output of the SOA-NLC scheme. The noise figures F_1 and F_2 are in dB scale. Reprinted with permission from [83]. © 2021 The Optical Society.

as in case with the holding beam. (See the supplementary material in Ref. [80] for details.)

In short, a holding beam provides a simple solution for the reduction of nonlinear phase distortion. However, this improvement occurs at the expense of gain reduction. The use of OPC can provide large SOA gain, while reducing phase distortions. We turn to this scheme next.

3.2e. OPC-based Nonlinear Distortion Compensation

In the scheme discussed in Refs. [82,83], the OPC technique was used to correct nonlinear distortions externally. This work shows that OPC is capable of compensating nonlinear distortions caused by not only the Kerr effect in optical fibers but also those introduced by SOAs. As shown in Fig. 13, two SOAs were used with an OPC stage sandwiched between them so that the combination worked as a low-distortion amplifier. Symbol period was longer than the gain recovery time in these experiments to avoid the bit-pattern effects introduced by SOAs. The distortion symmetry before and after OPC stage is very important for the efficient distortion compensation. Thus, in the experiment, the SOAs which are symmetric in terms of the carrier lifetime, polarization dependence, and wavelength dependence are used in the experiment and the operating points are carefully chosen after a detailed characterization as explained in Ref. [83].

The operation of such OPC combined with an SOA-based nonlinear compensation (SOA-NLC) scheme can be understood as follows. The optical signal from the transmitter is amplified by the first SOA with a distorted constellation. Assuming the signal is not distorted by the pattern effects, the output field after the first SOA can be written as [52]

$$E_i'(t) = E_i(t) \exp\left[\frac{1}{2}(1 - j\alpha_{H1})h_1(t)\right], \tag{61}$$

where α_{H1} is Henry's linewidth enhancement factor, $h_1(t)$ is the integrated gain coefficient, and $G_1 = \exp[h_1(t)]$ the power gain of the first SOA. This equation ignores both the wavelength dependence [84] and the polarization dependence [85] of $h_1(t)$ but its use is justified for the three-channel experiment. The influences of SHB, CH, and two-photon absorption [86] are also not considered because they had a negligible effect under the conditions of this experiment.

Any time-dependent change in the amplitude of input signal results in a corresponding change in the gain, which in turn produces nonlinear phase modulation. As $h_1(t)$ acts as the homogeneously broadened gain shared by all WDM channels, both SPM and XPM are present in a WDM system. OPC is used to compensate for the distortions

induced by such nonlinear phase modulations. The electric field after the OPC stage, under ideal conditions, can be written as

$$E_i'^*(t) = E_i^*(t)\exp\left[\frac{1}{2}(1+j\alpha_{H1})h_1(t) - \alpha_{loss}\right], \tag{62}$$

where $E_i^*(t)$ denotes the conjugate of the electric field of the input signal, α_{loss} is the loss coefficient such that $\exp(-2\alpha_{loss})$ represents the loss of the OPC stage. The field at the output of the second SOA is given by

$$E_o(t) = E_i'^*(t)\exp\left[\frac{1}{2}(1-j\alpha_{H2})h_2(t)\right], \tag{63}$$

where the subscript 2 stands for the second SOA. If we assume that both SOAs are identical and operated at the same drive current, the output can be written in a simple form as

$$E_o(t) = E_i^*(t)\exp[h_1(t) - \alpha_{loss}]. \tag{64}$$

If we ensure that $G_1 = \exp(2\alpha_{loss})$, the output of SOA-NLC combination can be expressed as

$$E_o(t) = E_i^*(t)\exp\left[\frac{1}{2}h_1(t)\right]. \tag{65}$$

Thus, the SOA-NLC scheme offers the same power gain as the single-SOA scheme but without the phase distortions. Note that ASE noise added by both SOAs is not included in the preceding discussion. The bit-pattern effects are also ignored.

In the presence of the bit-pattern effects, the envelope of the output field after the first SOA changes from its input shape. The OPC stage reverses only the phase, leaving the envelope intact. The envelope is further distorted after the second SOA, invalidating the requirement that $h_1(t)$ should be equal to $h_2(t)$. In other words, envelope changes do not allow the second SOA to cancel nonlinear distortions induced by the first SOA, hampering the effectiveness of the OPC stage.

The scheme requires the two SOAs to operate at the same gain. For this reason, the loss of the OPC stage must not be larger than the gain of either of the SOAs. For experiments investigating different input power levels, the loss of the OPC stage should be manually adjusted to maintain the requisite gain-loss condition. Through a detailed characterization of two SOAs, it is possible to find a suitable operating point that satisfies the gain-loss condition. As shown in Fig. 13, considering OPC as a loss element ($L = \exp(-2\alpha_{loss})$) together with the gain-loss condition $G = G_1 = G_2 = 1/L$, the total noise figure (NF) is approximately NF $= F_1 + F_2$, where F_1 and F_2 are the noise figures of the two SOAs.

The results for a three-channel WDM system in the back-to-back configuration are shown in Fig. 14 . Same input power and drive current ($I_{drive} = 150$ mA) are maintained at both the SOAs. Input signal power was −14.5 dBm, corresponding to an operating regime where the signal is expected to undergo nonlinear distortions. The input and output spectra after the SOA and at the OPC stage are shown. The constellations for channel 1 at different stages of the experiments for the first WDM channel are also shown. The constellation is distorted considerably after the first SOA because of nonlinear distortions, but it is laterally inverted after OPC because of the phase-conjugation effect. After the second SOA, a constellation without nonlinear distortion is obtained. The gain (per channel) was ≈18 dB for both SOAs. The OSNR after the second SOA was reduced by about 3.2 dB, but the data could be recovered, thanks to OPC, despite the nonlinear distortions and noise added by two SOAs. This approach provides performance improvement (in terms of the BER and the Q factor)

Figure 14

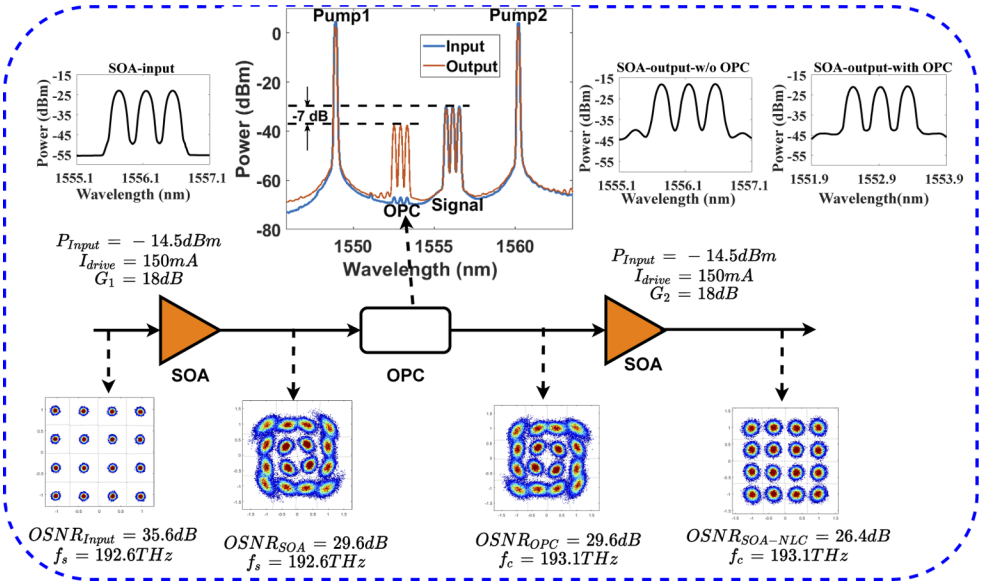

Optical spectra at the input and the output of the SOA, with and without OPC, for a three-channel WDM system. The input and output spectra of the OPC stage are also shown. Constellations for channel 1 at different stages are shown at the bottom for $P_{in} = -14.5$ dBm and $I_{drive} = 150$ mA. Reprinted with permission from [83]. © 2021 The Optical Society.

over the single-SOA approach, despite the additional ASE noise added by the second SOA.

We now provide a comparison between two nonlinear phase-distortion compensation techniques discussed in this section. The OPC-based method compensates for the nonlinear phase distortion without gain reduction. However, the major hurdles in the practical use are (a) the gain-recovery time of the SOA limits the possible highest symbol rate and (b) complexity in implementation. In terms of complexity, and hence energy efficiency, the holding beam technique is preferred as it requires only an additional laser source. If the requirement is such that the distortion needs compensation irrespective of the gain reduction, the holding beam technique is the simplest method. It can also support a larger symbol rate than the inverse of gain-recovery time of the SOA in use.

4. ALL-OPTICAL WAVELENGTH CONVERSION

There is an ever-increasing demand for the bandwidth over which data can be transmitted through optical networks. To address this demand, optical networks are always exploring ways and methods to squeeze more bits within the available bandwidth. Current networks use amplitude, phase, and polarization of the optical carrier to encode information. Future networks may utilize different spatial modes of an optical fiber to encode information, a scheme known as space-division multiplexing. All such efforts are trying to increase the number of bits per hertz, thereby increasing the efficiency of bandwidth utilization. In addition, there are efforts to make the definition of a channel more fluid to increase the efficiency further.

Ensuring flexible bandwidth and using all degrees of freedom to pack more bits per hertz appear to be important for a network's efficiency. However, data over optical channels often needs to travel hundreds of kilometers before arriving at its destination.

Figure 15

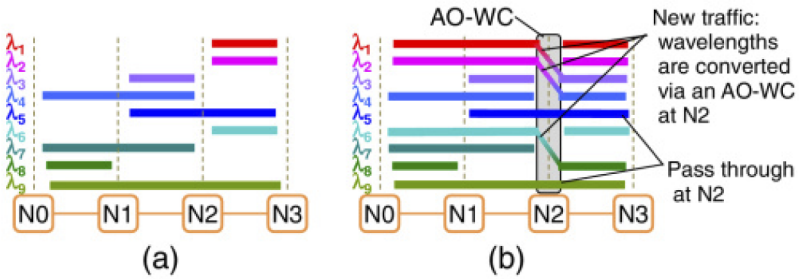

Illustration of (a) static wavelength allocation and (b) dynamic wavelength allocation enabled with wavelength conversion. Reprinted with permission from [87]. © 2018 The Optical Society.

During this process, light has to propagate through multiple nodes shared by different networks. In a static optical network, wavelengths are assigned so that each wavelength remains unique from end to the other end. This is highly inefficient in practice for long-haul networks. In addition, when one node has to communicate with another node, it needs to ensure that the same wavelength is unique at both nodes [87]. A wavelength converter solves this problem and allows the reuse of wavelengths. The illustration of the difference between the static and dynamic wavelength allocation is shown in Fig. 15.

All-optical wavelength conversion of WDM channels permits dynamic allocation of wavelengths within the optical layer [88,89]. From a network perspective, wavelength conversion reduces the blocking probability in wavelength switched networks [90]. An all-optical wavelength conversion has all the advantages of an all-optical network because it can be transparent to both the bit rate and the modulation format. In addition, it has the advantage of being energy efficient when complex modulation formats are used. The understanding of the physical layer, particularly of the nonlinear processes used for wavelength conversion, is very important to design, efficient WDM systems. Among various nonlinear processes utilized for all-optical wavelength conversion, the phenomenon of FWM is most widely used [91]. FWM is attractive because it provides transparency to the modulation formats and bit rates with a relatively large and uniform conversion efficiency [92]. FWM process has been historically studied in various media such as optical fibers, silicon waveguides, and semiconductor crystals [93]. SOAs provide a viable solution because they require much lower pump powers compared with such alternatives.

4.1. Nonlinear Processes Utilized for Wavelength Conversion

Even though wavelength conversion can be done in the electrical domain by recovering the electrical data with a receiver and re-transmitting it at another wavelength, such a scheme is costly and inefficient in terms of energy consumption. There are several all-optical methods that do not require conversion to the electrical domain. They make use of nonlinear optical processes within an SOA such as XGM, XPM, and FWM [94,95].

4.1a. Cross-Gain Modulation

In XGM, a pump beam modulates the gain of the SOA, and the modulated gain is experienced by the probe beam at a different wavelength. Thus, the probe beam amplification depends on the power level of the pump beam, leading to wavelength conversion. This is illustrated in the Fig. 16, where the output power at 1539 nm is

Figure 16

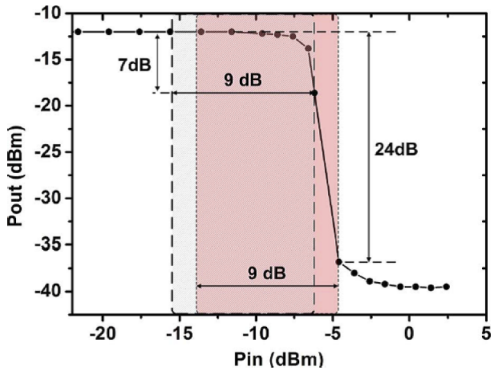

Wavelength conversion through XGM. Output power at 1539 nm is plotted against input power at 1525 nm. © 2009 IEEE. Reprinted, with permission, from Kapsalis *et al.*, IEEE Photon. Technol. Lett. **21**, 1618 (2009) [96].

Figure 17

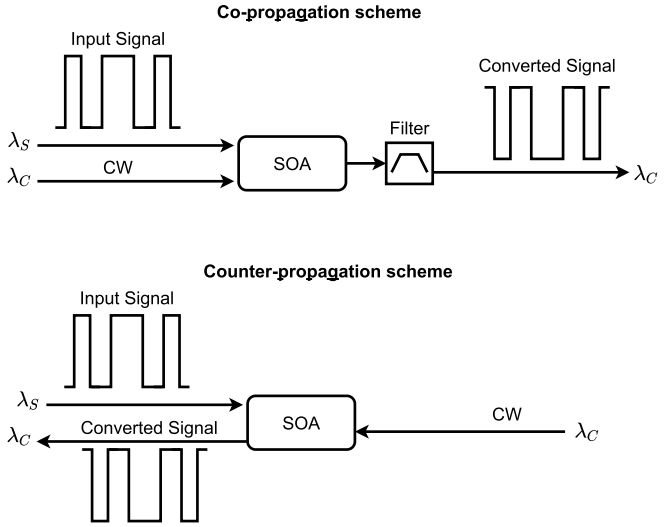

Schematic showing co-propagating and counter-propagating schemes for wavelength conversion through XGM.

plotted for different values of input power at 1525 nm [96]. When the input power is sufficiently high (> -5 dBm in this case), the overall gain experienced by the SOA is saturated, resulting in a very small output power (−40 dBm). When the input power is lower than −7.5 dBm, the output power of −12.5 dBm corresponds to the case of unsaturated gain.

The pump and the signal need to be simultaneously propagating inside the SOA to realize XGM. As shown in Fig. 17, this can be done in two ways: in the (1) co-propagating mode where the pump and probe beams propagate in the same direction or in the (2) counter-propagation mode where the pump and probe beams propagate in the opposite directions [95]. Counter-propagating scheme has the advantage that it does not require an optical filter at the output.

Implementation of XGM-based wavelength conversion requires two conditions: (1) the data should be encoded in the amplitude level of the pump beam; and (2) the bit-rate of the pump should be lower than the gain-recovery time of the SOA. Thus,

the SOA acts like a high-pass filter for the pump beam and a low-pass filter for the probe beam.

In summary, the main advantages of XGM-based wavelength conversion is that it can be used for the broadband wavelength conversion of amplitude-modulated data, including multi-level PAM signals [97]. It is fairly bit-rate independent within the bandwidth of the SOAs. It is also polarization insensitive if the gain of the SOA is polarization insensitive. XGM can also be utilized with minimal signal degradation [96]. However, XGM-based wavelength conversion is not format-agnostic and works only for amplitude-modulated data.

4.1b. Cross-Phase Modulation

In the case of XPM, the phase of one signal is modulated by variations in the amplitude of an another signal in the same SOA. The power-dependent gain and gain-dependent phase variations are reasons for the XPM process in SOAs, as discussed in Section 2. Wavelength conversion through XPM is carried out in SOAs by employing a Mach–Zehnder interferometer (MZI) configuration [98–100]. Such a device (called SOA-MZI) was used during the 1990s for wavelength conversion [99]. In this work, SOAs were monolithically integrated using a symmetric MZI to form a compact, polarization-insensitive, all-optical wavelength converter capable of operating at up to 10 Gb/s. A CW signal at the desired output wavelength was launched into the MZI, where it was first split, passed through an SOA, and then recombined. The output of the device depended on the phase difference $\triangle\phi$ in the two arms of the MZI. The SOAs in the two arms controlled this phase difference through the bias current. The dynamic range of the input power available for wavelength conversion depends on the linewidth enhancement factor α_H of the SOAs used. This range can be enhanced by appropriately selecting the wavelength of the probe and the bias current for the phase control. Wavelength upconversion into the millimeter-wave frequency band was demonstrated in 2004 using a SOA-MZI device [98]. A higher dynamic range obtained in this experiment was suitable for mobile communication systems. One of the advantages of the XPM-based approach is that it allows chirp-free operation. However, the entire structure needs to be monolithically integrated for stable operation. Moreover, this technique is not modulation transparent and works only for amplitude-modulated signals.

4.1c. Four-Wave Mixing

The most widely used method for wavelength conversion using SOAs is based on the FWM phenomenon. The mechanism of FWM in SOA is discussed in detail in Section 2.7. The main reason behind the attractiveness of FWM for wavelength conversion is that FWM is a coherent and fast-responding process where a pump beam allows the transfer of all properties of the input signal to a new idler wave generated inside a nonlinear medium. An SOA is an attractive nonlinear medium for FWM because it provides a high conversion efficiency [101], as discussed in Section 2.7. FWM occurs in SOAs through modulation of the carrier density, CH, and SHB [102] (see Section 2.7). When employing an SOA for FWM, it is important to understand and mitigate any degradation effects. Considerable work has been done to characterize and mitigate such effects [103–106].

It is also important to understand the impact of SOA on the wavelength conversion process because SOAs can degrade both the amplitude and phase of the signal. This is in addition to the degradation by the FWM process, if the operating conditions, SOA's driving current and the pump power, are not selected properly. When an SOA is operated at high driving currents to provide more gain and a higher conversion efficiency, it also degrades the OSNR of the converted signal. Similarly, a high pump

Figure 18

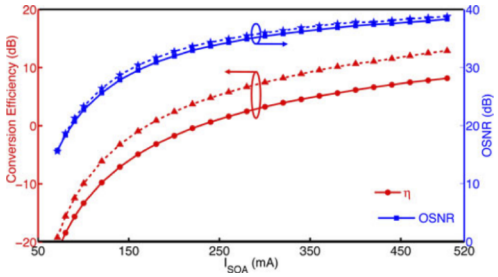

Conversion efficiency and OSNR as a function of I_{SOA} for $\triangle\lambda$ = 0.5 nm at a pump power of −3.3 dBm (dashed curves) and +0.3 dBm (solid curves). Input signal power was −10 dBm. © 2012 IEEE. Reprinted, with permission, from Baveja *et al.*, IEEE J. Sel. Topics Quantum Electron. **18**, 899 (2012) [107].

power can lead to gain saturation and reduce conversion efficiency. At the same time, it is also important to ensure that the pump power is high enough to slightly saturate the SOA and, thus, avoid the patterning effect. The wavelength difference between the pump and the signal also affects the OSNR, and hence the quality of the wavelength-converted idler. A detailed analysis of the conversion efficiency and the idler's OSNR was carried out in Ref. [107]. As an example, Fig. 18 shows the measured conversion efficiency and the corresponding OSNR for a specific SOA at different drive currents and two pump power levels for a fixed pump–probe detuning of 0.5 nm. It can be seen that the OSNR and the conversion efficiency are increased with increase in drive current. It is also interesting to note that the conversion efficiency is reduced when the SOA is highly saturated with 0.3 dBm pump power as compared with that of −3.3 dBm. Thus, as discussed, optimization of the pump–probe power levels play significant part in the quality of the wavelength-converted signal. Further research has been done to find the optimum SOA settings for the best conversion efficiency, while degrading the converting signal the least [103,105,108].

4.2. Signal Fidelity During Wavelength Conversion

4.2a. Amplitude

To study the fidelity of an amplitude-modulated signal at 10 Gbps, the signal was launched together with the pump into the SOA to initiate FWM. Polarization controllers were used to align the states of polarization of the pump and the signal. At the SOA's output we used optical filters to separate the signal and the idler and passed them through a noise-loading stage to vary the OSNR. An avalanche photodetector (APD) was used for BER measurements and an optical spectrum analyzer (OSA) was used to measure the OSNR of the wavelength-converted idler. Figure 19 shows the measured spectrum together with the filtered spectra of the signal and the idler.

The BER of the signal and the idler was measured as a function of OSNR, and the results are shown in Fig. 20. It can be seen that there is almost no OSNR penalty compared with the back-to-back configuration (no SOA). The average signal power was 0.1 mW at the input of the SOA. More importantly, the required pump power was only 1 mW in this experiment. Even at such a small pump-power level, the conversion efficiency was more than 100% because of the gain provided by the SOA. The effects of stimulated Brillouin scattering, which is a major bottleneck in using fiber-based converters, are also absent when SOAs are used for FWM. Penalty-free all-optical wavelength conversion of 10-Gb/s data was realized using FWM inside a nonlinear SOA.

Figure 19

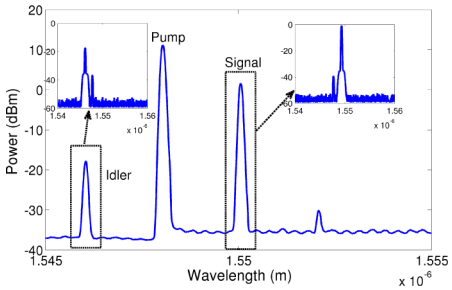

Measured spectrum at the output of the SOA used for FWM. Insets show the filtered spectra of the signal and the idler.

Figure 20

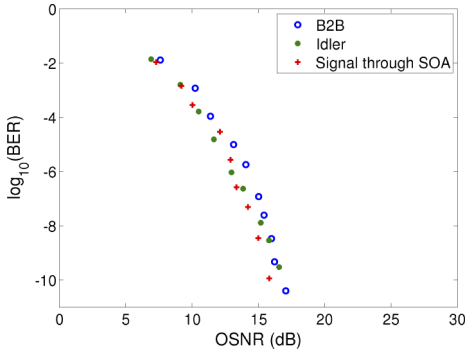

Experimental results of all-optical wavelength conversion at 10 Gb/s through FWM in a nonlinear SOA.

4.2b. Phase

Signal phase was also modulated in advanced formats simultaneously with the amplitudes to increase the spectral efficiency of coherent communication systems [109]. In such a case, it is essential that a wavelength converter does not add phase noise during the conversion process. Spectral broadening of the idler during FWM was observed as early as 1978 [110] and later studied in detail in Ref. [104]. Several schemes have been suggested to prevent such spectral broadening. One approach involves modulate the phase of the pump [111,112]. Another approach makes use of two pumps and dithers their phases in opposite directions [113–116]. Such schemes indirectly rely on producing a specific phase shift between the two pumps. Spectral broadening is also an issue when FWM is used for creating a frequency comb. It has been recently shown that spectral broadening during comb generation can be prevented when the seed frequencies have correlated phase noise [117]. However, correlation of phase noise between an "incoming" signal and a "local" pump is difficult in practice.

A new scheme based on correlated pumps was demonstrated in Refs. [32,103]. Figure 21(a) shows the spectral representation of a partially degenerate FWM scheme in which mixing of the pump and signal waves (frequencies ω_p and ω_s) creates the Stokes and anti-Stokes waves at frequencies

$$\omega_{St} = 2\omega_p - \omega_s, \qquad \omega_{a-St} = 2\omega_s - \omega_p. \tag{66}$$

The linewidths of these two FWM components is found to be [104]

$$\Delta\omega_{St} = 4\Delta\omega_p + \Delta\omega_s, \qquad \Delta\omega_{a-St} = 4\Delta\omega_s + \Delta\omega_p. \tag{67}$$

Figure 21

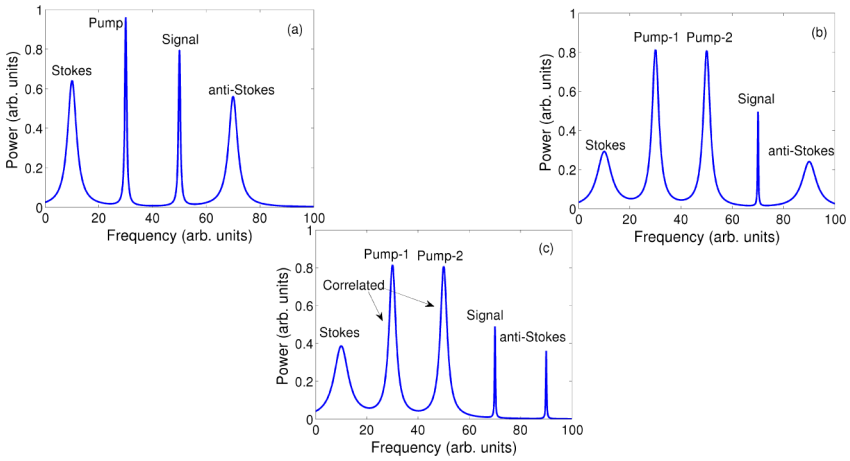

Spectral representation of (a) partially degenerate scheme, (b) nondegenerate scheme with the two pumps without correlated phase noise, and (c) nondegenerate scheme with the two pumps having correlated phase noise. Reprinted from [103]. © 2013 The Optical Society.

For the case where $\omega_s<\omega_p$, these relations are interchanged for the Stokes and the anti-Stokes frequencies. In the case of nondegenerate FWM with two independent pumps, as represented in Fig. 21(b), the frequencies become

$$\omega_{St} = \omega_{p1} + \omega_{p2} - \omega_s, \qquad \omega_{a-St} = \omega_{p1} - \omega_{p2} + \omega_s. \tag{68}$$

In this case, phase variance becomes

$$\sigma^2_{\Delta\theta-St/a-St} = \sigma^2_{\Delta\theta-p1} + \sigma^2_{\Delta\theta-p2} + \sigma^2_{\Delta\theta-s}, \tag{69}$$

where ω_{p1} and ω_{p2} represent the frequencies of the two pumps, and the respective $\Delta\theta$ represent phase errors due to their phase noise. The corresponding linewidth becomes

$$\Delta\omega_{a-St/St} = \Delta\omega_s + \Delta\omega_{p1} + \Delta\omega_{p2}, \tag{70}$$

with $\Delta\omega_{p1}$ and $\Delta\omega_{p2}$ representing the linewidths of the two pumps. The general phase error variance relations for the Stokes and anti-Stokes components are

$$\begin{aligned}\sigma^2_{\Delta\theta-St} =& \sigma^2_{\Delta\theta-s} + \sigma^2_{\Delta\theta-p1} + \sigma^2_{\Delta\theta-p2} + 2\mathrm{Cov}(\Delta\theta_{p1}, \Delta\theta_{p2}) \\ &- 2\mathrm{Cov}(\Delta\theta_{p2}, \Delta\theta_s) - 2\mathrm{Cov}(\Delta\theta_{p1}, \Delta\theta_s),\end{aligned} \tag{71}$$

$$\begin{aligned}\sigma^2_{\Delta\theta-a-St} =& \sigma^2_{\Delta\theta-s} + \sigma^2_{\Delta\theta-p1} + \sigma^2_{\Delta\theta-p2} - 2\mathrm{Cov}(\Delta\theta_{p1}, \Delta\theta_{p2}) \\ &- 2\mathrm{Cov}(\Delta\theta_{p2}, \Delta\theta_s) + 2\mathrm{Cov}(\Delta\theta_{p1}, \Delta\theta_s),\end{aligned} \tag{72}$$

where Cov() represents the covariance of two random variables (phase errors in each wave in this case).

When the two pumps in the nondegenerate scheme are correlated, $\mathrm{Cov}(\Delta\theta_{p2}, \Delta\theta_{p1}) = \sigma^2_{\Delta\theta-p1} = \sigma^2_{\Delta\theta-p1}$ and $\mathrm{Cov}(\Delta\theta_{p1/p2}, \Delta\theta_s) = 0$, thereby giving respective linewidth of the anti-Stokes and Stokes as

$$\Delta\omega_{a-St} = \Delta\omega_s, \qquad \Delta\omega_{St} = 4\Delta\omega_{p1/p2} + \Delta\omega_s. \tag{73}$$

It is observed from (73) that the anti-Stokes component retains the linewidth, i.e., the phase noise of the signal when the two pumps in the nondegenerate scheme are correlated.

Figure 22

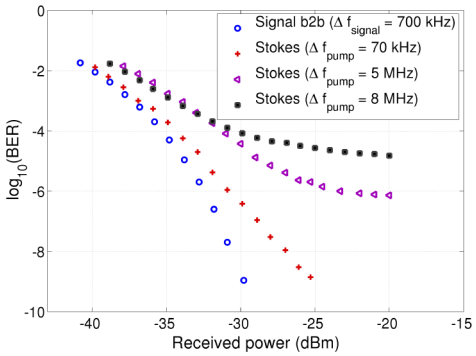

BER as a function of received power for the DQPSK data format in four cases. DFB laser used for the signal had 700-kHz linewidth and MGY laser used as pump had 5 or 8 MHz linewidth. Reprinted from [103]. © 2013 The Optical Society.

The effect of these results was explored by performing all-optical wavelength conversion on a 10.7-GBaud DQPSK data signal [103]. The partially degenerate pumping scheme was initially tested using pump lasers with different phase noise values. The pump with the largest phase noise was used for generating correlated pumps to demonstrate the effectiveness of the dual-correlated pumping scheme.

Figure 22 shows the measured BER for different received powers of the signal (measured back-to-back), Stokes, and the anti-Stokes components for the partially degenerate FWM scheme. The laser used to generate the DQPSK signal was a DFB laser with a linewidth of about 700 kHz. The experiment was carried out using pump lasers of different linewidths, with $\omega_s > \omega_p$ in all the cases. The pump used was either an external cavity laser (ECL; linewidth 60 kHz) or a wavelength-tunable, modulated grating, Y-branch laser (MGY; linewidth 5 MHz). To increase the linewidth, the MGY laser was tuned from ITU-T grid channel 40 (5 MHz linewidth) to channel 38 (8 MHz linewidth). When the linewidth of the pump was increased, a penalty was observed for the Stokes component as expected. It was also observed that the pump with a larger phase noise results in an error floor for the Stokes component. The error floor increased from 1×10^{-6} to 1×10^{-5} when the pump linewidth was changed from 5 to 8 MHz, whereas a BER lower than 1×10^{-9} was obtained when pump's linewidth was 60 kHz.

The dual-correlated pumping scheme was tested next with the tunable modulated-grating Y-branch (MGY) laser operated at a linewidth of 8 MHz. The signal at the input, the signal through SOA, Stokes, and the anti-Stokes component are filtered independently and their BER characteristics were shown as a function of received power in Fig. 23. It was observed that the BER of the anti-Stokes component was exactly identical to that of the signal. The BER corresponding to the Stokes component was found to result in an error floor of approximately 1×10^{-4}. These BER results were as expected from Eq. 73. It was experimentally verified that phase noise from the pump is not transferred to the generated wavelength, irrespective of the type of phase noise (frequency dependent/independent), and wavelength conversion can occur without performance degradation. This concept was also tested using a QPSK signal for wavelength conversion [118]. Here the effect of nonlinear phase noise on wavelength conversion using dual-correlated pumps was studied. It was shown that there are OSNR requirements on the dual-correlated pumps for penalty-free wavelength conversion. It was also shown that the nonlinear phase noise generated in the SOA was transferred to the idler because of the uncorrelated nature of the amplitude noise

Figure 23

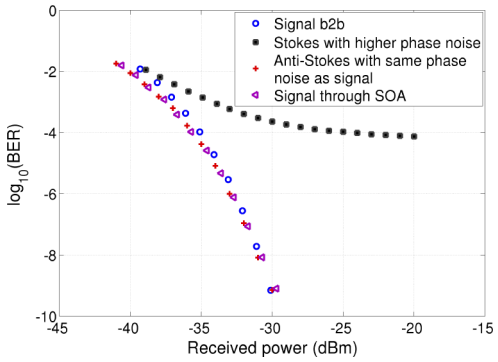

BER as a function of received power using dual correlated pumps (linewidth 8 MHz). DFB laser used for the signal had 700-kHZ linewidth. Reprinted from [103]. © 2013 The Optical Society.

Figure 24

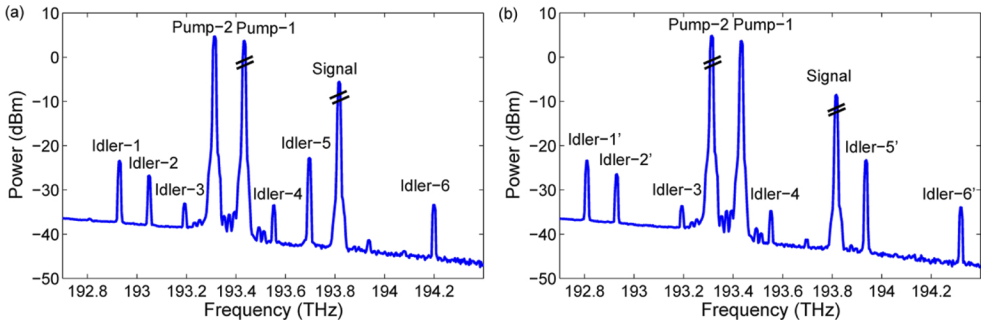

Spectrum at the SOA's output when signal's state of polarization is parallel to that of (a) pump 1 or (b) pump 2. Reprinted from [105]. © 2016 The Optical Society.

for the pump signals. Such distortion reduction techniques were further investigated in Refs. [108,119].

4.2c. Polarization

Generally, polarization independence is realized using a polarization diversity scheme by employing two independent SOAs as wavelength converters for the orthogonal polarizations. However, it is possible to achieve polarization-independent wavelength conversion of polarization multiplexed signals using FWM inside a single SOA [105]. The authors verified the vector theory of FWM by making the polarization of the pump either parallel or perpendicular to the polarization of the signal and identifying the frequency of the generated idlers. Figure 24 shows the optical spectra recorded in these two cases.

When the two pumps are parallel polarized, the idler corresponding to $\omega_{p1} - \omega_{p2} + \omega_s$ is a frequency-shifted version of the signal preserving the polarization multiplexed data in the signal. Physically, this process can be perceived as a grating formed by beating of the two pumps, which transfers the signal to the idler frequency. Mathematically, when the two pumps are parallel polarized, the FWM at the frequency $\omega_{p1} - \omega_{p2} + \omega_s$ can be expressed as a unitary transformation. It is also interesting that this idler frequency preserves the phase noise of the signal (no phase noise transfer from the pumps to the signal). In another experiment, wavelength conversion of polarization multiplexed signal was realized using a single SOA, and the results are shown in Fig. 25. No

Figure 25

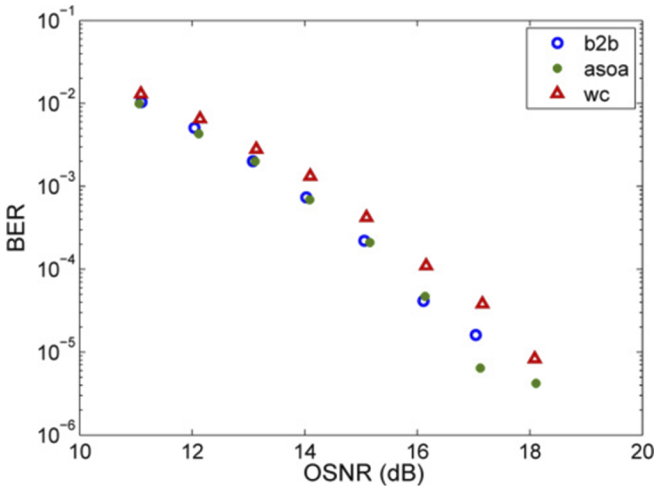

BER as a function of OSNR for the input signal (b2b), signal after SOA (asoa), and wavelength-converted signal (wc) for a polarization-multiplexed QPSK signal at 12.5 GBaud. Reprinted from [105]. © 2016 The Optical Society.

Figure 26

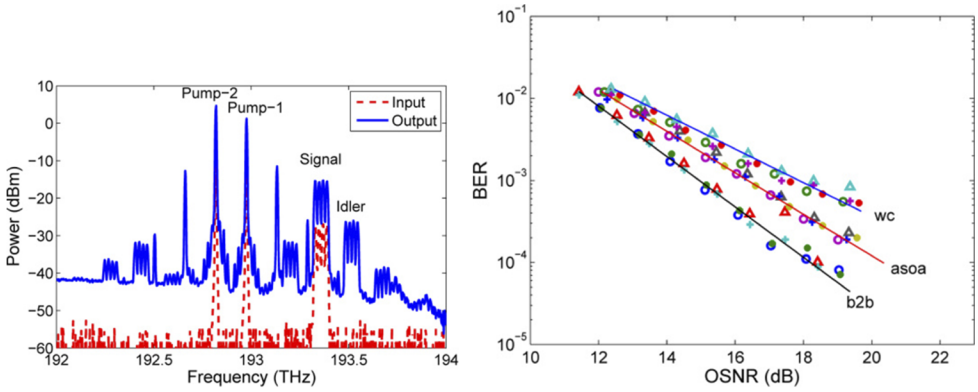

(a) Optical spectra at the input and output of the SOA for wavelength conversion of a 12.5 GBaud four-channel Nyquist PM-QPSK superchannel. (b) BER as a function of OSNR for the input signal (b2b), the signal after SOA (asoa), and the wavelength-converted signal (wc) for four-channel Nyquist WDM super-channel modulated with PM-QPSK signals at 12.5 GBaud. Reprinted from [105]. © 2016 The Optical Society.

penalty was observed between the back-to-back case (b2b, before SOA), the signal after the SOA (asoa), and the wavelength-converted signal (wc).

The wavelength conversion of polarization-multiplexed Nyquist superchannels has also been implemented using SOAs [105]. The optical spectra at the input and output of the SOA are shown in Fig. 26(a). It can be seen that there is a degradation of the OSNR when the signal passes through the SOA. The BER as a function of OSNR is also shown in Fig. 26(b) for the signal before SOA, signal after SOA, and the wavelength-converted signal. There is a degradation of the Nyquist superchannel when it passes through the SOA, which is due to the effect of the nonlinear phase noise from the SOA [118]. The degradation of the idler is worse because of the transfer of this noise from the signal, and the additional nonlinear phase noise generated on the idler. This can be

Figure 27

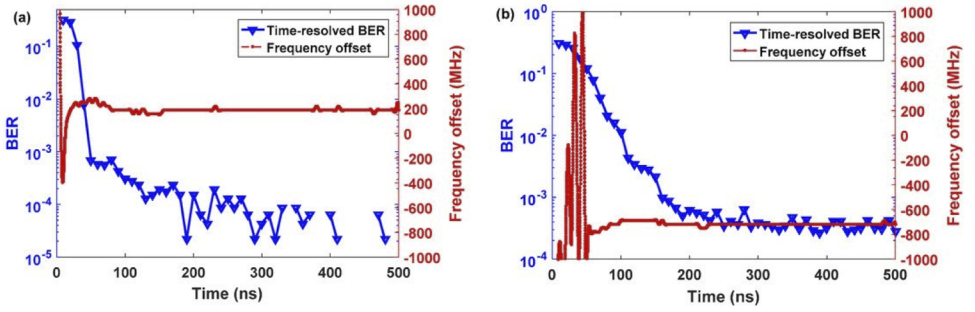

(a) (b)

Switching characteristics of a FWM-based wavelength converter. Time-resolved BER and frequency offset curves for (a) a QPSK signal and (b) a PM-QPSK signal at 12 GBaud, when the wavelength of the received idler is at the first channel on the ITU grid. Reprinted from [122] under a Creative Commons license.

mitigated by using higher pump powers. However, this will lead to lower conversion efficiency and a lower OSNR. DSP at the coherent receiver may be used to mitigate this nonlinear phase noise.

4.3. Fast Re-Configurable Wavelength Conversion

To deploy a FWM-based wavelength-conversion scheme, it is critical to understand the time required for switching the wavelengths by the SOA employed. In several studies [120–122], a gain-switched distributed Bragg reflector (SGDBR) laser was used to study the switching dynamics of an SOA-based wavelength converter. A wide tuning range (>10 nm) and less than 50 ns and 160 ns reconfiguration time was achieved for the wavelength conversion system for QPSK and PM-QPSK signals, respectively. The effect of switching of the pump laser was studied on the BER performance of the wavelength-converted idler at a wavelengths of 1541 nm (corresponding to pump wavelength of 1548 nm) and 1539 nm (corresponding to pump wavelength of 1554 nm) for QPSK and PM-QPSK signals at 12.5 GBaud. The results are shown in Fig. 27. The time-resolved BER values are obtained by averaging over 125 symbols (10 ns) and 200 switching events after wavelength switching. Signal was at 1542.5 nm from a low-phase-noise ECL with a linewidth of tens of kilohertz. The output of a coherent receiver output was sampled at 50 GHz for the DSP [105]. A study of the time-resolved BER, in comparison with the frequency offset between the local oscillator laser and the wavelength-converted idler, was also presented in [122]. It was found that BER can go below the FEC limit (10^{-3}) when the time taken for frequency stabilization of the pump was 50 ns for a QPSK signal and 160 ns for a PM-QPSK signal, respectively.

For a better understanding of the re-configurable nature of wavelength converters, a study of the BER as a function of OSNR variations of the received signal after 50 and 160 ns intervals for QPSK and PM-QPSK signals has been carried out [122]. The results are shown in Fig. 28. We can see that, 50 ns after the switching event, only the QPSK signals can be decoded. For PM-QPSK signals, 160 ns delay is required after the switching event. This is due to the convergence time required by the constant modulus algorithm used for polarization demultiplexing. It must be stressed that this delay of 50 and 160 ns, required for QPSK and PMQPSK wavelength converted signals, is not due to the SOA or the FWM process. FWM process is instantaneous, in principle, and the nonlinear SOA used in this work has a fast gain recovery time of 25 ps (data sheet specification).

Figure 28

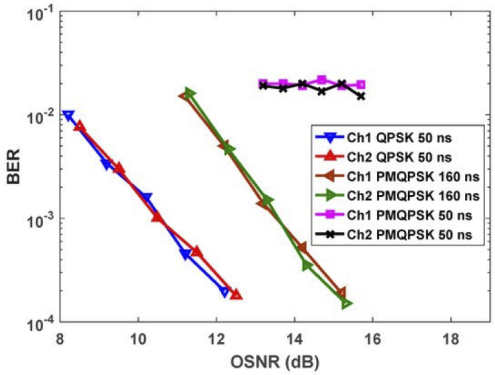

BER as a function of OSNR for the QPSK signal 50 ns after the switching event and for the PM-QPSK signal 160 ns after the switching event. Reprinted from [122] under a Creative Commons license.

4.4. Practicality of Implementing Wavelength Conversion in a Network

All-optical wavelength conversion aims at dynamic allocation of wavelengths by wavelength switching in optical nodes. This has become a necessity for the network operators, because they need to enhance the already-deployed networks to satisfy the increase in users and bandwidths [123]. Various nonlinear mechanisms been studied to realize all-optical wavelength conversion [88]. FWM-based wavelength converters have attracted the most attention. The main advantage of FWM is its flexibility to convert the wavelength continuously to any wavelength within the conversion range of the SOA, while maintaining transparency to both modulation format and bit rate [124].

FWM has been studied in a wide range of media including fibers, silicon, and other semiconductors [88]. The passive devices generally have lower conversion efficiency and require large power levels at the pump and signal wavelengths [125]. However, active media such as SOAs require relatively low input pump and signal powers [101]. The OSNR degradation is not a concern as it has been shown [107] that an output OSNR of 30 dB or more is possible for the wavelength-converted signal. If multiple wavelength converters are employed along a network path, OSNR degradation will be dominated by the first stage, and this issue will not create a bottleneck. Polarization sensitivity is also a challenge for such wavelength converters, and it has been shown that a single SOA can be used for polarization-insensitive wavelength conversion using FWM [126]. The issue of phase-noise increase associated with the FWM process can be resolved with the use of correlated pumps, such as from a comb source, so integrated comb sources can be used for generating pumps for FWM-based wavelength conversion. Wide-bandwidth wavelength conversion is also possible using SOAs and a 100 nm wide wavelength conversion using such an SOA was demonstrated with an average OSNR of 30 dB for the converted signal in Ref. [127].

As switching and routing contributes to more than 30% of total power consumption in a communication network, it is important to analyze the energy consumption of all-wavelength conversion to understand its scalability and practicality. Georgakilas and Tzanakaki [128] investigated the energy consumption of wavelength converters in three different scenarios, namely (a) unprotected, (b) shared backup path protection, and (c) dedicated path protection, based on the provisioning of the optical network for handling link outage. In all the cases, power consumption of all-optical wavelength converters was found to be better than that based on conversion to the electrical domain. It should

be noted that the analysis in this paper was carried out for intensity modulation. However, standard OEO wavelength conversion systems will need complete coherent receivers and associated DSP; thus integration of the all-optical wavelength conversion technology is anticipated to provide a lower power consumption solution.

5. SOA FOR PHASE MANIPULATION

In coherent optical communication systems, various impairments are compensated using DSP, where the trade-off between latency and efficiency of a DSP algorithm needs to be considered carefully. In the case of long fiber links, the overhead in DSP is the highest for chromatic dispersion compensation [129]. Nonlinear impairments in the fiber are typically avoided by controlling the optical power launched into the fiber. Even though advanced machine-learning algorithms have been used in recent years for nonlinearity compensation [130], the corresponding signal processing overheads are typically large. In this context, all-optical techniques, especially OPC implemented with mid-span spectral inversion (MSSI), have proved to be effective in compensating for the impairments induced by both the dispersion and nonlinearity of optical fibers [131–134]. Most OPC demonstrations have used FWM in highly nonlinear fibers (HNLFs) or periodically poled lithium niobate, both of which require power levels, typically larger than 100 mW. On the other hand, SOAs have proved to be an efficient and compact platform that requires much smaller optical power levels to invoke nonlinearities. Thus, exploring the use of SOAs for OPC may prove advantageous for optical communication systems.

An important application of FWM is its tailored use for phase-sensitive amplification and phase quantization. Phase regeneration and amplitude regeneration are two important functions in the field of optical communications. Amplitude regeneration of intensity-modulated data using all-optical processing has been reported in the past [135–137]. The advent of coherent optical communication demands the use of such optical processing toward phase regeneration. The squeezing function of phase-sensitive amplifiers (PSAs) enables phase regeneration, where the signal and noise are amplified in the quadrature that carries information, while being attenuated in the conjugate quadrature [138,139].

In addition to optical communication, PSAs have a wide range of applications in large-scale Ising spin networks [140], phase measurement with enhanced sensitivity [141], and in quantum metrology [142]. FWM in a HNLF is usually employed for realizing PSA [143]. However, practical implementation of fiber-based schemes is limited by the high-pump-power requirement and its relatively large footprint. A smaller footprint occurs for waveguide-based nonlinear media such as periodically poled lithium niobate [144,145] and silicon germanium [146]. However, all these nonlinear media demand high pump powers to demonstrate the phase quantization. Thus, considering the use of SOAs for phase quantization process is highly desirable.

An SOA for OPC was considered as early as 1996 for amplitude-modulated signals [147]. Dynamic optimization of the pump and signal power levels and conversion efficiency with minimal distortions were discussed in that work. For polarization-insensitive OPC, SOAs have been used with orthogonal pumps in Ref. [148]. It is only recently that SOAs have been used for this purpose for applications in coherent communication systems [149–151].

5.1. Signal Fidelity in OPC using SOAs

5.1a. OSNR Retention in an OPC Stage

The gain provided by an SOA is nonparametric in nature. It is generally believed that spontaneous noise added by an SOA makes it unsuitable for nonlinear optical signal

Figure 29

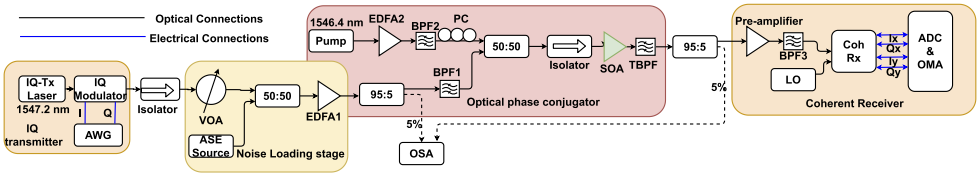

Experimental setup used to study noise transfer during the OPC process inside an SOA.

processing. In Ref. [150], the noise performance of a nonlinear SOA was evaluated in the context of OPC. In most previous works, performance of the generated conjugate wave was evaluated by noise-loading the filtered conjugate and measuring the BER as a function of the loaded OSNR. These measurements assume a transmitter-class OSNR (>25 dB) at the input of the nonlinear medium and do not take into account the noise transfer that could potentially occur due to the OPC process in SOA at various *input* OSNR levels. As the PSA stage, or the OPC stage, is typically envisaged to be placed mid-span, it is critical to evaluate the noise transfer as a function of input signal's OSNR.

Such an experimental study has recently been carried out [150]. OSNR of both the signal and the conjugate waves at the output of the SOA was measured for different *input signal OSNRs* for a CW and a 21-Gbaud QPSK signal. Figure 29 shows the schematic of the experimental setup used to evaluate the OSNR at the input and output of the SOA. The SOA used in this experiment (Kamelian-NL-SOA) had a short carrier lifetime (τ_s = 25 ps). The pump beam with a linewidth (frequency f_p, Δf_p = 100 KHz) was amplified by an EDFA and filtered using a bandpass filter (bandwidth 0.1 nm). The signal from a tunable laser (frequency f_s, linewidth Δf_s = 40 kHz) was fed to an optical IQ modulator to generate QPSK data at 21 Gbaud. This modulated signal is noise-loaded and combined with the pump using a 3-dB coupler before being fed to the nonlinear SOA. The average power of the pump and the signal at the SOA's input was maintained at 0 and −8 dBm, respectively. The signal's frequency had a frequency offset of ±125 GHz with respect to the pump in order to measure the gain and the conjugate conversion efficiency. The output signal and conjugate waves are filtered independently using a wave-shaper (Finisar WSS-1000s) and fed to a phase and polarization-diversity coherent receiver. The detected signals (both I and Q) were digitized using an analog-to-digital converter (ADC, 80 GS/s) and this data is further processed using the standard DSP algorithms to obtain the BER for different input OSNRs. The conjugate of the modulated signal is generated with a conversion efficiency of around 0 dB, while the signal experiences a gain of around 10 dB at a detuning of 100 GHz [150]. The OSNRs of the output signal and the conjugate are shown in Fig. 30 for different input OSNRs (measured with reference bandwidth of 0.1 nm). For the power levels and the input OSNR (< 26 dB) used in this experiment, the OSNR degradation for a reference resolution bandwidth of 0.1 nm, due to the SOA noise was negligible.

The influence of signal distortion through SOA propagation and phase conjugation is quantified in Fig. 30(b) for the conjugate wave by analyzing the BER performance as a function of input OSNR, and comparing with back-to-back curve for QPSK data modulated at 21 Gbaud. The performance of the output signal is identical to that of the back-to-back configuration, thus proving that no significant noise is added by the SOA even with a gain of >10 dB. The generated conjugate has a penalty of ≈1 dB for all OSNR values. The nonlinear phase distortion occurring in all SOAs is an important

Figure 30

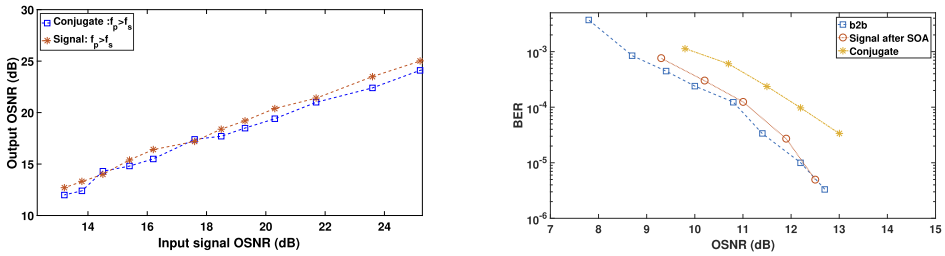

(a) (b)

(a) Output OSNR of the signal and the conjugate waves as a function of input OSNR for a 21-Gbaud QPSK signal ($f_p > f_s$). (b) BER versus OSNR for signal before SOA (back-to back), signal after SOA, and the conjugate wave created by the SOA. Reprinted from [150]. © 2019 The Optical Society.

Figure 31

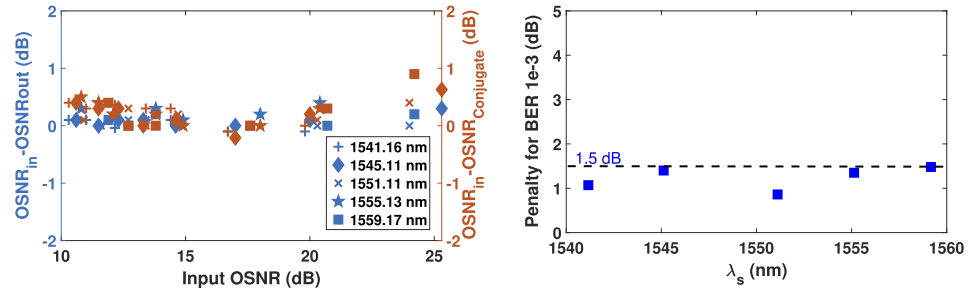

(a) (b)

(a) Difference in the OSNR (ΔOSNR) at the input and output of the SOA (signal, left axis; conjugate, right axis) as a function of input OSNR across the C-band wavelengths. (b) BER performance of the conjugate wave across the C-band wavelengths for a 21-Gbaud QPSK signal.

factor affecting the performance [15]. These results indicate that the signal's distortion caused by the SOA-induced chirp is minimal in the presence of the pump. The pump acts like a holding beam (see Section 3.2.3). The only difference in this case is that the pump's wavelength is close to the signal (detuning is 1 nm).

The performance of the SOA was evaluated across the entire C-band by changing the wavelength of a 21-Gbaud QPSK signal. The results are shown in Fig. 31(a). The pump–signal detuning was fixed at 125 GHz (1 nm), whereas the signal and pump frequencies were varied. It is evident that the noise-retention property of the OPC process holds across the entire C-band for the input OSNR considered. Difference in the OSNR (ΔOSNR) at the input and output of the SOA is <1 dB for both the signal and conjugate waves. The power penalty was also measured and the results are shown in Fig. 31(b). The penalty was <1.5 dB at the BER of 1×10^{-3} across the entire C-band. Clearly, SOAs can be used reliably for optical signal processing based on OPC.

5.1b. Polarization Sensitivity in OPC

Polarization sensitivity of the FWM process is one of the primary challenges in the OPC implementation. In an optical network employing polarization multiplexing, a polarization-insensitive FWM scheme is required for practical implementation of OPC. In one approach, two orthogonally polarized pumps are employed to realize polarization-insensitive OPC [151]. The mechanism that produces this result is known

Figure 32

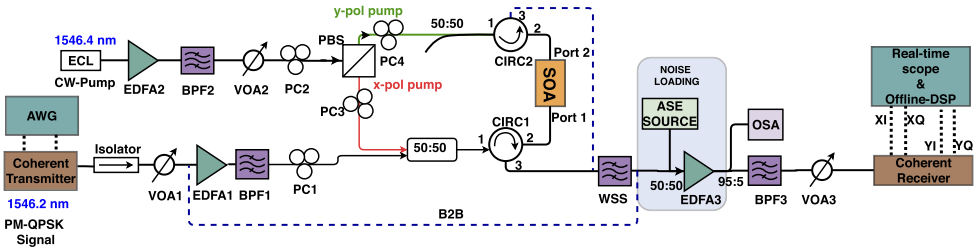

Experimental setup for OPC of a PM-QPSK signal using orthogonally polarized counterpropagating pumps. © 2019 IEEE. Reprinted, with permission, from Sobhanan *et al.*, IEEE Photon. Technol. Lett. **31**, 919 (2019) [152].

as Bragg scattering, and its polarization transformation properties have been discussed in Ref. [151]. Polarization-insensitive OPC of a 10-Gbaud PM-QPSK signal has also been demonstrated using an SOA [152].

Bragg scattering occurs when one pump is scattered by a dynamic grating, formed as a result of the beating between the signal and the other pump. This process enables the generation of the conjugate waves at both the ports of an SOA. Unlike the conventional FWM, it is critical to consider the phase-matching conditions to determine the processes that are involved in the OPC process. This in turn sets the polarization properties in Bragg scattering-based FWM [152]. Figure 32 shows the schematic of an experimental setup used for this purpose [152]. The pump was a narrow-linewidth (100 kHz) ECL at 1546.4 nm. It was is split into two orthogonal polarized parts using a polarization beam splitter (PBS), which were counter-propagated through a nonlinear SOA. At a drive forward current of 375 mA, polarization dependence of the gain was <0.5 dB, and the gain-recovery time was 25 ps.

The center wavelength of the signal laser (λ_s = 1546.2 nm) differed from that of the pump by 25 GHz. The signal was modulated with the PM-QPSK format and coupled with its polarization oriented arbitrarily with respect to one of the pumps (X-polarization in the experiment). Both pump and signal were fed to the SOA through the input port of the SOA. The other pump (Y-polarized) was launched into the SOA through the output port. The power levels of both pumps were around 1 dBm, whereas the signal power was maintained at −8 dBm. The phase-conjugate wave ($\omega_c = 2\omega_p - \omega_s$) at 1546.6 nm was extracted from both the input and output ports of the SOA using circulators and filtered through a bandwidth-programmable optical filter (Finisar WSS-1000S). Controlled amounts of ASE noise was added to the filtered conjugate to change its OSNR. The output was fed to a polarization and phase-diversity coherent receiver. The electrical analog signal corresponding to the in-phase (I) and quadrature (Q) components in each polarization were digitized using high-speed ADCs. The digital samples were equalized for various impairments using off-line DSP.

It was found that the conjugate wave had a conversion efficiency of about −3 dB at port 2. In contrast, the efficiency was ≈ −7 dB at port 1 because the conjugate wave was produced only through Bragg scattering. Our estimate of conversion efficiency is based on the total power in both polarizations; differences in the power levels for *X* and *Y* polarizations become important for evaluating the BER performance. The measured BER for the two conjugate waves is shown in Fig. 33, for both *X* and *Y* polarizations, at the input (a) and output (b) ports for a 10 Gbaud PM-QPSK signal. The back-to-back performance of the signal is also shown in these figures for comparison. It can be seen that the BER performance of both conjugate waves is nearly identical, with only a negligible difference at the two ports of the SOA. This result can be attributed to the

Figure 33

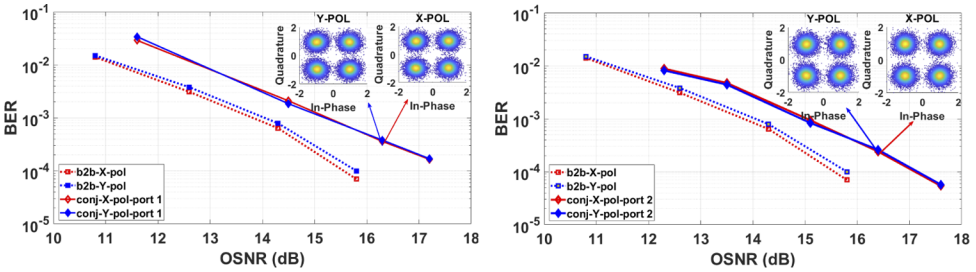

BER as a function of OSNR for the X- and Y-polarized conjugate waves, measured at (a) input and (b) output ports for a 10 Gbaud PM-QPSK signal. The back-to-back case is also shown for comparison. © 2019 IEEE. Reprinted, with permission, from Sobhanan *et al.*, IEEE Photon. Technol. Lett. **31**, 919 (2019) [152].

Figure 34

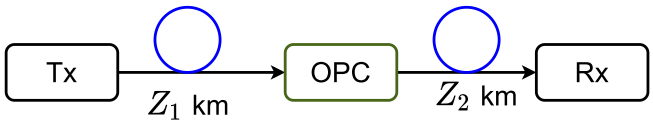

Schematic of the MSSI.

polarization-insensitive nature of OPC in this experiment. When compared with the back-to-back case, the OSNR penalty is <1.5 dB in all cases. This penalty is due to phase distortions resulting from the phase-noise transfer in a partially degenerate FWM scheme, which are especially severe at low baud rates and from the nonlinear phase noise in SOA. We should stress that the OPC process is expected to be independent of the modulation format. Conjugate generation at larger baud rates can be realized with a larger pump–signal detuning, albeit with lower conversion efficiencies. In Ref. [152], the authors also discussed unitary polarization transformation of the Bragg scattering and stressed the polarization-insensitive nature of the OPC process.

5.2. Simultaneous Compensation of Dispersive and Nonlinear Distortions

As we discussed earlier in this section, the OSNR of an incoming signal is nearly preserved at the output end of an SOA used for OPC. Moreover, OSNR of the conjugate wave is nearly the same as that of the signal. We also found that chirp-free amplification of the signal occurs in the presence of a saturating pump. Here we discuss how OPC by an SOA can be used for simultaneous compensation of distortions induced by the combination of dispersion and nonlinearity inside optical fibers [153]. Figure 34 shows a schematic of the MSSI scheme.

Let Z_1 and Z_2 be the lengths of the transmission fibers before and after the OPC stage, respectively. Following the OPC analysis of Ref. [153], the propagation of a telecom signal through an optical fiber is governed by the following nonlinear Schrödinger equation (NLSE):

$$\frac{\partial E(z,t)}{\partial z}+\frac{j}{2}\beta_2\frac{\partial^2 E(z,t)}{\partial t^2}-j\gamma_1|E(z,t)|^2E(z,t)+\frac{\alpha}{2}E(z,t)=0, \tag{74}$$

where α, β_2, and γ are the fiber attenuation, second-order dispersion, and nonlinear parameters, respectively. This equation can be used to study the evolution of the complex envelope $E(z,t)$ of the signal through the first span of the fiber. The conjugate

of the signal (E^*) generated through OPC requires the use of the following modified NLSE for its propagation through the second span of the fiber:

$$\frac{\partial E^*(z,t)}{\partial z} - \frac{j}{2}\beta_2 \frac{\partial^2 E^*(z,t)}{\partial t^2} + j\gamma_2 |E^*(z,t)|^2 E^*(z,t) + \frac{\alpha}{2} E^*(z,t) = 0. \tag{75}$$

Note that the signs of both the second and third terms in Eq. 74 are inverted for the propagation of the conjugate wave.

In general, β_2 may vary with distance because of dispersion management. However, if the accumulated dispersion is the same in both sections, i.e., $\int_0^{Z_1} \beta_2(z)\, dz = \int_0^{Z_2} \beta_2(z)\, dz$, all dispersive effects can be compensated by the OPC. However, the nonlinear impairments depend on the local optical power of the signal that varies because of losses. As a result, the degree to which the nonlinear effect can be compensated depends on the design of the transmission link. From Eqs. (74) and (75), a general condition for perfect compensation of the Kerr effect can be written as [154]

$$\frac{1}{\gamma_1 P_1} \int_0^{Z_1} \beta_2(z)\, dz = \frac{1}{\gamma_2 P_2} \int_0^{Z_2} \beta_2(z)\, dz, \tag{76}$$

where the subscripts 1 and 2 stand for the two spans, respectively. When β_2 and γ are constants and have the same values in two spans, the dispersive and nonlinear phases accumulated in the first span can be compensated when the conjugate is transmitted through an equal length of the second span of fiber, assuming Eq. 76 is satisfied [153].

Let us assume OPC is performed using partially degenerate FWM inside an SOA. Consider a signal at the frequency ω_s with the linewidth $\triangle\nu_s$ and a pump at the frequency ω_p with the linewidth $\triangle\nu_p$. When both are injected into the SOA, the conjugate at the frequency $2\omega_p - \omega_s$ is generated with a linewidth of $4\triangle\nu_p + \triangle\nu_s$ [104]. In addition, the SOA is expected to introduce nonlinear phase distortions, depending on the bias current and the input power levels. Thus, an SOA is expected to introduce some penalty with respect to the back-to-back situation owing to the inherent phase distortions and the phase-noise transfer during the OPC process similar to what we have seen in the previous section. SOAs may still be preferred because of their compact size and relatively smaller power levels required for the pump, provided the performance penalty associated with their use is not too large.

5.2a. Amplitude- and Phase-Modulated Signals

In a 1988 demonstration of MSSI [155], 2-ps optical pulses were sent over 40 km of standard fiber by employing an SOA in the middle of the span. It was found that the second-order dispersive effects governed by β_2 were completely compensated. At the same time, distortions and the excess chirp generated within the SOA were negligible even for 2-ps pulses. It was this experiment that suggested that SOAs can be used for OPC in high-data-rate applications. Indeed, an implementation of this technique for a 40-Gb/s amplitude-modulated system showed that both dispersive and nonlinear distortions could be compensated over distances of up to 406 km [156,157].

Several experiments employed SOA-based OPC for phase-modulated signals [158,159]. A 40-Gb/s RZ-DPSK signal was successfully transmitted over 100 km with a penalty of less than 2.5 dB with respect to back-to-back configuration [158]. In another experiment, this technique was used to demonstrate the transmission of a 107-Gb/s RZ-QPSK signal over 108 km of standard fiber with a BER smaller than the FEC limit [159]. More recent work has used the OPC technique for advanced modulation formats. We discuss this work next in the context of m-QAM signals.

Figure 35

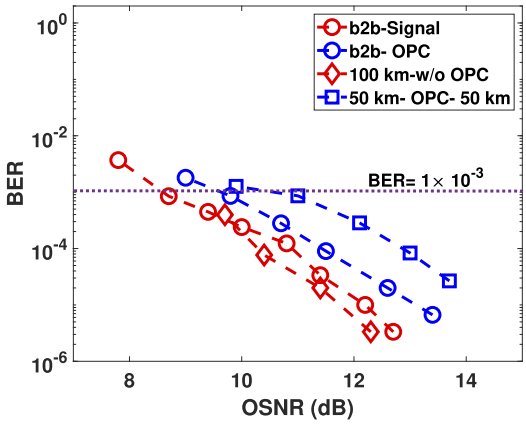

BER in four cases plotted as a function of OSNR for a 40-Gb/s QPSK signal. Back-to-back performance is shown with the curves marked b2b. Reprinted from [160] under a Creative Commons license.

5.2b. mQAM Signals

In a 2020 experiment, SOA-based OPC was used to transmit 21-Gbaud QPSK signal over 100 km of standard fiber [160]. A narrow-linewidth laser at wavelength 1551.11 nm was used with an IQ modulator to generate the QPSK signal at 21 Gbaud. The modulated signal was transmitted in the first 50-km span using EDFAs such that the signal power launched into the OPC stage was −8 dBm. The pump laser at wavelength 1550.11 nm (pump–signal detuning 125 GHz) had 1 mW power that was enough to saturate the SOA and initiate the FWM process needed for OPC. The conjugate wave was filtered, amplified, and fed to the second 50-km span of standard fiber. The OSNR of the signal/conjugate was controlled by introducing ASE noise from an EDFA at the coherent receiver. The received signal was digitized and is processed using off-line DSP. Both the signal and the pump wavelength were swept over the C-band, while maintaining the detuning of 125 GHz between them. Figure 35 shows the BER performance as a function of OSNR under four operating conditions [160]. The "b2b-signal" curve represents the back-to-back case, without any OPC or fiber link and is used as a reference to calculate the OSNR penalty. The "b2b-OPC" curve corresponds to the conjugated idler (without any fiber). The BER is estimated with respect to the conjugate data in this case. It shows a penalty of about 1 dB compared with the back-to-back case because of nonlinear phase distortions inside the SOA used for OPC. The performance of the system after 100-km fiber, but without the OPC module, is also shown. DSP in this case included dispersion compensation through frequency-domain equalization [129]. For this reason, BER results were identical to the back-to-back case. The BER curve with rectangles shows the results when an OPC stage was used mid-span with a 1-mW pump power and a conversion efficiency of −3 dB. The off-line DSP in this case did not include dispersion compensation. It is seen that the power penalty is less than 1.5 dB (at the FEC limit) compared with the "b2b-OPC" case [160]. The origin of this penalty may be nonlinear chirp accumulated within the SOA. Compared with the back-to-back case, the total penalty is about 2.5 dB. It may be possible to reduce it further with optimization of the signal and pump powers launched into the SOA.

To observe the effect of input signal power, it was increased in steps of 2 dBm, and the performance of the system with signal modulated in 16-QAM modulation format was evaluated with and without OPC. Care was taken to ensure that launched power was the same in each span, and the pump power was maintained at 0 dBm in all cases.

The error vector magnitude (EVM) is calculated as a function of the signal power, and the result are shown in Fig. 36(a). The EVM is larger for an OPC-based system at low powers owing to (i) phase-noise transfer from the pump and (ii) nonlinear chirp inside the SOA. Penalty at the smallest launch power can also be attributed to a lower conversion efficiency and a lower output OSNR of the conjugate wave, even though the input signal to SOA is maintained at −8 dBm. The initial drop in EVM with increasing power is due to a corresponding increase in the OSNR at the input end. As the input power increases beyond a certain value, nonlinear distortions increase the EVM, as seen in Fig. 36(a). However, the power level at which EVM starts to degrade is larger in the presence of OPC. Indeed, the OPC-based system performs better at high power levels, a feature indicating the nonlinear tolerance of such a system.

Without OPC, EVM penalty becomes too large at power levels larger than 8 dBm due to the large nonlinear phase distortions from the fiber distorting the data of the 16-QAM signal. In contrast, data could be retrieved successfully (BER below FEC limit) even at a launch power of 12 dBm when OPC was used. The reason is that most of the nonlinear effects accumulated in the first fiber span were compensated in the second span because of OPC. Referring to Fig. 36 and taking 10% EVM as being acceptable, the power margin of OPC is about 2 dB. This margin would increase for longer lengths (say 500 km each section) because nonlinear distortions increase with length.

The performance advantage of the SOA-based OPC across the entire C-band is shown in Fig. 36(b), where the EVM is evaluated for 16-QAM signals for the 100-km link, using launch power per span of 10 dBm. The EVM is around 10% throughout the C-band with a ±1% variance. However, such a system at any wavelength will operate successfully because the BER is below the FEC limit at all the points in Fig. 36(b). These results indicate that the use of SOA-based OPC is beneficial for WDM systems making use of the entire C-band [160].

5.2c. Coherent Orthogonal Frequency-Division Multiplexed Signals

SOA-based OPC is also useful for coherent OFDM systems. Its effectiveness for distortion compensation in such systems was demonstrated in Ref. [161] using a 16-QAM coherent orthogonal frequency-division multiplexing (CO-OFDM) signal. Coherent OFDM signals pose a much bigger challenge to the use of SOAs because

Figure 36

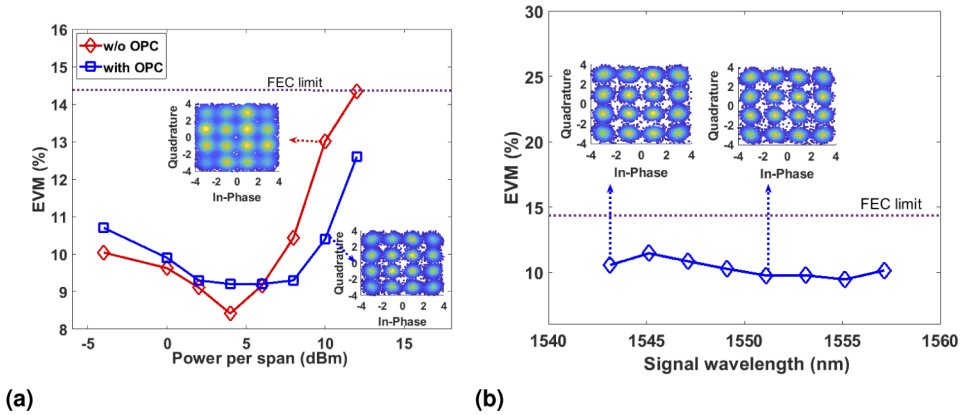

(a) EVM for a 16-QAM signal as a function of input power to each 50-km fiber span with and without OPC. (b) EVM over the C-band when OPC is used with a per-span launch power of 10 dBm. Reprinted from [160] under a Creative Commons license.

Figure 37

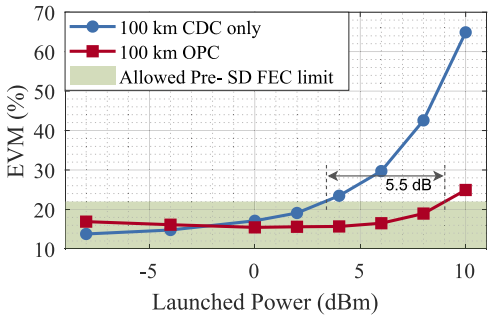

EVM performance of a 80-Gb/s 16-QAM CO-OFDM system with and without SOA-based OPC. CDC stands for chromatic-dispersion compensation. The shaded region shows the acceptable FEC limit. Reprinted from [161] under a Creative Commons license.

their relatively larger peak-to-average power ratio (PAPR) is expected to induce larger gain fluctuations, resulting in more nonlinear phase noise. In practice, distortions resulting from fiber's nonlinearity as well as SOA's nonlinearity affect a CO-OFDM system when an SOA is used for MSSI, especially in the case of few-hop fiber links.

As an example, Fig. 37 compares the EVM performance of a 80-Gb/s 16-QAM CO-OFDM system as a function of launched power, with and without OPC. In this experiment, the OFDM signal was produced using 16-QAM symbols with 72 subcarriers (along with a guard band and eight pilot subcarriers), and it spanned a total frequency spread of 20 GHz. This frequency-domain signal is converted to the time domain through a 128-point inverse FFT operation. This digital electric signal was used to drive a coherent transmitter and to generate a 80-Gb/s, 16-QAM, CO-OFDM signal at the 1551.11 nm wavelength (with a 25-kHz linewidth). Power levels used were identical to those used for the single-carrier experiment [160]. DSP algorithms included (correlation-based) time and (blind) frequency synchronization, training-symbol-based channel estimation/equalization, and pilot-assisted phase-noise correction [162].

The curve with circles in Fig. 37 shows the EVM as a function of launched power when no OPC was employed but dispersion was compensated at the receiver. The curve with squares show the improvement realized when OPC was used mid-span to compensate for nonlinear distortions. As one may expect, the magnitude of the error vector is much smaller in the OPC case, especially at high-power levels. With the use of OPC, the power at which the EVM starts to degrade beyond the FEC limit is about 9 dBm, which is larger by 5.5 dB compared with the case without OPC, thereby indicating the improved nonlinear tolerance of the OPC system. The relatively poorer performance of the OPC case at smaller launched powers (<-3 dBm) is attributed to the lower OSNR of the input signal.

5.3. Regeneration and Quantization of Optical Phase

The advent of coherent systems requires devices capable of regenerating or quantization of the phase of an optical signal. Such devices are typically based on a FWM-based PSA, built typically utilizing FWM in nonlinear media. The general schematic of a parametric amplifier is shown in Fig. 38.

When the pump and signal wave mix in a nonlinear media, it creates a dynamic grating. Considering the phase modulation of the pump due to this grating, sidebands are generated at frequencies $\omega_p - (\omega_p - \omega_s)$ and $\omega_p + (\omega_p - \omega_s)$. Power is thus transferred

Figure 38

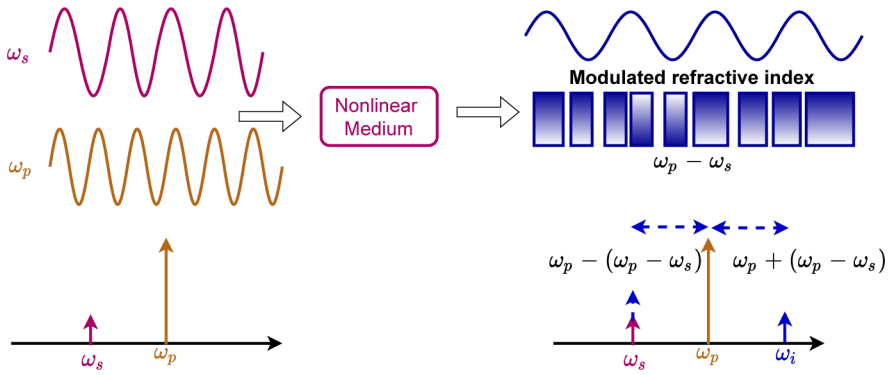

General schematic of a parametric amplifier.

from the pump (at ω_p) to the signal (at ω_s) and to the idler (at ω_i) simultaneously. Thus, when the incoming signal is allowed to mix with strong pump(s), in addition to the generation of conjugate idlers, the signal also experiences amplification. The gain experienced by the signal in this case is referred to as the parametric gain, and this process is utilized to realize parametric amplifiers. Wide-band and high-gain fiber optic parametric amplifiers have been demonstrated in the past with HNLFs [163–165]. If the idler is seeded at the input of the parametric amplifier, it results in a coherent mixing of signal and idler, giving rise to a phase-sensitive operation. The gain experienced by the signal in this case is a function of its input phase and this property of PSAs is used for phase regeneration. In case of binary PSK (BPSK) signals, the signal is symmetrically placed between two pumps and the idler generated at the signal frequency, coherently mixes with the signal, resulting in two-level phase quantization [166]. Four level quantization occurs when the signal (with phase ϕ_s) adds coherently with its conjugated third harmonic (with phase $-3\phi_s$); both generated at the same frequency, resulting in a phase addition corresponding to $e^{i\phi_s} + r.e^{-i3\phi_s}$, where r is the ratio of the corresponding power levels. Phase-sensitive amplification thus requires efficient nonlinear media.

PSAs have been demonstrated in nonlinear media such as optical fibers, periodically poled lithium niobate, photonic crystal fibers, or chalcogenide waveguides [143] in the past. However, the pump power required for achieving PSA in these nonlinear media is relatively high. The use of SOAs for such a device requires not only much smaller powers (<10 mW) but also has the advantage that it can be integrated within a chip containing a photonic integrated circuit. SOAs have been used for realizing a PSA in several studies [167–169]. In this section, we discuss the details of the some experiments that have demonstrated phase regeneration and phase quantization using SOAs.

5.3a. SOA-Based Phase Regeneration

The pumps, signal, and idler waves must be phase-correlated for phase regeneration. Establishing this phase correlation has been challenging in the practical implementation of phase-sensitive amplification. A common approach is to generate the idler through a FWM process at a "copier stage" and transmit it along with the signal. To avoid transmission of high-power pumps through the transmission fiber, the pumps are typically generated locally at the PSA through an injection-locking process [143]. Thus, efficient and controllable FWM is required at both the copier and the PSA stage. Here we discuss a few demonstrations where SOAs were used at both the copier and PSA stages.

Figure 39

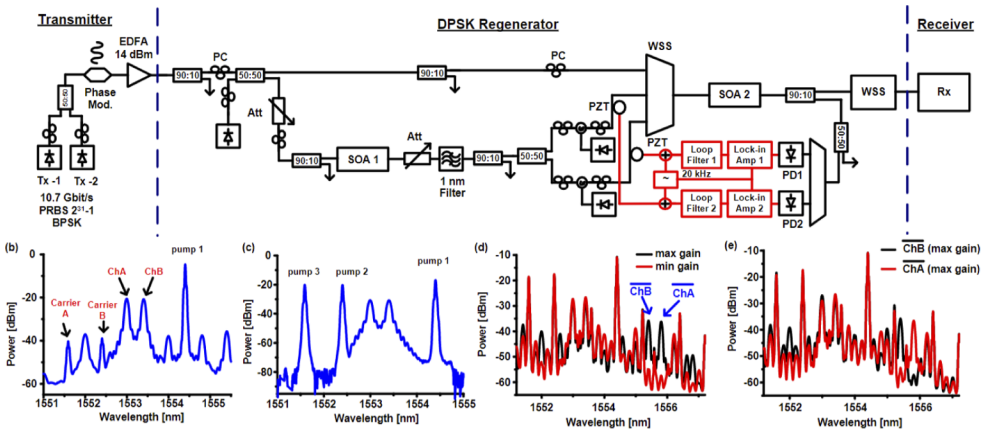

(a) Experimental setup used for DPSK regeneration. (b) Optical spectrum after the carrier extraction stage at the output of SOA-1. (c) Optical spectrum at the output of the WSS. (d) Optical spectrum at the output of SOA-2 when both channels are locked either at the maximum or minimum gain stateof the PSA. (e) Optical spectrum at the output of the SOA-2 when the channels are locked at different phase sensitive gain states of the PSA. © 2012 IEEE. Reprinted, with permission, from Sygletos *et al.*, European Conference on Optical Communication, paper Tu.1.A.2 (2012) [170].

Phase regeneration of a two-channel DPSK signal was demonstrated as early as 2012 using SOAs [170]. The schematic of this experiment is shown in Fig. 39. The signal was allowed to experience FWM with a pump laser in SOA-1 to extract the phase-correlated pumps for the PSA stage; the corresponding output spectrum is shown in Fig. 39(b). Note that the pump power required for this process was less than 4 mW, which is significantly smaller than the power levels required ($\approx$1 W) for the corresponding implementation in a HNLF by the same authors [171]. Two slave lasers were injection-locked, where the extracted pumps from SOA-1 acted as the master to strip off any residual signal modulation. The cleaned-up pumps were then combined with the signal in a wave-shaper, whose output spectrum is shown in Fig. 39(c). Another benefit of using an SOA as a copier is that the path difference between the signal arm and the copier arm is reduced significantly, thus minimizing the effects of environmentally induced phase fluctuations between the signal and the pumps.

The signal experiences phase-sensitive amplification at the PSA stage, which is in another SOA (SOA2). As the modulation format in this case is DPSK, the idler generated at the signal wavelength for each channel coherently mixes with the signal, resulting in two-level quantization/regeneration. Figure 40 shows the BER as a function of received power and the corresponding eye diagrams observed at the output of the PSA stage. Note that the two-level quantization requires the signal and idler to mix with equal proportions for maximum phase squeezing. As the SOA also offers nonparametric gain, the PSA process resulted in a nonoptimal phase squeezing for the degenerate mixing of the signal and the idler in this experiment. However, significant phase squeezing was observed at the nondegenerate idler (indicated as λ-converted channels). Figure 40 shows the BER performance of the DPSK signals with a sensitivity improvement of more than 4.5 dB. This brings us to an important issue when SOAs are used for optimization, the optimization of the mixing ratios of the signal and idler: this issue is discussed in the next section.

Four-level quantization was implemented with SOAs for the first time in Ref. [169]. Figure 41 shows the spectra measured in this experiment at the input and output of the

Figure 40

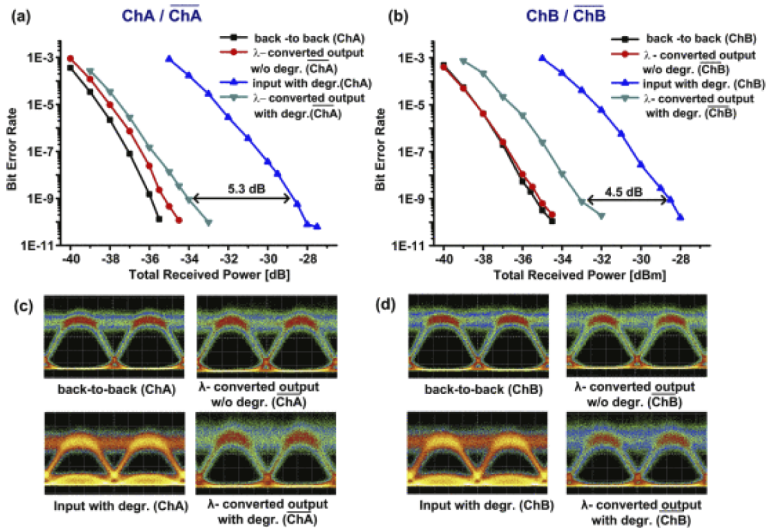

BER versus total received power: (a) for ChA and its wavelength-converted channel; (b) for ChB and its wavelength-converted channel at the input/output of PSA with and without the presence of input periodic degradation. (c) Corresponding eye diagrams for the four channels. © 2012 IEEE. Reprinted, with permission, from Sygletos *et al.*, European Conference on Optical Communication, paper Tu.1.A.2 (2012) [170].

Figure 41

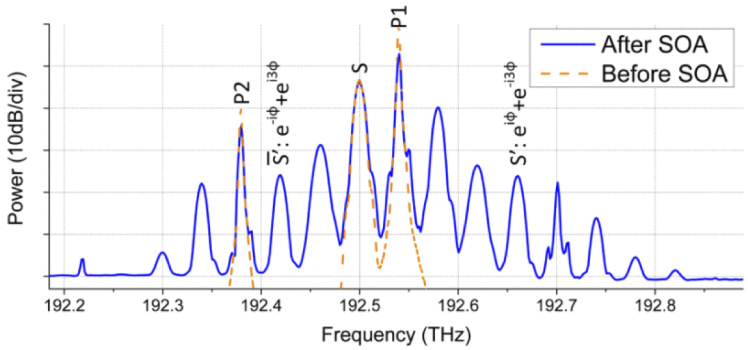

Example of spectra before (dashed orange line) and after (solid blue line) FWM in SOA. © 2016 IEEE. Reprinted, with permission, from Bottrill *et al.*, IEEE Photon. Technol. Lett. **28**, 205 (2016) [169].

PSA stage. It is evident that there are two possibilities for the generation of quantized output: a conjugated output from the mixing of the conjugated signal and its third harmonic ($e^{-i\phi_s} + r.e^{3i\phi_s}$) and an nonconjugated output from the mixing of signal and conjugate of its third harmonic ($e^{i\phi_s} + r.e^{-3i\phi_s}$), labeled as $\bar{S}'$ and S', respectively, in the figure. The highly efficient FWM processes in the SOA enabled this demonstration without a copier stage. The schematic of the experimental setup used for four-level quantization is shown in Fig. 42. Phase correlations were established by deriving the signal and the pumps from the same laser source, to minimize additional complexities. A phase modulator was used in the signal arm to introduce phase errors while phase correlated pumps were derived by over-driving a Mach–Zehnder modulator (MZM) followed by a programmable filter (PF). The fiber stretcher is used to match the phases in the signal and pump arms.

Figure 42

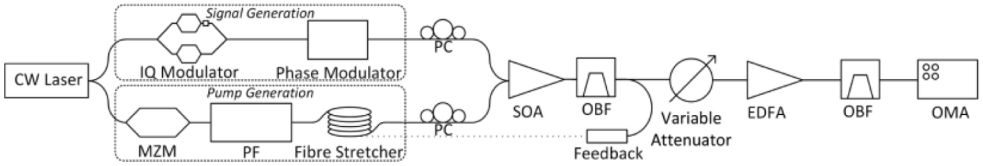

Experimental setup used for four-level phase quantization. © 2016 IEEE. Reprinted, with permission, from Bottrill *et al.*, IEEE Photon. Technol. Lett. **28**, 205 (2016) [169].

Figure 43

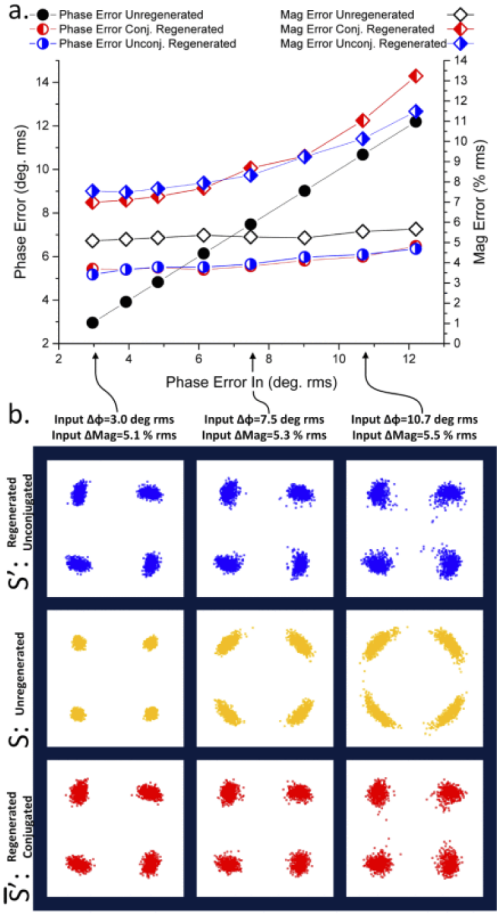

(a) Phase and amplitude noise statistics before and after regeneration for both the conjugated and unconjugated output. (b) Constellation plots for the three input phase-noise levels studied for the unregenerated case, as well as for the conjugated and nonconjugated output. © 2016 IEEE. Reprinted, with permission, from Bottrill *et al.*, IEEE Photon. Technol. Lett. **28**, 205 (2016) [169].

Figure 43 shows the noise statistics of the signal observed in the experiment and it is evident that the output phase noise is very similar between the conjugated or unconjugated output. By comparing the regenerated phase noise curves to the unregenerated phase noise curve, the system shows a reduction in phase noise for all input phase noises exceeding 5.5° rms and for the highest input noise case of 12.2° rms, the system results in a halving of phase noise. The output magnitude noise in all cases can be seen to be worse than the input magnitude noise, worsening as the input phase noise

increases. This phase-noise-dependent increase in magnitude noise is expected from this type of phase squeezer [166] and is the result of phase dependent gain. The large increase in phase noise for low input phase noise levels is due to the ASE induced magnitude noise being converted into phase noise through nonlinear effects (such as SPM and XPM) as well as the ASE itself, which we believe can be improved through the use of a longer SOA. Constellation plots are shown in Fig. 43(b), before and after regeneration, for both the conjugated and unconjugated outputs using three different values of input phase noise. The conjugated and unconjugated results match each other quite well, both showing deterioration of the signal in the case of low phase noise, but showing a clear reduction in phase noise for the higher input noise levels. The increase in phase noise observed for low input phase noises is due to the fact that the poor OSNR of the pumps and corresponding amplitude noise induces a nonlinear phase noise in the signal [118]. It should also be reiterated that, power levels of the coherently mixing signals need to be optimized in order to achieve the maximum phase squeezing and this is indeed a challenge in the case of SOAs because they also provide nonparametric gain. However, this issue can be resolved by quantifying the gain extinction ratio (GER) as a function of input signal power levels, as discussed in the following subsection.

5.3b. Power Optimization for Phase Quantization

The GER is decided by the correct choice of mixing ratios of the signal with the desired idler. Several reports in the past have described the details of optimization of power levels of the mixing beams in HNLF-based PSA [172]. In Ref. [173], an experimental study was conducted with random gain values and it was concluded that the best phase quantization is achieved when the power ratio between the signal and the conjugate are equal in case of two-level quantization. A brute-force optimization of the quantization may be possible by adjusting the power levels at the input of the PSA when the nonlinear medium is passive. However, this may be difficult for an active gain medium such as SOA. SOAs also provide asymmetric gain, hence it would be cumbersome to carry out an optimization by just randomly adjusting the power ratio of the input waves.

In this section, a relation between the signal-to-idler amplitude mixing ratio (r) and the GER, which is a measurable quantity at the output of the SOA, that can be used to achieve optimal M-level phase quantization in general is described as in Ref. [174]. This relation is universal and can be applied irrespective of the nonlinear medium used for the PSA. The numerical results on the influence of GER on M-level quantization with SOA are presented in Ref. [175]. The experimental data that verifies the dependence of GER on the quality of phase quantization in SOA is described in this section [174].

The complex amplitude A_{out} of the coherent combination of signal and the idler for M-level quantization can be written as

$$A_{out} = A_0 \exp(j\phi_s) + rA_0 \exp\left(-j(M-1)\phi_s\right), \tag{77}$$

where A_0 and rA_0 are the amplitudes of the two mixing fields. The quality of this interference output or the quantization depends on the mixing ratio r, which is decided by the conversion efficiency of the mixing process and by the nonparametric gain offered by the SOA. The importance of the choice of r for an M-level quantization was studied in detail in Ref. [176]. The average deviation of the phase quantizer from an ideal step function was quantified in this work through a misfit factor (MF) defined as

$$MF = \log_{10}\left(\frac{M^2}{\pi^2}\int_{-\frac{\pi}{M}}^{\frac{\pi}{M}} |\phi_o(r,\phi_s) - \phi_{step}|\, d\phi_s\right), \tag{78}$$

Figure 44

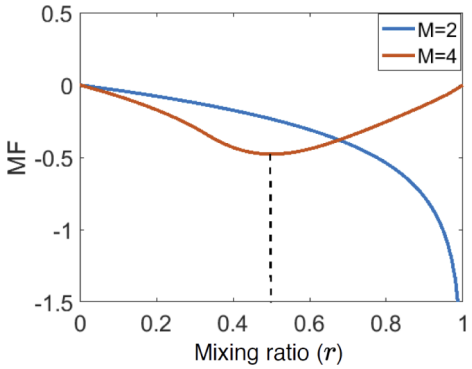

Misfit factor as a function of the mixing ratio r for $M = 2$ and 4.

Figure 45

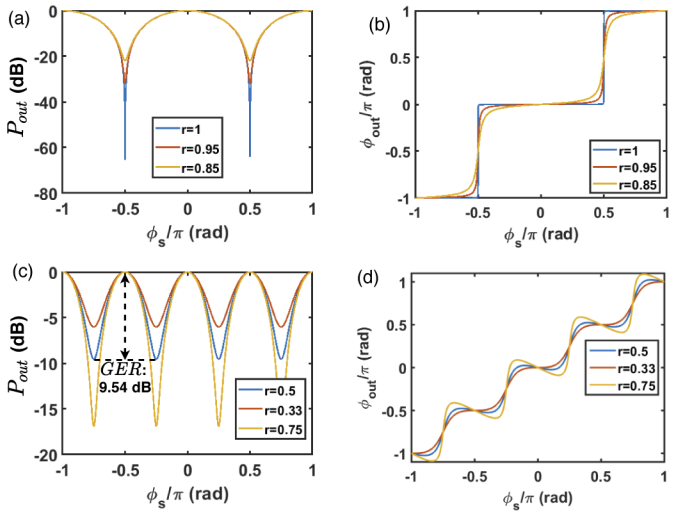

Quantized output as a function of relative input signal phase (a) output power (normalized) and (b) output phase for two-level quantization, (c) output power (normalized) and (d) output phase for four-level quantization, for different r values. Reprinted from [174]. © 2021 The Optical Society.

where ϕ_s is the input phase to be quantized, ϕ_o is the phase of the output field defined in Eq. (77), and ϕ_{step} is the ideal step function.

Figure 44 shows MF as a function of r for $M = 2$ and 4. The misfit factor of an ideally quantized output would tend to $-\infty$. The quantized output as a function of the relative input phase are shown in Fig. 45 for both two- and four-level quantization and for different values of r. For the two-level phase quantization, the value of r that leads to the ideal MF is 1, as seen in Fig. 45, indicating that optimal quantization occurs when the conjugate and the requisite idler mix with equal amplitudes. The optimal mixing ratio progressively decreases with increasing M. For $M = 4$, MF is found to be minimum at $r = 0.5$. As r is not measurable directly in an experiment, especially when the nonlinear medium is an SOA, it can be quantified through the GER, defined as the ratio of the maximum output gain to the minimum output gain as ϕ_s is tuned over its 2π range.

For a process governed by Eq. (77), the output power P_{out} is given by

$$P_{out} = |A_{out}|^2 = A_o^2(1 + r^2 + 2r\cos(M\phi_s)). \tag{79}$$

Figure 46

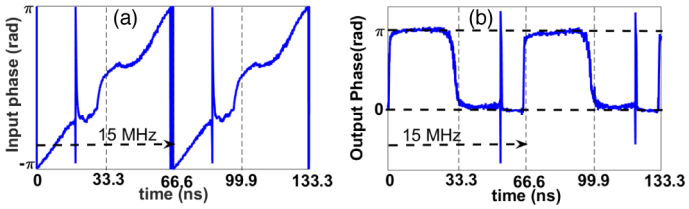

(a) Phase of the input signal to the phase quantizer obtained by driving a phase modulator with a 15 MHz sawtooth input voltage. (b) Two-level phase-quantized output of the PSA stage. Reprinted from [174]. © 2021 The Optical Society.

The GER can be found in an analytic form using the output power and is given by

$$\mathrm{GER} = 10\log_{10}\left(\frac{P_{out,max}}{P_{out,min}}\right) = 10\log_{10}\left(\frac{1+r}{1-r}\right)^2. \tag{80}$$

Thus, there exists a direct relation between r and GER and it can be used to optimize the experimental operating conditions for any M-level quantization scheme. For $M = 2$, MF is minimum at $r = 1$ and, hence, GER should be as large as possible. However, MF is minimum at $r = 0.5$ for $M = 4$, and substituting it in Eq. (80), we find that the optimal GER for best quantization is 9.54 dB. Thus, the GER helps to identify the operating point which would correspond to minimum MF and provide the best possible phase quantization.

In one SOA-based experiment that used the optimized GER, the input pump power (1 mW) was chosen such that it was sufficient to saturate the SOA. The signal-to-idler power ratio (S/I) and the pump-to-idler power ratio (P/I) were chosen such that GER was maximum in the case of two-level quantization [174]. The largest GER was observed for a S/I power ratio of −6 dB, and the corresponding phase quantization results are shown in Fig. 46(a). The phase of the signal was modulated at a frequency of 15 MHz using a sawtooth waveform, and the applied drive voltage was set such that it varied from $-V_\pi$ to $+V_\pi$ (3.5 V_{pp}) at the input port of the modulator. Thus, one cycle of sawtooth waveform modulated the signal's phase linearly over the 2π range. Figures 46(a) and 46(b) show the input and the output of the phase-quantization stage. It is evident that the output is quantized to two fixed phase states with a nonzero mean phase shift (corresponding to the residual ϕ_s). The two quantized phase states are found to have a phase difference of π, as expected for a two-level phase quantizer. The lower quantized value is aligned to 0 rad, and the upper quantized one to π, for a clear visualization, i.e., the output phase plotted is the relative output phase. Phase jumps in both Figs. 46(a) and 46(b) are due to phase wrapping between $-\pi$ and $+\pi$, whenever random phase drifts occur owing to some environmental perturbation or voltage fluctuations in RF source used to drive the modulator. The GER is maximum at an S/I ratio of −6 dB, and almost ideal phase quantization is realized for the optimized power ratio. Other S/I ratios resulted in smaller GER values with a large quantization error. Similar results were found for the four-level quantization at a GER of 9.5 dB [174]. The specific values of the optimized power ratio are specific to the reported experiment and can change under different experimental conditions, but the concept of optimal GER is independent of the experimental conditions.

5.4. Comparison with Other Nonlinear Media

It is now established that FWM is the key process that can enable wavelength conversion, phase conjugation, parametric amplification, and phase-sensitive amplification,

Table 4. Summary of the Different Demonstrations of OPC and PSA-Based Phase Regeneration and Phase Quantization Experiments in Different Nonlinear Media with the Corresponding Pump Power Levels Used

Process	Nonlinear Medium	Pump Power (dBm)	Reference
OPC	HNLF	25	[177]
		30	[178]
		32	[179]
		32	[180]
	PPLN	30.1	[181]
		25.9	[182]
		20.4	[183]
		> 20	[131]
		24.4	[184]
	Si waveguide	26	[46,185]
	Si nanowire	22.4	[186]
	SOA	0	[150–152]
Phase quantization	HNLF	27	[176]
		29	[172]
		>20	[187]
		26	[188]
		33	[166]
		>30	[189]
		29	[190].
Phase regeneration	HNLF	30	[4]
		30	[144].
	PPLN	24.7	[145]
		21	[191]
	SiGe Waveguide	<21	[146]
	SOA	< 6	[192]
		< 7	[170]
		<10	[169]
	PPLN	33	[89]
PSA	a-Si:H waveguide	32 (Peak power-pulsed)	[193]
	Si-Photonic crystal waveguide	31.7 (Peak power-pulsed)	[194]
	AlGaAs	19 to 27	[195]
Phase quantization	**SOA**	**0**	[174]

under the characteristic operating conditions required for each process. Any nonlinear medium capable of yielding FWM can thus be used for the realization of the above functionalities. In order to compare these, Table 4 lists the pump powers used in various experiments for FWM-based OPC process in different nonlinear media. It is clear from this table that SOAs require the least pump power and should be used when energy efficiency is a prerequisite. Table 4 also lists the corresponding comparison for other phase manipulation processes discussed in this section, and it is evident that SOAs stand out in terms of the pump power requirement and, hence, the energy efficiency. Most of the passive nonlinear medium discussed in Table 4 require pump power levels well in excess of 10 mW to initiate nonlinearity, which potentially implies the need for high-power EDFAs to achieve the required pump power levels. When employing SOA nonlinearities to undertake various all-optical processing functions, pump powers of smaller than 10 mW are typically required, however, the SOA being an active medium we also need to consider the power consumed by the SOA drive current for energy efficiency calculations. Thus, while we compare the energy efficiency in general, in the case of SOAs based signal processing applications we need to consider power consumption of pump laser and the SOA, while for other passive media discussed in Table 4, we need to consider power consumption of laser and EDFA in order to reach the required pump power levels. A standard single mode laser diode and SOA, with output power levels around 10 mW, will typically consume a few watts of electrical power for laser/SOA drive current and thermo-electric cooler (TEC) [196,197]. Usually the power consumption for high-power EDFA is several tens of watts [198] (it can be more for higher-power EDFAs). Thus, for SOA based nonlinear systems the total

power consumed should be in the order of 10 W, while for other passive nonlinear medium based systems the total power consumed is (laser+EDFA+nonlinear medium) several tens of watts and can exceed 100 W. Thus, effective power consumption for the nonlinear processes is lower for SOA-based systems compared with other nonlinear media and, hence, it has higher energy efficiency. We would also note here the ability to develop integrated functional components based on SOAs is key to reducing both footprint and power consumption for practical network applications.

6. OPTICAL SWITCHING

A huge demand for data processing, data storage, and communication capacity (in optical networks and data centers) motivates the search for alternatives to electrical switches and routers. Processing of big data requires huge volumes of small packets to be exchanged between the memories in the servers of data centers. Switching capacity of electrical routers is ultimately limited by the fastest clock speed and energy efficiency. Optical switching is an attractive alternative. It also has the potential to be bit-rate and modulation format agnostic, along with the ability to provide high switching speeds. Switching typically involves processing of the data at the packet level. The most desired properties of a switch are its (a) ability to buffer, (b) low insertion loss, (c) small size, (d) large port count, (e) fast switching speed, and (f) low energy consumption. Traditional low-loss implementations involving liquid crystals, microelectromechanical systems (MEMS), and piezo-based free-space optics can potentially provide a large port count, but are not viable because of their relatively low switching speeds, large footprints, high cost, and insufficient reliability. Electro-optic implementations with sufficiently high speeds are highly lossy to be useful in a practical large port count scenario.

Implementation of fast reconfigurable switches on a silicon platform is attractive because its large-scale integrability, compatibility with the CMOS process, fast switching time, and high reliability. Switching is implemented with phase shifters in one of the arms of a MZI or in a micro-ring resonator by either utilizing carrier injection (free-carrier dispersion effect) or the thermo-optic effect. IBM demonstrated a 90-nm CMOS switch with integrated electronic buffers in the 4×4 configuration, with -20 dB cross talk and only 5 mW power consumption, but its insertion loss was 3 dB [199]. In addition to the phase-change elements, thermo-optic heaters are required to correct for phase errors in any interferometer-based implementations. A 32×32 silicon-photonics chip has been demonstrated with a high-index contrast planar light wave circuit [200]. Its 1024 switches were implemented using thermo-optic phase shifters on both arms of the MZIs employed for switching. A fiber-to-fiber insertion loss of 10.8 dB, on-chip electric power consumption of 1.9 W, and a cross talk better than -20 dB (over 14.2-nm wavelength range) band was demonstrated in this implementation.

Scaling to a large number of ports is realized by cascading optical switches, but this approach is limited by high insertion losses. On-chip amplifiers, fabricated along with the switch, will help to compensate for such losses. In this context, SOAs find applications in the fabrication of optical switches as compact and small-footprint amplifiers. In addition, they also offer themselves as an alternative switching media that can provide high extinction ratios, or low cross talks, and faster switching speeds along with the gain. SOAs also have the amenability for integration and, hence, can be scaled to larger port dimensions.

A 16×16 InP-based switch was demonstrated as early as 2011 with 192 gating SOAs and with a potential energy efficiency of 3 pJ/bit [201]. Its size was 37% smaller than other similar implementations and it was suitable for 100-Gb/s packets. In this

Figure 47

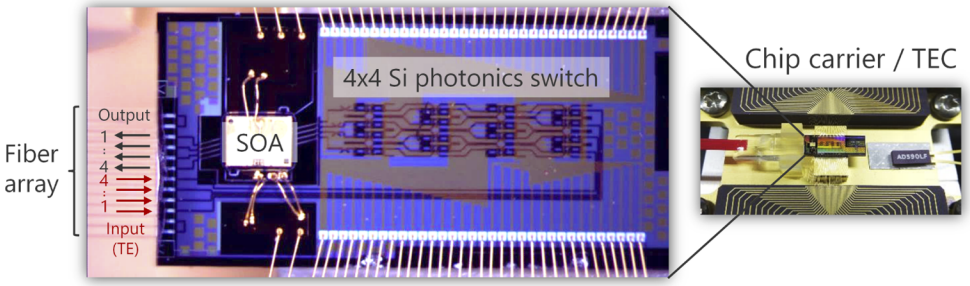

Top view of the SOA-integrated silicon photonics switch fabricated. Adapted from J. Lightwave Technol. **37**, 123 (2019) [204].

architecture, packet scheduling can be carried out within a data-center cluster without any buffering. Any switching between the clusters or to the external Internet is proposed to be carried out with a buffered router. SOAs are used not only as switching elements but also in the shuffle network that cascades smaller dimension sub-switches. The shuffle networks need to be powered to make it transparent, and to control the gain in each path. However, a large footprint of InP photonic circuits prevents the scalability of ports, considering the wafer size.

A hybrid approach, where SOAs are used as phase shifters in MZIs and short-length SOAs are used at the output of a dilated coupler as gain/loss elements, was demonstrated in Ref. [202]. The switch employed a 16×16 configuration and it exhibited an extinction ratio of 47 dB and relatively low power consumption compared with other SOA-based devices. This implementation minimized the ASE noise during the OFF state, resulting in low power consumption. An active–passive integration was demonstrated in Ref. [203] where monolithically integrated SOA gate arrays were used for switching, while the shuffle network was passive.

The flip-chip bonding technology has also been explored to integrate SOAs on top of silicon photonic platforms. Using this approach, in a recent demonstration, a 4×4 silicon-photonics had path-independent insertion loss, and it was capable of handling an eight-channel, 32-Gbaud, 16-QAM WDM signal [204]. The top view of the fabricated device is shown in Fig. 47. The circuit had also incorporated a spot-size converter with inverse taper for mode-matching the SOA and the silicon photonic circuit. The fiber-to-fiber gain of 5 dB was demonstrated, which proves that SOAs could compensate the losses incurred during a multi-stage switching process. One design issue here is the optimization of the placement of the SOA with respect to the switches. As we discussed in Section 3, finite time of the nonlinear gain response to the input optical signals has to be taken into account. In Ref. [204], the SOA array was placed after the switches to better suppress nonlinear distortions, while maintaining tolerable OSNR values for the given input power ranges in the experimental system.

Figure 48(a) shows the switch settings and Fig. 48(b) shows the Q factors measured at different input signal power levels for switching of a 16-QAM signal. It also shows measured values of the OSNR at the output at these power levels. Even though the OSNR values improve with increasing input signal power, significant nonlinear degradation occurs owing to gain-induced phase changes discussed in Section 3, and hence an optimization of input power levels becomes necessary. The experimental results suggest the optimum input power to be close to -10 dBm. Holding-beam and phase-conjugation approaches discussed in Section 3. may improve the data quality for a wider range of input power levels.

Figure 48

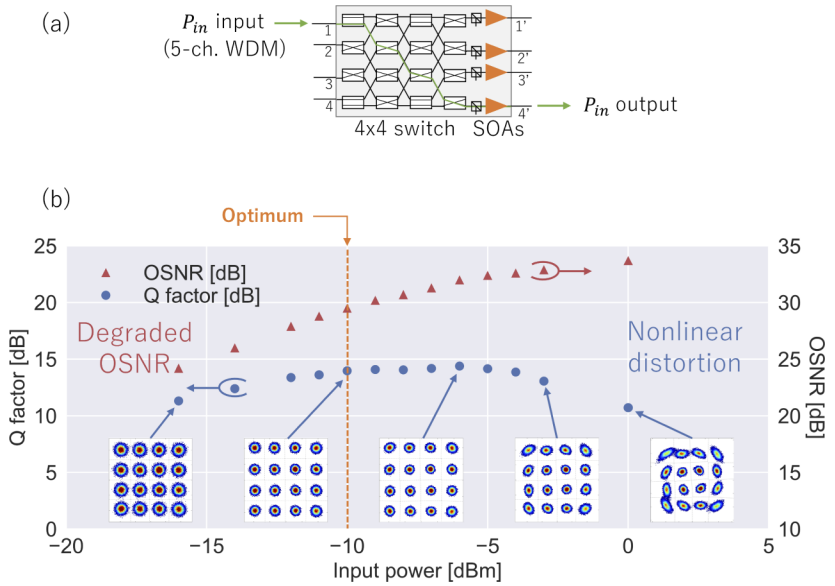

(a) Switch settings and (b) measurements of the Q factor of the output optical signal for a 4×4 silicon photonics switch containing SOAs for amplification. Adapted from J. Lightwave Technol. **37**, 123 (2019) [204].

Before integrated optical switch technologies may become practical, it is imperative to increase the number of switching ports with a larger number of WDM channels and with SOAs compensating for the cascading losses. To realize such switches, the ability to efficiently integrate the SOAs on the silicon-photonic platforms is going to be the key. It will result not only in high-performance optical switches but also in devices exploiting merits of both the SOA and silicon-photonic platforms.

7. CONCLUDING REMARKS

It should be evident from this review that SOAs have many interesting properties that make them suitable for a variety of applications. In particular, they have the potential to become important for coherent communication systems. Here, we mention a few other SOA applications that we were unable to include in details in this review.

Implementation of network functionalities in the optical domain can potentially lead to optical transparent networks that are free from bottlenecks resulting from optical–electrical–optical conversions. Header recognition is typically performed at the network nodes for routing of packets. As most all-optical header-processing systems are constrained by the number of labels that can be processed, a hybrid photonic router is envisaged, where optical processing parallelizes the header bits and electronic processing is used for each parallel channel [205]. Performing the latter functionality in the optical domain would enable all-optical routing decisions. Optical header processing using multiple header recognition systems has been demonstrated using pulse-position modulation-based techniques [206]. Optical header recognition systems have also been reported in the past for on–off data using several approaches. These include the optical correlation systems based on SOA-loop mirror, fiber Bragg gratings, and terahertz optical asymmetric demultiplexer [207,208]. The gain-recovery times limit the speed of operation of these SOA-based systems. Header recognition systems have also been demonstrated using cascaded SOA-MZI configurations for XGM [209,210]. A combination of XNOR and AND gates was used for one header processing system [211], where each logic gate was implemented using the SOA-MZI configuration. A header

recognition scheme for the BPSK data has also been realized using XNOR and AND gates with only two SOAs [212].

SOAs have found applications in the realm of microwave photonics, where the microwave (or millimeter-wave) signals are manipulated directly within the photonic domain. In one approach, such signals are used to modulate an optical carrier, which can be manipulated in the optical domain using available photonic technologies that include both active devices such as EDFAs and SOAs and passive components such as optical delay lines and filters. In an early experiment [213], a sub-carrier-multiplexed (SCM) signal was wavelength converted using FWM with only a 0.5 dB power penalty. Later studies analyzed the performance of XGM- and XPM-based wavelength conversion of an SCM signal [214]. A tunable delay line, based on the concept of slow light, has also been made through FWM inside SOAs [215,216]. There is also a body of research work that have used the SOA nonlinearities to directly manipulate the phase shift of microwave signals [217–220]. In these studies, light from a laser is modulated by a microwave carrier and is passed through an SOA, where it is allowed to undergo FWM and self-gain modulation. A controllable phase shift is impinged on the microwave signal, depending on the SOA's input optical power level and its bias current. The phase-shifting property of the SOAs also has allowed the creation of continuously tunable opto-electronic oscillators [221], tunable microwave notch filters [222,223], and a 360° phase-shifter using three cascaded SOAs.

FWM in SOAs has also been used to study correlation between two optical frequencies. There is a predictable transfer of phase from the pump and signal to the generated idler, which depends critically on the correlation properties of the pump and signal. This feature has been utilized to quantify the correlation between the spectral lines of an optical frequency comb [224,225]. There are also experiments in which SOAs are utilized for converting the data format such as NRZ-to-RZ conversion and vice versa [226–229]. In recent past, a group demonstrated the photonic digital-to-analog conversion using the red frequency chirp [230] and using the blue chirp in SOAs [231].

Recently, mode-division multiplexing in few-mode fibers have been used to substantially increase the capacity of fiber-optic links. A critical component in such systems is the few-mode fiber amplifier. The use of multimode SOAs for this purpose has been explored . The first four-mode SOA was demonstrated in Ref. [232]. A p–i–n junction with carefully designed QW layers was used to achieve the same overlap and uniform gain for all four modes. Many issues, such as minimal electrical leakage, polarization-independent operation, and minimal mode mismatch between a few-mode fiber and an SOA, need to be addressed before such SOAs become practical. SOA-based parametric amplifiers have also been studied recently for optical signal processing in few-mode telecommunication systems [233,234].

Thus, there exists a vast realm of applications areas in addition to on-chip amplification where SOAs can be put to use in coherent communication systems and microwave photonics. Further advances in nanoscale engineering to realize efficient and reliable quantum dot structures in SOA to operate in the otherwise-inaccessible wavelengths will aid in amplification and optical signal processing across the transparency band of optical fibers.

FUNDING

People Programme (Marie Curie Actions) of the European Union's Seventh Framework Programme; Scheme for Promotion of Academic and Research Collaboration; Department of Science and Technology, Ministry of Science and Technology,

India; National Science Foundation (ECCS-1933328); Science Foundation Ireland (12/RC/2276-P2, 18/EPSRC/3591); Visvesvaraya PhD Scheme (MEITY-PHD-2695).

DISCLOSURES

The authors declare no conflicts of interest.

DATA AVAILABILITY

No data were generated or analyzed in the presented research.

REFERENCES

1. M. J. O'Mahony, "Semiconductor laser optical amplifiers for use in future fiber systems," J. Lightwave Technol. **6**, 531–544 (1988).
2. S. Yamamoto, K. Mochizuki, H. Wakabayashi, and Y. Iwamoto, "Long-haul high-speed optical communication systems using a semiconductor laser amplifier," J. Lightwave Technol. **6**, 1554–1558 (1988).
3. T. Saitoh and T. Mukai, "Recent progress in semiconductor laser amplifiers," J. Lightwave Technol. **6**, 1656–1664 (1988).
4. N. A. Olsson, "Lightwave systems with optical amplifiers," J. Lightwave Technol. **7**, 1071–1082 (1989).
5. A. D'Ottavi, F. Girardin, L. Graziani, F. Martelli, P. Spano, A. Mecozzi, S. Scotti, R. Dall'Ara, J. Eckner, and G. Guekos, "Four-wave mixing in semiconductor optical amplifiers: a practical tool for wavelength conversion," IEEE J. Sel. Top. Quantum Electron. **3**, 522–528 (1997).
6. D. F. Geraghty, R. B. Lee, M. Verdiell, M. Ziari, A. Mathur, and K. J. Vahala, "Wavelength conversion for WDM communication systems using four-wave mixing in semiconductor optical amplifiers," IEEE J. Sel. Top. Quantum Electron. **3**, 1146–1155 (1997).
7. M. Asghari, I. H. White, and R. V. Penty, "Wavelength conversion using semiconductor optical amplifiers," J. Lightwave Technol. **15**, 1181–1190 (1997).
8. M. J. Connelly, *Semiconductor Optical Amplifiers* (Kluwer Academic, 2002).
9. M. Premaratne and G. P. Agrawal, *Light Propagation in Gain Media: Optical Amplifiers* (Cambridge University Press, 2011).
10. N. K. Dutta and Q. Wang, *Semiconductor Optical Amplifiers*, 2nd ed. (World Scientific, 2013).
11. K. E. Zoiros, *Applications of Semiconductor Optical Amplifiers*, 2nd ed. (MDPI, 2018).
12. T. Akiyama, M. Sugawara, and Y. Arakawa, "Quantum-dot semiconductor optical amplifiers," Proc. IEEE **95**, 1757–1766 (2007).
13. M. J. Connelly, "Wideband semiconductor optical amplifier steady-state numerical model," IEEE J. Quantum Electron. **37**, 439–447 (2001).
14. M. Connelly, Semiconductor optical amplifier model, MATLAB Central File Exchange. Retrieved 21 September 2021.
15. G. P. Agrawal and N. A. Olsson, "Self-phase modulation and spectral broadening of optical pulses in semiconductor laser amplifiers," IEEE J. Quantum Electron. **25**, 2297–2306 (1989).
16. A. Mecozzi and J. Mork, "Saturation effects in nondegenerate four-wave mixing between short optical pulses in semiconductor laser amplifiers," IEEE J. Sel. Top. Quantum Electron. **3**, 1190–1207 (1997).
17. D. Cassioli, S. Scotti, and A. Mecozzi, "A time-domain computer simulator of the nonlinear response of semiconductor optical amplifiers," IEEE J. Quantum Electron. **36**, 1072–1080 (2000).

18. G. P. Agrawal, "Population pulsations and nondegenerate four-wave mixing in semiconductor lasers and amplifiers," J. Opt. Soc. Am. B **5**, 147–159 (1988).
19. A. D'Ottavi, A. Mecozzi, S. Scotti, F. Cara Romeo, F. Martelli, P. Spano, R. Dall'Ara, J. Eckner, and G. Guekos, "Four-wave mixing efficiency in traveling wave semiconductor optical amplifiers at high saturation," Appl. Phys. Lett. **67**, 2753–2755 (1995).
20. A. Uskov, J. Moerk, and J. Mark, "Wave mixing in semiconductor laser amplifiers due to carrier heating and spectral hole burning," IEEE J. Quantum Electron. **30**, 1769–1781 (1994).
21. H. Ghafouri-Shiraz, *The Principles of Semiconductor Laser Diodes and Amplifiers* (Imperial College Press, London, 2004).
22. G. Toptchiyski, S. Kindt, K. Petermann, E. Hilliger, S. Diez, and H. G. Weber, "Time-domain modeling of semiconductor optical amplifiers for OTDM applications," J. Lightwave Technol. **17**, 2577–2583 (1999).
23. https://www.thorlabs.com/drawings/fd59ab3030160c8a-92200DD0-B9B3-3044-42399691F4006F10/SOA1013S-SpecSheet.pdf Accessed May 2022.
24. https://www.thorlabs.com/drawings/fd59ab3030160c8a-92200DD0-B9B3-3044-42399691F4006F10/SOA1117P-SpecSheet.pdf Accessed May 2022.
25. C. H. Henry, "Theory of the phase noise and power spectrum of a single mode injection laser," IEEE J. Quantum Electron. **19**, 1391–1397 (1983).
26. S. P. O'Duill and L. Barry, "Improved reduced models for single-pass and reflective semiconductor optical amplifiers," Opt. Commun. **334**, 170–173 (2015).
27. S. Philippe, A. L. Bradley, R. Maldonado-Basilio, F. Surre, B. F. Kennedy, P. Landais, and H. Soto-Ortiz, "Polarization dependence of non-linear gain compression factor in semiconductor optical amplifier," Opt. Express **16**, 8641–8648 (2008).
28. S. Fu, M. Wang, W.-D. Zhong, P. Shum, Y. J. Wen, J. Wu, and J. Lin, "SOA nonlinear polarization rotation with linear polarization maintenance: characterization and applications," IEEE J. Sel. Top. Quantum Electron. **14**, 816–825 (2008).
29. B. S. Gopalakrishnapillai, M. Premaratne, A. Nirmalathas, and C. Lim, "Power equalization using polarization rotation in semiconductor optical amplifiers," IEEE Photonics Technol. Lett. **17**, 1695–1697 (2005).
30. S. P. O'Duill, A. Anthur, T. Huynh, D. Venkitesh, and L. P. Barry, "Numerical generation of laser-resonance phase noise for optical communication simulators," Appl. Opt. **54**, 3398–3406 (2015).
31. S. P O'Duill, P. Landais, and L. P. Barry, "Estimation of the performance improvement of pre-amplified PAM4 systems when using multi-section semiconductor optical amplifiers," Appl. Sci. **7**, 908 (2017).
32. S. P. O'Duill, S. T. Naimi, A. Anthur, D. Venkitesh, and L. P. Barry, "Simulations of an OSNR-limited all-optical wavelength conversion scheme," IEEE Photonics Technol. Lett. **25**, 2311–2314 (2013).
33. S. T. Naimi and S. P. O'Duill, "Simulations of the OSNR and Laser linewidth limits for reliable wavelength conversion of DQPSK signals using four-wave mixing," Opt. Commun. **310**, 150–155 (2014).
34. S. T. Naimi, S .P. O'Duill, and L. P. Barry, "All optical wavelength conversion of Nyquist-WDM superchannels using FWM in SOAs," J. Lightwave Technol. **33**, 3959–3967 (2015).
35. W. Way, T. Chan, and A. Lebedev, "Technical feasibility study of 56 Gb/s and 112 Gb/s PAM-4 transmission," presented at the IEEE Meeting on P802.3bs Task Force 200 GbE and 400 GbE, Norfolk, VA, USA, 12–14 May 2014.

36. M. A. Summerfied and R. S. Tucker, "Frequency-domain model of multiwave mixing in bulk semiconductor optical amplifiers," IEEE J. Sel. Top. Quantum Electron. **5**, 839–850 (1999).
37. R. N. Bracewell, *The Fourier Transform and Its Applications* (McGraw Hill, New York, 1999).
38. A. Mecozzi, S. Scotti, A. D'Ottavi, E. Iannone, and P. Spano, "Four-wave mixing in travelling-wave semiconductor optical amplifiers," IEEE J. Quantum Electron. **31**, 689–699 (1995).
39. M. J. Connelly, "Wideband steady-state numerical model and parameter extraction of a tensile strained bulk semiconductor optical amplifier," IEEE J. Quantum Electron. **43**, 47–56 (2007).
40. S. Balle, "Simple analytical approximations for the gain and refractive index spectra in quantum well lasers," Phys. Rev. A **57**, 1304–1312 (1998).
41. M. G. Cara, L. Occhi, and S. Balle, "Modeling and measurement of the wavelength-dependent output properties of quantum-well optical amplifiers: effects of a carrier-dependent escape time," IEEE J. Sel. Top. Quantum Electron. **9**, 783–787 (2003).
42. S. Bauer, V. Sichkovsckyi, O. Eyal, T. Septon, A. Becker, I. Khanonkin, G. Eisenstein, and J. P. Reithmeier, "1.5 μm indium phosphide-based quantum dot lasers and optical amplifiers," IEEE Nanotechnol. Mag. **15**, 23–36 (2021).
43. D. Hadass, A. Bilenca, H. Dery, V. Mikhelashvili, G. Eisenstein, R. Schwertberger, A. Somers, J. P. Reithmeier, A. Forchel, M. Calligaro, S. Bansropun, and M. Krakowski, "Gain and noise saturation of wide-band InAs-InP quantum dash optical amplifiers: model and experiments," IEEE J. Sel. Top. Quantum Electron. **11**, 1015–1026 (2005).
44. R. J. Mears, L. Reekie, I. M. Jauncey, and D. N. Payne, "Low-noise erbium-doped fibre amplifier at 1.54 μm," Electron. Lett. **23**, 1026–1028 (1987).
45. H. Takara, K. Uchiyama, I. Shake, and K. Mori, "3 Tbit/s (16O Gbit/s × l9ch) OTDM/WDM transmission experiment," in *Optical Fiber Commun. Conf.* (1999), paper PD1.
46. A. Ghazisaeidi, I. F. de Jauregui Ruiz, R. Rios-Müller, L. Schmalen, P. Tran, P. Brindel, A. Carbo Meseguer, Q. Hu, F. Buchali, G. Charlet, and J. Renaudier, "Advanced C+L-band transoceanic transmission systems based on probabilistically shaped PDM-64QAM," J. Lightwave Technol. **35**, 1291–1299 (2017).
47. J-X. Cai, H. G. Batshon, M. V. Mazurczyk, O. V. Sinkin, D. Wang, M. Paskov, W. W. Patterson, C. R. Davidson, P. C. Corbett, G. M. Wolter, T. E. Hammon, M. A. Bolshtyansky, D. G. Foursa, and A. N. Pilipetskii, "70.46 Tb/s Over 7, 600 km and 71.65 Tb/s Over 6, 970 km transmission in C+L band using coded modulation with hybrid constellation shaping and nonlinearity compensation," J. Lightwave Technol. **36**, 114–121 (2018).
48. J. Bromage, "Raman amplification for fiber communications systems," J. Lightwave Technol. **22**, 79–93 (2004).
49. J.-X. Cai, Y. Sun, H. G. Batshon, M. Mazurczyk, H. Zhang, D. G. Foursa, and A. N. Pilipetskii, *54 Tb/s Transmission over 9,150 km with Optimized Hybrid Raman-EDFA Amplification and Coded Modulation* (European Conf. Optical Commun., 2014), pp. 1–3.
50. J. Pedro and N. Costa, "Optimized hybrid Raman/EDFA amplifier placement for DWDM mesh networks," J. Lightwave Technol. **36**, 1552–1561 (2018).
51. T. Kobayashi, S. Shimizu, M. Nakamura, T. Umeki, T. Kazama, R. Kasahara, F. Hamaoka, M. Nagatani, H. Yamazaki, H. Nosaka, and Y. Miyamoto, "Wideband inline-amplified WDM transmission using PPLN-based optical parametric amplifier," J. Lightwave Technol. **39**, 787–794 (2021).

52. J. Renaudier and A. Ghazisaeidi, "Scaling capacity growth of fiber-optic transmission systems using 100+ nm ultra-wideband semiconductor optical amplifiers," J. Lightwave Technol. **37**, 1831–1838 (2019).
53. Q. Xu, M. Yao, Y. Dong, W. Cai, and J. Zhang, "Experimental demonstration of pattern effect compensation using an asymmetrical Mach–Zehnder interferometer with SOAs," IEEE Photonics Technol. Lett. **13**, 1325–1327 (2001).
54. E. E. Patent, V. Tol, M. L. Nielsen, J. H. Binsma, Y. Oei, J. Mørk, and M. Smit, "Integrated SOA-MZI for pattern-effect-free amplification," Electron. Lett. **41**, 549–551 (2005).
55. G. Amirhossein and Ann Rusch Leslie, "On the efficiency of digital back-propagation for mitigating SOA-induced nonlinear impairments," J. Lightwave Technol. **29**, 3331–3339 (2011).
56. J. G. L. Jennen, R. C. J. Smets, H. De Waardt, G. N. van den Hoven, and A. J. Boot, "4×10 Gbit/s NRZ transmission in the 1310 nm window over 80 km of standard single mode fibre using semiconductor optical amplifiers," in *European Conf. Optical Commun.*, (1998), pp. 235–236.
57. Y. Kim, H. Jang, Y. Kim, J. Lee, D. Jang, and J. Jeong, "Transmission performance of 10-Gb/s 1550-nm transmitters using semiconductor optical amplifiers as booster amplifiers," J. Lightwave Technol. **21**, 476–481 (2003).
58. L. H. Spiekman, J. M. Wiesenfeld, A. H. Gnauck, L. D. Garrett, G. N. Van Den Hoven, T. Van Dongen, M. J. H. Sander-Jochem, and J. J. M. Binsma, "Transmission of 8 DWDM channels at 20 Gb/s over 160 km of standard fiber using a cascade of semiconductor optical amplifiers," IEEE Photonics Technol. Lett. **12**, 717–719 (2000).
59. L. H. Spiekman, J.M. Wiesenfeld, A.H. Gnauck, L.D. Garrett, G.N. van den Hoven, T. van Dongen, M.J.H. Sander-Jochem, and J.J.M. Binsma, "8×10 Gb/s DWDM transmission over 240 km of standard fiber using a cascade of semiconductor optical amplifiers," IEEE Photonics Technol. Lett. **12**, 1082–1084 (2000).
60. Y. Sun, A. K. Srivastava, S. Baneijee, J. W. Sulhoff, R. Pan, K. Kantor, R. M. Jopson, and A. R. Chraplyvy, "Error-free transmission of 32 × 2.5 Gb/s DWDM channels over 125 km of all-wave fiber using cascaded in-line semiconductor optical amplifiers," in *Optical Amplifiers and Applications Conf.* (1999), paper SN3.
61. Y. Sun, A. K. Srivastava, S. Baneijee, J. W. Sulhoff, R. Pan, K. Kantor, R. M. Jopson, and A. R. Chraplyvy, "Error-free transmission of 32×2.5 Gbit/s DWDM channels over 125 km using cascaded in-line semiconductor optical amplifiers," Electron. Lett. **35**, 1863–1865 (1999).
62. S. Banerjee, A.K. Srivastava, Y. Sun, J.W. Sulhoff, K. Kantor, and C. Wolf, "Cascaded semiconductor optical amplifiers for transmission of 32 DWDM channels over 315 km," in *Optical Fiber Commun. Conf.* (2000), paper WM32.
63. A. H. Gnauck, L. H. Spiekman, J. M. Wiesenfeld, and L. D. Garrett, "Dynamic add/drop of 8-of-16 l0-Gb/s channels in 4x40 km semiconductor optical amplifier-based WDM system," in *Optical Fiber Commun. Conf.* (2000), paper PD39.
64. P. J. Urban, E. G. C. Pluk, M. M. de Laat, F. M. Huijskens, G. D. Khoe, A. M. J. Koonen, and H. de Waardt, "1.25-Gb/s transmission over an access network link with tunable OADM and a reflective SOA," IEEE Photonics Technol. Lett. **21**, 380–382 (2009).
65. E. Wong, K. L. Lee, and T. B. Anderson, "Directly modulated self-seeding reflective semiconductor optical amplifiers as colorless transmitters in wavelength division multiplexed passive optical networks," J. Lightwave Technol. **25**, 67–74 (2007).

66. R. Bonk, H. Schmuck, W. Poehlmann, and T. Pfeiffer, "Beneficial OLT transmitter and receiver concepts for NG-PON2 using semiconductor optical amplifiers [invited]," J. Opt. Commun. Netw. **7**, A467–A473 (2015).
67. S. Sarmiento, J. M. D. Mendinueta, J. A. Altabás, S. Spadaro, S. Shinada, H. Furukawa, J. V. Olmos, J. A. Lázaro, and N. Wada, "Optical power budget enhancement in 50–90 Gb/s IM-DD PONs with NOMA-CAP and SOA-based amplification," IEEE Photonics Technol. Lett. **32**, 608–611 (2020).
68. A. Ghazisaeidi, "Theory of coherent WDM systems using in-line semiconductor optical amplifiers," J. Lightwave Technol. **37**, 4188–4200 (2019).
69. A. Arnould, A. Ghazisaeidi, D. Le Gac, P. Brindel, M. Makhsiyan, K. Mekhazni, F. Blache, M. Achouche, and J. Renaudier, "Experimental characterization of nonlinear distortions of semiconductor optical amplifiers in the WDM regime," J. Lightwave Technol. **38**, 509–513 (2020).
70. A. Arnould, A. Ghazisaeidi, D. Le Gac, P. Brindel, M. Makhsiyan, K. Mekhazni, F. Blache, N. Fontaine, D. Neilson, R. Ryf, H. Chen, M. Achouche, and J. Renaudier, "103 nm ultra-wideband hybrid raman/SOA transmission over 3 × 100 km SSMF," J. Lightwave Technol. **38**, 504–508 (2020).
71. R. Bonk, G. Huber, T. Vallaitis, S. Koenig, R. Schmogrow, D. Hillerkuss, R. Brenot, F. Lelarge, G.-H. Duan, S. Sygletos, C. Koos, W. Freude, and J. Leuthold, "Linear semiconductor optical amplifiers for amplification of advanced modulation formats," Opt. Express **20**, 9657–9672 (2012).
72. S. Koenig, R. Bonk, H. Schmuck, W. Poehlmann, Th. Pfeiffer, C. Koos, W. Freude, and J. Leuthold, "Amplification of advanced modulation formats with a semiconductor optical amplifier cascade," Opt. Express **22**, 17854–17871 (2014).
73. A. Mecozzi and J. Mørk, "Saturation induced by picosecond pulses in semiconductor optical amplifiers," J. Opt. Soc. Am. B **14**, 761–770 (1997).
74. X. Wei and L. Zhang, "Analysis of the phase noise in saturated SOAs for DPSK applications," IEEE J. Quantum Electron. **41**, 554–561 (2005).
75. R. Gutiérrez-Castrejón and A. Filios, "Pattern-effect reduction using a cross-gain modulated holding beam in semiconductor optical in-line amplifier," J. Lightwave Technol. **24**, 4912–4917 (2006).
76. L. Xue, L. Yi, R. Lin, L. Huang, and J. Chen, "SOA pattern effect mitigation by neural network based pre-equalizer for 50G PON," Opt. Express **29**, 24714–24722 (2021).
77. K. Inoue and M. Yoshino, "Gain dynamics of a saturated semiconductor laser amplifier with 1.47 μm LD pumping," IEEE Photonics Technol. Lett. **8**, 506–508 (1996).
78. M. A. Dupertuis, J. L. Pleumeekers, T. P. Hessler, P. E. Selbmann, B. Deveaud, B. Dagens, and J.Y. Emery, "Extremely fast high-gain and low-current SOA by optical speed-up at transparency," IEEE Photonics Technol. Lett. **12**, 1453–1455 (2000).
79. S. Aneesh and V. Deepa, "Low-distortion amplification of single channel QPSK/16QAM signals using SOA with HBeam," paper SpM2I.5, SPPCom 2020.
80. A. Sobhanan, M. Pelusi, T. Inoue, S. Namiki, and D. Venkitesh, "Low distortion amplification of 16 and 64QAM signals using SOA," Opt. Commun. **502**, 127331 (2022).
81. G. P. Agrawal and C. M. Bowden, "Concept of linewidth enhancement factor in semiconductor lasers: its usefulness and limitations," IEEE Photonics Technol. Lett. **5**, 640–642 (1993).
82. A. Sobhanan, M. Pelusi, T. Inoue, D. Venkitesh, and S. Namiki, "Compensation of SOA nonlinear distortions by mid-stage optical phase conjugation," in *Optical Fiber Commun. Conf.* (2020), paper M1I.5.

83. A. Sobhanan, M. Pelusi, T. Inoue, D. Venkitesh, and S. Namiki, "Compensation of SOA-induced nonlinear phase distortions by optical phase conjugation," Opt. Express **29**, 12252–12265 (2021).
84. W. Mathlouthi, F. Vacondio, P. Lemieux, and L. A. Rusch, "SOA gain recovery wavelength dependence: simulation and measurement using a single-color pump–probe technique," Opt. Express **16**, 20656–20665 (2008).
85. H. J. S. Dorren, D. Lenstra, Y. Liu, M. T. Hill, and G. D. Khoe, "Nonlinear polarization rotation in semiconductor optical amplifiers: theory and application to all-optical flip-flop memories," IEEE J. Quantum Electron. **39**, 141–148 (2003).
86. A. Marculescu, S. Ó Dúill, C. Koos, W. Freude, and J. Leuthold, "Spectral signature of nonlinear effects in semiconductor optical amplifiers," Opt. Express **25**, 29526–29559 (2017).
87. K. Ishii, T. Inoue, I. Kim, X. Wang, H. N. Tan, Q. Zhang, T. Ikeuchi, and S. Namiki, "Analysis and demonstration of network utilization improvement through format-agnostic multi-channel wavelength converters," J. Opt. Commun. Netw. **10**, A165–A174 (2018).
88. E. Ciaramella, "Wavelength conversion and all-optical regeneration: achievements and open issues," J. Lightwave Technol. **30**, 572–582 (2012).
89. Y. Lee, D. Lee, G. Bernstein, and G. Martinelli, "A framework for the control of wavelength switched optical networks (WSON) with impairments," Internet Engineering Task Force (IETF) Document (2012).
90. R. Ramaswami and K. N. Sivarajan, "Routing and wavelength assignment in all-optical networks," IEEE/ACM Trans. Networking **3**, 489–500 (1995).
91. J. M. H. Elmirghani and H. T. Mouftah, "All-optical wavelength conversion: technologies and applications in DWDM networks," IEEE Commun. Mag. **38**, 86–92 (2000).
92. O. Aso, M. Tadakuma, and S. Namiki, "Four-wave mixing in optical fibers and its applications," Furukawa Rev. **1**, 63–68 (2000).
93. G. P. Agrawal, "Nonlinear fiber optics: its history and recent progress [Invited]," J. Opt. Soc. Am. B **28**, A1–A10 (2011).
94. S. J. B. Yoo, "Wavelength conversion technologies for WDM network applications," J. Lightwave Technol. **14**, 955–966 (1996).
95. T. Durhuus, B. Mikkelsen, C. Joergensen, S. L. Danielsen, and K. E. Stubkjaer, "All-optical wavelength conversion by semiconductor optical amplifier," J. Lightwave Technol. **14**, 942–954 (1996).
96. A. Kapsalis, H. Simos, D. Syvridis, M. Hamacher, and H. Heidrich, "Tunable wavelength conversion using cross-gain modulation in a vertically coupled microring laser," IEEE Photonics Technol. Lett. **21**, 1618–1620 (2009).
97. A. A. E. Hajomer, M. Presi, N. Andriolli, C. Porzi, W. Hu, G. Contestabile, and X. Yang, "On-chip all-optical wavelength conversion of PAM-4 signals using an integrated SOA-based turbo-switch circuit," J. Lightwave Technol. **37**, 3956–3962 (2019).
98. H. Song, J. Seon Lee, and J. Song, "Signal up-conversionby using a cross-phase-modulation in all-optical SOA-MZI wavelength converter," IEEE Photonics Technol. Lett. **16**, 593–595 (2004).
99. C. Joergensen, S. L. Danielsen, T. Durhuus, B. Mikkelsen, K. E. Stubkjaer, N. Vodjdani, F. Ratovelomanana, A. Enard, G. Glastre, D. Rondi, and R. Blondeau, "Wavelength conversion by optimized monolithic integrated Mach–Zehnder interferometer," IEEE Photonics Technol. Lett. **8**, 521–523 (1996).
100. Y. Ye, X. Zheng, H. Zhang, Y. Li, and Y. Guo, "Study on the dynamic range of input power for wavelength converter based on cross-phase modulation in SOAs," Opt. Commun. **200**, 349–354 (2001).

101. P. P. Baveja, Y. Xiao, S. Arora, G. P. Agrawal, and D. N. Maywar, "All-optical semiconductor optical amplifier-based wavelength converters with sub-mW pumping," IEEE Photonics Technol. Lett. **25**, 78–80 (2013).
102. G. P. Agrawal, "Four-wave mixing and phase conjugation in semiconductor laser media," Opt. Lett. **12**, 260–262 (1987).
103. A. P. Anthur, R. T. Watts, K. Shi, J. O'Carroll, D. Venkitesh, and L. P. Barry, "Dual correlated pumping scheme for phase noise preservation in all-optical wavelength conversion," Opt. Express **21**, 15568–15579 (2013).
104. R. Hui and A. Mecozzi, "Phase noise of four-wave mixing in semiconductor lasers," Appl. Phys. Lett. **60**, 2454–2456 (1992).
105. A. P. Anthur, R. Zhou, S. O'Duill, A. J. Walsh, E. Martin, D. Venkitesh, and L. P. Barry, "Polarization insensitive all-optical wavelength conversion of polarization multiplexed signals using co-polarized pumps," Opt. Express **24**, 11749–11761 (2016).
106. A. P. Anthur, S. O'Duill, and L. P. Barry, "Investigation of intensity noise transfer during four-wave mixing in nonlinear optical media," J. Opt. Soc. Am. B **34**, 389–396 (2017).
107. P. P. Baveja, D. N. Maywar, and G. P. Agrawal, "Interband four-wave mixing in semiconductor optical amplifiers with ASE-enhanced gain recovery," IEEE J. Sel. Top. Quantum Electron. **18**, 899–908 (2012).
108. Y. Lin, E. Giacoumidis, S. O'Duill, and L. P. Barry, "DBSCAN-based clustering for nonlinearity induced penalty reduction in wavelength conversion systems," IEEE Photonics Technol. Lett. **31**, 1709–1712 (2019).
109. A. H. Gnauck and P. J. Winzer, "Optical phase-shift-keyed transmission," J. Lightwave Technol. **23**, 115–130 (2005).
110. K. O. Hill, D. C. Johnson, B. S. Kawasaki, and R. I. MacDonald, "cw three-wave mixing in single-mode optical fibers," J. Appl. Phys. **49**, 5098–5106 (1978).
111. T. Tanemura, Han Chuen Lim, and K. Kikuchi, "Suppression of idler spectral broadening in highly efficient fiber four-wave mixing by binary-phase-shift-keying modulation of pump wave," IEEE Photonics Technol. Lett. **13**, 1328–1330 (2001).
112. T. Tanemura and K. Kikuchi, "Polarization-independent broad-band wavelength conversion using two-pump fiber optical parametric amplification without idler spectral broadening," IEEE Photonics Technol. Lett. **15**, 1573–1575 (2003).
113. H. Min-Chen, "Narrow-linewidth idler generation in fiber four-wave mixing and parametric amplification by dithering two pumps in opposition of phase," J. Lightwave Technol. **20**, 469–476 (2002).
114. K. Torii and S. Yamashita, "Cancellation of spectral spread by pump frequency modulation in optical fiber wavelength converter," in *Optical Fiber Commun. Conf.* (2001), paper WW5.
115. S. Yamashita and M. Tani, "Cancellation of spectral spread in SBS-suppressed fiber wavelength converters using a single phase modulator," IEEE Photonics Technol. Lett. **16**, 2096–2098 (2004).
116. K. K. Y. Wong, M. E. Marhic, and L. G. Kazovsky, "Phase-conjugate pump dithering for high-quality idler generation in a fiber optical parametric amplifier," IEEE Photonics Technol. Lett. **15**, 33–35 (2003).
117. T. Zhi, O. J. Wiberg Andreas, M. Evgeny, P. P. Kuo Bill, A. Nikola, and R. Stojan, "Spectral linewidth preservation in parametric frequency combs seeded by dual pumps," Opt. Express **20**, 17610–17619 (2012).
118. A. P. Anthur, R. T. Watts, S. O'Duill, R. Zhou, D. Venkitesh, and L. P. Barry, "Impact of nonlinear phase noise on all-optical wavelength conversion of 10.7-GBaud QPSK data using dual correlated pumps," IEEE J. Quantum Electron. **51**, 1–5 (2015).

119. Y. Lin, E. Giacoumidis, S. O'Duill, A. P. Anthur, and L. P. Barry, "Reduction of nonlinear distortion in SOA-based wavelength conversion system by post-blind-compensation based on machine learning clustering," in *Optical Fiber Commun. Conf.* (2019), paper Th2A.35.
120. A. P. Anthur, R. T. Watts, R. Zhou, P. Anandarajah, D. Venkitesh, and L. P. Barry, "Penalty-free wavelength conversion with variable channel separation using gain-switched comb source," Opt. Commun. **324**, 69–72 (2014).
121. Y. Lin, A. P. Anthur, S. O'Duill, S. T. Naimi, Y. Yu, and L. P. Barry, "Fast reconfigurable SOA-based all-optical wavelength conversion of QPSK data employing switching tunable pump lasers," *Optical Fiber Commun. Conf.* (2017), pp. 1–3.
122. Y. Lin, A. P. Anthur, S. O'Duill, F. Liu, Y. Yu, and L. P. Barry, "Fast reconfigurable soa-based wavelength conversion of advanced modulation format data," Appl. Sci. **7**, 1033 (2017).
123. Optical Impairment-Aware W. S. O. N. Control Plane, Cisco ONS, 15454 MSTP.
124. G. Contestabile, L. Banchi, M. Presi, and E. Ciaramella, "Investigation of transparency of FWM in SOA to advanced modulation formats involving intensity, phase, and polarization multiplexing," J. Lightwave Technol. **27**, 4256–4261 (2009).
125. O. Aso, M. Tadakuma, and S. Namiki, "Four-wave mixing in optical fibers and its applications," Furukawa Rev. **19**, 63–68 (2000).
126. R. Schnabel, U. Hilbk, T. Hermes, P. Meissner, C. Helmolt, K. Magari, F. Raub, W. Pieper, F. J. Westphal, R. Ludwig, L. Kuller, and H. G. Weber, "Polarization insensitive frequency conversion of a 10-channel OFDM signal using four-wave-mixing in a semiconductor laser amplifier," IEEE Photonics Technol. Lett. **6**, 56–58 (1994).
127. G. Contestabile, Y. Yoshida, A. Maruta, and K. Kitayama, "Ultra-broad band, low power, highly efficient coherent wavelength conversion in quantum dot SOA," Opt. Express **20**, 27902–27907 (2012).
128. K. Georgakilas and A. Tzanakaki, "The impact of optical wavelength conversion on the energy efficiency of resilient WDM optical networks," in *2011 13th International Conference on Transparent Optical Networks* (2011), pp. 1–4.
129. S. J. Savory, G. Gavioli, R. I. Killey, and P. Bayvel, "Electronic compensation of chromatic dispersion using a digital coherent receiver," Opt. Express **15**, 2120–2126 (2007).
130. A. Amari, X. Lin, O. A. Dobre, R. Venkatesan, and A. Alvarado, "A machine learning-based detection technique for optical fiber nonlinearity mitigation," IEEE Photonics Technol. Lett. **31**, 627–630 (2019).
131. T. Umeki, T. Kazama, A. Sano, K. Shibahara, K. Suzuki, M. Abe, H. Takenouchi, and Y. Miyamoto, "Simultaneous nonlinearity mitigation in 92×180-Gbit/s PDM-16QAM transmission over 3840 km using PPLN-based guard-band-less optical phase conjugation," Opt. Express **24**, 16945–16951 (2016).
132. M. A. Z. Al-Khateeb, M. Tan, M. Asif Iqbal, A. Ali, M. E. McCarthy, P. Harper, and A. D. Ellis, "Experimental demonstration of 72% reach enhancement of 3.6 Tbps optical transmission system using mid-link optical phase conjugation," Opt. Express **26**, 23960–23968 (2018).
133. K. R. H. Bottrill, N. Taengnoi, F. Parmigiani, D. J. Richardson, and P. Petropoulos, "PAM4 transmission over 360 km of fibre using optical phase conjugation," OSA Continuum **2**, 973–982 (2019).
134. M. Al-Khateeb, M. Tan, T. Zhang, and A. D. Ellis, "Combating fiber nonlinearity using dual-order raman amplification and OPC," IEEE Photonics Technol. Lett. **31**, 877–880 (2019).
135. P. V. Mamyshev, "All-optical data regeneration based on self-phase modulation effect," European Conf. Optical Commun. **1998**, 475–476 (1998).

136. T. I. Lakoba and M. Vasilyev, "On multi-channel operation of phase-preserving 2R amplitude regenerator," Opt. Commun. **322**, 114–117 (2014).
137. J. K. Lucek and K. Smith, "All-optical signal regenerator," Opt. Lett. **18**, 1226–1228 (1993).
138. C. M. Caves, "Quantum limits on noise in linear amplifiers," Phys. Rev. D **26**, 1817–1839 (1982).
139. J. A. Levenson, I. Abram, T. Rivera, and P. Grangier, "Reduction of quantum noise in optical parametric amplification," J. Opt. Soc. Am. B **10**, 2233–2238 (1993).
140. T. Inagaki, K. Inaba, R. Hamerly, K. Inoue, Y. Yamamoto, and H. Takesue, "Large-scale Ising spin network based on degenerate optical parametric oscillators," Nat. Photonics **10**, 415–419 (2016).
141. Z. Y. Ou, "Enhancement of the phase-measurement sensitivity beyond the standard quantum limit by a nonlinear interferometer," Phys. Rev. A **85**, 023815 (2012).
142. F. Hudelist, J. Kong, C. Liu, J. Jing, Z. Y. Ou, and W. Zhang, "Quantum metrology with parametric amplifier-based photon correlation interferometers," Nat. Commun. **5**, 3049 (2014).
143. P. A. Andrekson and M. Karlsson, "Fiber-based phase-sensitive optical amplifiers and their applications," Adv. Opt. Photonics **12**, 367–428 (2020).
144. B. J. Puttnam, D. Mazroa, S. Shinada, and N. Wada, "Phase-squeezing properties of non-degenerate PSAs using PPLN waveguides," Opt. Express **19**, B131–B139 (2011).
145. T. Umeki, M. Asobe, and H. Takenouchi, "In-line phase sensitive amplifier based on PPLN waveguides," Opt. Express **21**, 12077–12084 (2013).
146. M. A. Ettabib, K. Bottrill, F. Parmigiani, A. Kapsalis, A. Bogris, M. Brun, P. Labeye, S. Nicoletti, K. Hammani, D. Syvridis, D. J. Richardson, and P. Petropoulos, "All-optical phase regeneration with record PSA extinction ratio in a low-birefringence silicon germanium waveguide," J. Lightwave Technol. **34**, 3993–3998 (2016).
147. T. Ducellier and M. B. Bibey, "Study of optical phase conjugation in bulk traveling wave semiconductor optical amplifier," IEEE Photonics Technol. Lett. **8**, 530–532 (1996).
148. A. Mecozzi, G. Contestabile, L. Graziani, F. Martelli, A. D'Ottavi, and P. Spano, "Polarization-insensitive four-wave mixing in a semiconductor optical amplifier," Appl. Phys. Lett. **72**, 2651–2653 (1998).
149. L. Wang, M. Gao, M. Liu, H. Zhu, B. Chen, and L. Xiang, "Energy-efficient all optical wavelength converter for optical phase conjugation," Opt. Fiber Technol. **58**, 102278 (2020).
150. A. Sobhanan, V. A. M. Karthik, L. V. Narayanan, R. D. Koilpillai, and D. Venkitesh, "Experimental analysis of noise transfer in optical phase conjugation process in nonlinear SOA," in *Optical Fiber Commun. Conf.* (2019), paper W2A.38.
151. A. Sobhanan and D. Venkitesh, "Polarization-insensitive phase conjugation using single pump Bragg-scattering four-wave mixing in semiconductor optical amplifiers," Opt. Express **26**, 22761–22772 (2018).
152. A. Sobhanan, L. N. Venkatasubramani, R. D. Koilpillai, and D. Venkitesh, "Polarization-insensitive phase conjugation of QPSK signal using Bragg-scattering FWM in SOA," IEEE Photonics Technol. Lett. **31**, 919–922 (2019).
153. C. Lorattanasane and K. Kikuchi, "Design theory of long-distance optical transmission systems using midway optical phase conjugation," J. Lightwave Technol. **15**, 948–955 (1997).

154. S. Watanabe and M. Shirasaki, "Exact compensation for both chromatic dispersion and Kerr effect in a transmission fiber using optical phase conjugation," J. Lightwave Technol. **14**, 243–248 (1996).
155. K. Kikuchi and K. Matsuura, "Transmission of 2-ps optical pulses at 1550 nm over 40-km standard fiber using mid-span optical phase conjugation in semiconductor optical amplifiers," IEEE Photonics Technol. Lett. **10**, 1410–1412 (1998).
156. D. D. Marcenac, D. Nesset, A. E. Kelly, M. Brierley, A. D. Ellis, D. G. Moodie, and C. W. Ford, "40 Gbit/s transmission over 406 km of NDSF using mid-span spectral inversion by four-wave-mixing in a 2-mm-long semiconductor optical amplifier," Electron. Lett. **33**, 879–880 (1997).
157. D. D. Marcenac, D. Nesset, A. E. Kelly, and D. Gavrilovic, "40 Gbit/s transmission over 103 km of NDSF using polarisation independent mid-span spectral inversion by four-wave mixing in a semiconductor optical amplifier," Electron. Lett. **34**, 100–101 (1998).
158. R. Seki, T. Yatsu, and M. Matsuura, "100 km transmission of RZ-DPSK signal using optical phase conjugation in a QD-SOA," IEICE Tech. Rep. **114**, 121–124 (2015).
159. H. Hu, L. Han, R. Ludwig, C. Schmidt-Langhorst, J. Yu, and C. Schubert, "107 Gb/s RZ-DQPSK signal transmission over 108 km SMF using optical phase conjugation in an SOA," in *Optical Fiber Commun. Conf.* (2009), paper OThF6.
160. A. Sobhanan, L. N. Venkatasubramani, R. D. Koilpillai, and D. Venkitesh, "Dispersion and nonlinearity distortion compensation of the QPSK/16QAM signals using optical phase conjugation in nonlinear SOAs," IEEE Photonics J. **12**, 1–7 (2020).
161. L. N. Venkatasubramani, A. Sobhanan, A. Vijay, R. D. Koilpillai, and D. Venkitesh, "Optical phase conjugation using nonlinear SOA for nonlinearity and dispersion compensation of coherent multi-carrier lightwave systems," IEEE Access **9**, 44059–44068 (2021).
162. L. N. Venkatasubramani, A. Vijay, D. Venkitesh, and R. D. Koilpillai, "Pilot-free common phase error estimation for CO-OFDM with improved spectral efficiency," IEEE Photonics J. **11**, 1–10 (2019).
163. J. Hansryd and P. A. Andrekson, "Broad-band continuous-wave-pumped fiber optical parametric amplifier with 49-dB gain and wavelength-conversion efficiency," IEEE Photonics Technol. Lett. **13**, 194–196 (2001).
164. J. Hansryd, P. A. Andrekson, M. Westlund, J. Li, and P. O. Hedekvist, "Fiber-based optical parametric amplifiers and their applications," IEEE J. Sel. Top. Quantum Electron. **8**, 506–520 (2002).
165. T. Torounidis, P. A. Andrekson, and B. Olsson, "Fiber-optical parametric amplifier with 70-dB gain," IEEE Photonics Technol. Lett. **18**, 1194–1196 (2006).
166. R. Slavík, F. Parmigiani, J. Kakande, C. Lundström, M. Sjödin, P. A. Andrekson, R. Weerasuriya, S. Sygletos, A. D. Ellis, L. G. Nielsen, D. Jakobsen, S. Herstrøm, R. Phelan, J. O'Gorman, A. Bogris, D. Syvridis, S. Dasgupta, P. Petropoulos, and D. J. Richardson, "All-optical phase and amplitude regenerator for next-generation telecommunications systems," Nat. Photonics **4**, 690–695 (2010).
167. W. Li, M. Lu, A. Mecozzi, M. Vasilyev, S. Arafin, D. Dadic, L. A. Johansson, and L. A. Coldren, "First monolithically integrated dual-pumped phase-sensitive amplifier chip based on a saturated semiconductor optical amplifier," IEEE J. Quantum Electron. **52**, 1–12 (2016).
168. A. D. Ellis and S. Sygletos, "Phase sensitive signal processing using semiconductor optical amplifiers," in *Optical Fiber Commun. Conf.* (2013).
169. K. R. H. Bottrill, R. Kakarla, F. Parmigiani, D. Venkitesh, and P. Petropoulos, "Phase regeneration of QPSK signal in SOA using single-stage, wavelength converting PSA," IEEE Photonics Technol. Lett. **28**, 205–208 (2016).

170. S. Sygletos, M. J. Power, F. C. Garcia Gunning, R. P. Webb, R. J. Manning, and A. D. Ellis, "Simultaneous dual channel phase regeneration in SOAs," in *European Conf. Optical Commun.* (2012), paper Tu.1.A.2.
171. S. Sygletos, P. Frascella, S. K. Ibrahim, L. G Nielsen, R. Phelan, J. O'Gorman, and A. D. Ellis, "A practical phase sensitive amplification scheme for two channel phase regeneration," Opt. Express **19**, B938–B945 (2011).
172. C. Lundström, B. Corcoran, M. Karlsson, and P. A. Andrekson, "Phase and amplitude characteristics of a phase-sensitive amplifier operating in gain saturation," Opt. Express **20**, 21400–21412 (2012).
173. Z. Tong, C. Lundström, M. Karlsson, M. Vasilyev, and P. A. Andrekson, "Noise performance of a frequency nondegenerate phase-sensitive amplifier with unequalized inputs," Opt. Lett. **36**, 722–724 (2011).
174. A. Sobhanan, A. Iyer, A. Anthur, G. P. Agrawal, L. P. Barry, and D. Venkitesh, "Power optimization for phase quantization with SOAs using the gain extinction ratio," Opt. Express **29**, 1545–1557 (2021).
175. A. Iyer, A. Sobhanan, and D. Venkitesh, "Optimization of four- wave mixing based multilevel phase quantization through gain extinction ratio," in *2017 IEEE Workshop on Recent Advances in Photonics* (2017).
176. J. Kakande, R. Slavík, F. Parmigiani, A. Bogris, D. Syvridis, L. Grüner-Nielsen, R. Phelan, P. Petropoulos, and D. J. Richardson, "Multilevel quantization of optical phase in a novel coherent parametric mixer architecture," Nat. Photonics **5**, 748–752 (2011).
177. K. Solis-Trapala, M. Pelusi, H. N. Tan, T. Inoue, and S. Namiki, "Optimized WDM transmission impairment mitigation by multiple phase conjugations," J. Lightwave Technol. **34**, 431–440 (2016).
178. M. F. C. Stephens, M. Tan, I. D. Phillips, S. Sygletos, P. Harper, and N. J. Doran, "1-THz-bandwidth polarization-diverse optical phase conjugation of 10×114Gb/s DP-QPSK WDM signals," in *Optical Fiber Commun. Conf.* (2014), paper W3F.6.
179. M. A. Z. Al-Khateeb, M. E. McCarthy, C. Sanchez, and A. D. Ellis, "Nonlinearity compensation using optical phase conjugation deployed in discretely amplified transmission systems," Opt. Express **26**, 23945–23959 (2018).
180. M. A. Z. Al-Khateeb, M. E. McCarthy, and A. D. Ellis, "Performance enhancement prediction for optical phase conjugation in systems with 100km amplifier spacing," in *European Conf. Optical Commun.* (2017).
181. I. Sackey, R. Elschner, C. Schmidt-Langhorst, T. Kato, T. Tanimura, S. Watanabe, T. Hoshida, and C. Schubert, "Novel wavelength-shift-free optical phase conjugator used for fiber nonlinearity mitigation in 200-Gb/s PDM-16QAM transmission," in *Optical Fiber Commun. Conf.* (2017), paper Th3J.1.
182. S.L. Jansen, D. van den Borne, C. Climent, M. Serbay, C.-J. Weiske, H. Suche, P.M. Krummrich, S. Spalter, S. Calabro, N. Hecker-Denschlag, P. Leisching, W. Rosenkranz, W. Sohler, G.D. Khoe, T. Koonen, and H. de Waardt, "10,200 km 22×2×10 Gbit/s RZ-DQPSK dense WDM transmission without inline dispersion compensation through optical phase conjugation," in *Optical Fiber Commun. Conf.* (2005), paper.PDP28.
183. S. L. Jansen, D. van den Borne, P. M. Krummrich, S. Spalter, G.-. Khoe, and H. de Waardt, "Long-haul DWDM transmission systems employing optical phase conjugation," IEEE J. Sel. Top. Quantum Electron. **12**, 505–520 (2006).
184. H. Hu, R. Nouroozi, R. Ludwig, C. Schmidt-Langhorst, H. Suche, W. Sohler, and C. Schubert, "110 km transmission of 160 Gbit/s RZ-DQPSK signals by midspan polarization-insensitive optical phase conjugation in a Ti:PPLN waveguide," Opt. Lett. **35**, 2867–2869 (2010).

185. F. Da Ros, A. Gajda, E. P. da Silva, A. Peczek, A. Mai, K. Petermann, L. Zimmermann, L. K. Oxenløwe, and M. Galili, "Optical phase conjugation in a silicon waveguide with lateral p-i-n diode for nonlinearity compensation," J. Lightwave Technol. **37**, 323–329 (2019).
186. D. Vukovic, J. Schröder, F. Da Ros, L. B. Du, C. J. Chae, D.-Y. Choi, M. D. Pelusi, and C. Peucheret, "Multichannel nonlinear distortion compensation using optical phase conjugation in a silicon nanowire," Opt. Express **23**, 3640–3646 (2015).
187. F. Parmigiani, G. D. Hesketh, R. Slavík, P. Horak, P. Petropoulos, and D. J. Richardson, "Optical phase quantizer based on phase sensitive four wave mixing at low nonlinear phase shifts," IEEE Photonics Technol. Lett. **26**, 2146–2149 (2014).
188. A. Almaiman, Y. Cao, A. Mohajerin-Ariaei, M. Ziyadi, P. Liao, C. Bao, F. Alishahi, A. Fallahpour, B. Shamee, Y. Akasaka, T. Ikeuchi, S. Wilkinson, J. D. Touch, M. Tur, and A. E. Willner, "Phase-sensitive QPSK channel phase quantization by amplifying the fourth-harmonic idler using counter-propagating Brillouin amplification," Opt. Commun. **423**, 48–52 (2018).
189. R. Slavík, A. Bogris, J. Kakande, F. Parmigiani, L. Grüner-Nielsen, R. Phelan, J. Vojtěch, P. Petropoulos, D. Syvridis, and D. J. Richardson, "Field-trial of an all-optical psk regenerator/multicaster in a 40 Gbit/s, 38 channel DWDM transmission experiment," J. Lightwave Technol. **30**, 512–520 (2012).
190. J.-Y. Yang, M. Ziyadi, Y. Akasaka, S. Khaleghi, M. R. Chitgarha, J. Touch, and M. Sekiya, "Investigation of polarization-insensitive phase regeneration using polarization-diversity phase-sensitive amplifier," in *European Conf. Optical Commun.* (2013).
191. S. Liu, K. J. Lee, F. Parmigiani, J. Kakande, K. Gallo, P. Petropoulos, and D. J. Richardson, "Phase-regenerative wavelength conversion in periodically poled lithium niobate waveguides," Opt. Express **19**, 11705–11715 (2011).
192. A. D. Ellis and S. Sygletos, "Phase sensitive signal processing using semiconductor optical amplifiers," in *Optical Fiber Commun. Conf.* (2013), paper OW4C.1.
193. S. Hongcheng, W. Ke-Yao, and C. Foster Amy, "Pump-degenerate phase-sensitive amplification in amorphous silicon waveguides," Opt. Lett. **42**, 3590–3593 (2017).
194. W. Yang, Y. Yu, M. Ye, G. Chen, C. Zhang, and X. Zhang, "Phase regeneration for polarization-division multiplexed signals based on vector dual-pump nondegenerate phase sensitive amplification," Opt. Express **23**, 2010–2020 (2015).
195. F. Da Ros, M. Pu, L. Ottaviano, H. Hu, E. Semenova, M. Galili, K. Yvind, and L.K. Oxenlowe, "Phase-sensitive four-wave mixing in AlGaAs-on-insulator nano-waveguides," in *IEEE IPC* (2016), pp. 505–506.
196. https://rpmclasers.com/wp-content/uploads/products/DX1_Manual.pdf. Accessed May 2022.
197. https://www.inphenix.com/en/semiconductor-optical-amplifiers/. Accessed May 2022.
198. https://www.pritel.com/high_power_fa.html Accessed May 2022.
199. N. Dupius, "CMOS photonic nanosecond-scale switch fabrics," in *Optical Fiber Commun. Conf.* (2016), paper M3I.1.
200. K. Suzuki, R. Konoike, J. Hasegawa, S. Suda, H. Matsuura, K. Ikeda, S. Namiki, and H. Kawashima, "Low-insertion-loss and power-efficient 32 × 32 silicon photonics switch with extremely high-Δ silica PLC connector," J. Lightwave Technol. **37**, Th4B.5 (2019).

201. A. Wonfor, H. Wang, R. V. Penty, and I. H. White, "Large port count high-speed optical switch fabric for use within datacenters [invited]," J. Opt. Commun. Netw. **3**, A32 (2011).
202. M. Ding, A. Wonfor, Q. Cheng, R. V. Penty, and I. H. White, "Emulation of a 16×16 optical switch using cascaded 4×4 dilated hybrid MZI-SOA optical switches," in *Optical Fiber Commun. Conf.* (2017).
203. R. Stabile, A. Albores-Mejia, and K. A. Williams, "Monolithic active-passive 16×16 optoelectronic switch," Opt. Lett. **37**, 4666–4668 (2012).
204. R. Konoike, K. Suzuki, T. Inoue, T. Matsumoto, T. Kurahashi, A. Uetake, K. Takabayashi, S. Akiyama, S. Sekiguchi, S. Namiki, H. Kawashima, and K. Ikeda, "SOA-integrated silicon photonics switch and its lossless multistage transmission of high-capacity WDM signals," J. Lightwave Technol. **37**, 123–130 (2019).
205. J. Kurumida and S. J. Ben Yoo, "Nonlinear optical signal processing in optical packet switching systems," IEEE J. Sel. Top. Quantum Electron. **18**, 978–987 (2012).
206. H. Le-Minh, Z. Ghassemlooy, W. P. Ng, and M. F. Chiang, "All-optical router with pulse-position modulation header processing in high-speed photonic packet switching networks," IET. Commun. **3**, 465–476 (2009).
207. N. Calabretta, Y. Liu, H. de Waardt, M. T. Hill, G. D. Khoe, and H. J. S. Dorren, "Multiple-output all-optical header processing technique based on two-pulse correlation principle," Electron. Lett. **37**, 1238–1240 (2001).
208. H. J. S. Dorren, M. T. Hill, Y. Liu, N. Calabretta, A. Srivatsa, F. M. Huijskens, H. de Waardt, and G. D. Khoe, "Optical packet switching and buffering by using all-optical signal processing methods," J. Lightwave Technol. **21**, 2–12 (2003).
209. A. Martinez, F. Ramos, J. Marti, J. Herrera, and R. Llorente, "All optical N-bit XOR gate with feedback for optical packet header processing," in *European Conf. Opt. Commun.* (2002).
210. J. M. Martinez, F. Ramos, and J. Marti, "All-optical packet header processor based on cascaded SOA-MZIs," Electron. Lett. **40**, 894–895 (2004).
211. R. P. Webb, J. M. Dailey, R. J. Manning, G. D. Maxwell, A. J. Poustie, S. Lardenois, R. Harmon, J. Harrison, G. Kopidakis, E. Athanasopoulos, A. Krithinakis, F. Doukhan, M. Omar, D. Vaillant, F. Di Nallo, M. Koyabe, and C. D. C.-Gilfedder, "All-optical header processing in a 42.6 Gb/s optoelectronic firewall," IEEE J. Sel. Top. Quantum Electron. **18**, 757–764 (2012).
212. R. Kakarla and D. Venkitesh, "Demonstration of optical header recognition for BPSK data using novel design of logic gates," Opt. Commun. **363**, 117–122 (2016).
213. W. Shieh, E. Park, and A. E. Wilner, "All-optical wavelength shifting of microwave subcarriers by using four-wave mixing in a semiconductor optical amplifier," IEEE Photonics Technol. Lett. **8**, 524–526 (1996).
214. J. Capmany, S. Sales, D. Pastor, A. Martinez, and B. Ortega, "Wavelength conversion of SCM signals using semiconductor optical amplifiers: theory, experiments, and applications," J. Lightwave Technol. **21**, 961–972 (2003).
215. B. Pesala, Z. Chen, A. V. Uskov, and C. Chang-Hasnain, "Experimental demonstration of slow and superluminal light in semiconductor optical amplifiers," Opt. Express **14**, 12968–12975 (2006).
216. H. Su, P. Kondratko, and S. Lien Chuang, "Variable optical delay using population oscillation and four-wave-mixing in semiconductor optical amplifiers," Opt. Express **14**, 4800–4807 (2006).
217. W. Xue, Y. Chen, F. Öhman, S. Sales, and J. Mørk, "Enhancing light slow-down in semiconductor optical amplifiers by optical filtering," Opt. Lett. **33**, 1084–1086 (2008).

218. P. Berger, J. Bourderionnet, M. Alouini, F. Bretenaker, and D. Dolfi, "Theoretical study of the spurious-free dynamic range of a tunable delay line based on slow light in SOA," Opt. Express **17**, 20584–20597 (2009).
219. S. Ó Dúill, E. Shumakher, and G. Eisenstein, "Noise properties of microwave phase shifters based on semiconductor optical amplifiers," J. Lightwave Technol. **28**, 791–797 (2010).
220. J. Lloret, F. Ramos, W. Xue, J. Sancho, I. Gasulla, S. Sales, J. Mork, and J. Capmany, "The influence of optical filtering on the noise performance of microwave photonic phase shifters based on SOAs," J. Lightwave Technol. **29**, 1746–1752 (2011).
221. E. Shumakher, S. O Duill, and G. Eisenstein, "Optoelectronic oscillator tunable by an SOA based slow light element," J. Lightwave Technol. **27**, 4063–4068 (2009).
222. J. Capmany, J. Mora, I. Gasulla, J. Sancho, J. Lloret, and S. Sales, "Microwave photonic signal processing," J. Lightwave Technol. **31**, 571–586 (2013).
223. W. Xue, S. Sales, J. Capmany, and J. Mørk, "Wideband 360° microwave photonic phase shifter based on slow light in semiconductor optical amplifiers," Opt. Express **18**, 6156–6163 (2010).
224. A. P. Anthur, R. T. Watts, T. N. Huynh, D. Venkitesh, and L. P. Barry, "Measuring the correlation of two optical frequencies using four-wave mixing," Appl. Opt. **53**, 7704–7708 (2014).
225. A. P. Anthur, V. Panapakkam, V. Vujicic, K. Merghem, F. Lelarge, A. Ramdane, and L. P. Barry, "Correlation coefficient measurement of the mode-locked laser tones using four-wave mixing," Appl. Opt. **55**, 4441–4445 (2016).
226. A. Reale, P. Lugli, and S. Betti, "Format conversion of optical data using four-wave mixing in semiconductor optical amplifiers," IEEE J. Sel. Top. Quantum Electron. **7**, 703–709 (2001).
227. C. H. Kwok and C. Lin, "Polarization-insensitive all-optical NRZ-to-RZ format conversion by spectral filtering of a cross phase modulation broadened signal spectrum," IEEE J. Sel. Top. Quantum Electron. **12**, 451–458 (2006).
228. G. Lin, K. Yu, and M. Lo, "All-Optical RZ data conversion with temporally and spectrally gain-sliced semiconductor optical amplifier via broadband optical injection," IEEE J. Sel. Top. Quantum Electron. **14**, 789–800 (2008).
229. T. G. Silveira, A. Teixeira, G. T. Beleffi, D. Forin, P. Monteiro, H. Furukawa, and N. Wada, "All-Optical conversion from RZ to NRZ using gain-clamped SOA," IEEE Photonics Technol. Lett. **19**, 357–359 (2007).
230. H. Hoshino, T. Okada, and M. Matsuura, "Photonic analog-to-digital conversion using a red frequency chirp in a semiconductor optical amplifier," Opt. Lett. **43**, 2272–2275 (2018).
231. T. Okada, R. Kobayashi, W. Rui, M. Sagara, and M. Matsuura, "Photonic digital-to-analog conversion using a blue frequency chirp in a semiconductor optical amplifier," Opt. Lett. **45**, 1483–1486 (2020).
232. H. Wen, Y. Alahmadi, P.k LiKamWa, C. Xia, C. Carboni, and G. Li, "Invited article: four-mode semiconductor optical amplifier," APL Photonics **1**, 070801 (2016).
233. Y. Alahmadi, H. Wen, P. LiKamWa, and G. Li, "Few-mode degenerate four-wave mixing in a few-mode semiconductor optical amplifier," in *Optical Fiber Commun. Conf.* (2019), paper W1C.6.
234. H. Wen, Y. Alahmadi, P. LiKamWa, and G. Li, "Modeling parametric processes in few-mode semiconductor optical amplifiers," IEEE J. Sel. Top. Quantum Electron. **24**, 1–17 (2018).

Aneesh Sobhanan received a B.Tech. in Electronics and Communication Engineering from CUSAT, Kerala in 2009. He received M.Tech. and Ph.D. degrees in Electrical Engineering from Indian Institute of Technology Madras, India, in 2014 and 2021, respectively. He is currently a Postdoctoral Research Associate at Aston Institute of Photonic Technologies, Aston University, Birmingham, UK. His research interests focus on nonlinear optics and semiconductor optical amplifiers and its applications in optical communication.

Aravind Padath Anthur, Ph.D., is currently working as a scientist in the QTE department of the IMRE, A*STAR, Singapore. He obtained his Ph.D. from IIT Madras, India on the topic of nonlinear optics for telecom applications. He worked as senior engineer in R&D at Tejas Networks Bangalore after his Ph.D. He was a postdoctoral fellow at the RINCE Institute of Dublin City University, Ireland. He has more than 10 years of research experience, having published more than 50 papers in international peer-reviewed journals and conferences.

Sean O'Duill received B.E. and Ph.D. degrees from University College Dublin in 1999 and 2008 respectively. The work of the Ph.D. thesis concerned tunable laser characterization for dual-format signalling and for the effect of optical fiber nonlinearities on dual-format signals. From May 2008 until September 2011, he was a postdoctoral fellow at the Technion working on "slow light" techniques for microwave signal processing and also for optical frequency comb generation. From October 2011 until October 2012, he was with the Karlsruhe Institute of Technology, developing theory and numerical simulation platforms of semiconductor optical amplifiers for use in PONs and for all-optical signal processing. Since November 2012 he has been with the Radio and Optics Communications Laboratory at DCU, simulating performance capabilities of optical signal processing subsystems for use in future networks and from August 2015 until December 2019 received an SFI Industrial Fellowship to work part time designing lasers within a DCU spin-off company, Pilot Photonics Ltd.

Mark Pelusi graduated with a Ph.D. in Electrical Engineering from the University of Melbourne in Australia and has held various research positions in both academia and industry in the field of high-bit-rate optical fiber communications and nonlinear signal processing. He was a Research Fellow at the Femtosecond Technology Research Association in Japan, Senior Hardware Engineer at Corvis Corporation in the USA, and Senior Research Fellow at the University of Sydney, Australia, where he was also leader of the flagship project in the ARC Centre for Ultrahigh bandwidth Devices and Optical Systems (CUDOS) on Nonlinear Signal Processing and Terabit per Second Communications. He is currently a Senior Researcher at the National Institute of Advanced Industrial Science and Technology (AIST).

Shu Namiki received M.S. and Dr.Sci. degrees in applied physics from Waseda University, Tokyo, Japan, in 1988 and 1998, respectively. From 1988 to 2005, he was working for Furukawa Electric Co., Ltd., where he developed award-winning high-power pump lasers, and patented multi-wavelength-pumped fiber Raman amplifiers. From 1994 to 1997, he was a Visiting Scientist at the Massachusetts Institute of Technology, Cambridge, where he studied mode-locked fiber lasers and ultra-short pulses in optical fiber. In 2005, he moved to the National Institute of Advanced Industrial Science and Technology (AIST), Tsukuba, Japan, where he has served as Executive Committee Chair of a 10-year national project called "Vertically Integrated Center for Technologies of Optical Routing toward Ideal Energy Savings (VICTORIES)" in collaboration with ten telecom-related companies, and he is currently Research Director of Platform Photonics Research Center in AIST. He has authored or coauthored more than 500 conference presentations, papers, book chapters, articles, and patents. His current research interests include software defined dynamic optical path networking and their enabling devices such as nonlinear fiber-optics and silicon photonics. He was an Associate Editor and Advisory Editor of *Optics Express* and the Co-Editor-in-Chief of the *IEICE Transactions on Communications*. He has been on the technical committee for OFC, ECOC, CLEO, OECC, OAA, etc., and served as Program Co-Chair of OFC 2015 and General Co-Chair of OFC 2017. Dr. Namiki is a Fellow of Optica and IEEE and a member of IEICE and JSAP.

Liam Barry received his B.E. degree in electronic engineering and M.Eng.Sc. degree in optical communications from University College Dublin in 1991 and 1993 respectively. From 1993 to 1996 he was employed as a Research Engineer in the Optical Systems Department of France Telecom's Research Laboratories (now known as Orange Labs) in Lannion, France, and as a result of his work on high-capacity optical networks he obtained his Ph.D. degree from the University of Rennes. In February 1996 he joined the Applied Optics Centre in Auckland University, New Zealand as a Research Fellow and in 1998 he took up a lecturing position in Dublin City University and established the Radio and Optical Communications Laboratory. He is currently Professor in the School of Electronic Engineering, Member of the Royal Irish Academy (MRIA), Member of the Irish Research Council (IRC), Principal Investigator for Science Foundation Ireland, and Director of the Radio and Optical Communications Laboratory. His main research interests are: all-optical signal processing, hybrid radio/fiber communication systems, and wavelength tunable lasers and optical frequency combs for flexible high-capacity networks. He has published over 500 articles in international peer-reviewed journals conferences and holds 10 patents in the area of optoelectronics. He has been a regular TPC member for the European Conference on Optical Communications (ECOC) since 2004 and served as ECOC Co-Chair for ECOC2019 in Dublin. He has also been a TPC member for the Optical Fibre Communication Conference (OFC) from 2007 to 2010, serving as Chair of the Optoelectronic Devices sub-committee for OFC 2010.

Deepa Venkitesh obtained her master's degree in physics from the University of Kerala and PhD from IIT Bombay. She is currently a Professor in the Department of Electrical Engineering, IIT Madras. Her areas of research interest include coherent optical communication, photonic signal processing, and fiber lasers. She has published more than 50 articles in international peer-reviewed journals and many more in conferences. She was bestowed with the Young Faculty Recognition Award of IIT Madras in 2012 and the Abdul Kalam Technology Innovation Fellowship of INAE in 2021. She is Senior Member of OSA and is currently the Associate Editor of the Optica journal *Advances in Optics and Photonics*. She is also currently the Associate Vice President of "Women in Photonics" of the IEEE Photonics Society.

Govind P. Agrawal received a B.S. degree from the University of Lucknow in 1969 and M.S. and Ph.D. degrees from the Indian Institute of Technology, New Delhi in 1971 and 1974, respectively. After holding positions at the Ecole Polytechnique, France, the City University of New York, and Bell Laboratories, Murray Hill, NJ in 1989 he joined the faculty of the Institute of Optics at the University of Rochester, where he is the James C. Wyant Professor of Optics. His research interests focus on optical communications, nonlinear optics, and silicon photonics. He is an author or coauthor of 8 books and more than 450 research publications. His books on *Nonlinear Fiber Optics* (Academic Press, 6th ed., 2019) and *Fiber-Optic Communication Systems* (Wiley, 5th ed., 2021) are used worldwide for research and teaching. He is involved with both IEEE and Optica and has served on the Optica Board of Directors. He was the Editor-in-Chief of *Advances in Optics and Photonics* during 2014–2019. He was the recipient of IEEE Quantum Electronics Award in 2012, the Esther Hoffman Beller Medal in 2015, the OSA Max Born Award in 2019, and the EPS Quantum Electronics and Optics Medal in 2019. He is a Fellow of OSA and a Life Fellow of IEEE. He is also a Distinguished Fellow of the Optical Society of India.